MACHINE LEARNING ASSISTED STRATEGIC SYNTHESIS OF TISSUE MIMETIC ELASTOMERS

Yidan Cong

A dissertation submitted to the faculty at the University of North Carolina at Chapel Hill in partial fulfillment of the requirements for the degree of Doctor of Philosophy in the Department of Chemistry.

Chapel Hill
2021

Approved by:

Wei You

Sergei S. Sheiko

Frank A. Leibfarth

Richard Superfine

Stephen L. Craig

ABSTRACT

Yidan Cong: Machine Learning Assisted Strategic Synthesis of Tissue Mimetic Elastomers
(Under the direction of Sergei Sheiko)

Over the course of evolution, biological creatures in nature have developed various elegant mechanisms to defend themselves. Particularly, soft biological tissues not only serve as cushions but at the same time, also prevent tearing. Meanwhile, some tissues, such as the skin of chameleons, can also display adaptive coloration which protects them from predators and helps them attract spouses. Inspired by the multifunctionality of biological tissues, this study focused on developing materials that possess a combination of these unique properties. To characterize the nonlinear elasticity of tissues and synthetic materials that mimic this property, we used firmness β and Young's modulus E_0. To unravel the origin of mechanical properties of tissues, we studied the stress-strain curves of previously measured tissues from literatures. We demonstrated that the mechanical properties of tissues were tied to their functions and structural organization of collagens. To target the nonlinear elasticity synthetically, we used linear-bottlebrush-linear (LBL) triblock copolymers that micro-phase separate into physical networks, which we named plastomers. The triblock was produced by a two-step atomic transfer radical polymerization (ATRP) synthesis: the bottlebrush macroinitiator was synthesized by grafting-through polymerization followed by linear chain extension from both ends of the macroinitiator. The synthetic challenges and synthetic outcomes on the effect of mechanical properties of plastomers were investigated. Rigorous

kinetic studies were performed to optimize the synthetic conditions for producing bottlebrush macroinitiator with high chain end fidelity. Next, we investigated in the control of mechanical properties by varying architectural parameters as well as mixing experiments. We showed that there is still a gap between synthetic plastomers and biological tissues. In particular, we lacked synthetic materials that possessed high firmness ($\beta > 0.8$) and high modulus ($E_0 > 10^5$ Pa). To bridge this gap, we needed to target plastomers with specific firmness and modulus. Therefore, we developed statistical and machine learning models that predicted the mechanical properties of triblocks based on chemical and architectural parameters. Finally, we investigated in incorporating structural coloration into plastomers. We studied factors, such as architectural parameters of the plastomers and swelling that controlled the reflected color of the plastomers. Specifically, we utilized ultraviolet-visible (UV-VS) spectroscopy and small angle X-ray scattering (SAXS) to demonstrate the effect of these factors on reflected wavelength and periodicity of the plastomers.

TABLE OF CONTENTS

LIST OF TABLES

LIST OF FIGURES

LIST OF ABBREVIATIONS AND SYMBOLS

2f-BiB	Difunctional ethylene bis(2-bromoisobutyrate) initiator
AFM	Atomic force microscopy
ATRP	Atom transfer radical polymerization
BB	Bottlebrush
BBCP	Bottlebrush copolymer
BzMA	Benzyl methacrylate
$CDCl_3$	Deuterated chloroform
C_s	Chain transfer coefficient
Đ	Dispersity
DMA	Dynamic mechanical analysis
DP	Degree of polymerization
d_1	Inter-brush distance
d_2	Radius of linear domain
d_3	Distance between linear domains
E	Structural modulus
E_0	Young's modulus
^{1}H-NMR	Proton nuclear magnetic resonance
L_0	Length of material at releaxed state
LB	Linear-bottlebrush
LBL	Linear-bottlebrush-linear
MAE	Mean absolute error
Me_6TREN	*tris*[2-(dimethylamino) ethyl] amine

MMA	Methyl methacrylate
M_n	Number average molecular weight
M_w	Weight average molecular weight
n_{bb}	Degree polymerization of the bottlebrush backbone
n_i	Refractive index
n_g	Grafting density of the side chains
n_L	Degree polymerization of the linear block
n_{sc}	Degree polymerization of the side chain
PBzMA	Poly(benzyl methacrylate)
PDMSMA	Poly(dimethylsiloxane methacrylate) macromonomer
PEG	Poly(ethylene glycol)
PMMA	Poly(methyl methacrylate)
PnBMA	Poly(n-butyl methacrylate)
PNiPAM	Poly(*N*-isopropylacrylamide)
POEOMA	Poly(oligo ethylene oxide methacrylate)
Ref	Reference
$< R_{in}{}^2 >$	Mean squared end-to-end distance
R_{max}	Polymer chain contour length
SARA	Supplemental activating and reducing agent
SAXS	Small angle X-ray scattering
T_g	Glass transition temperature
THF	Tetrahydrofuran
V_b	Volume fraction of the bottlebrush block

V_L	Volume fraction of the linear block
β	Firmness parameter
δ	Solubility parameter
θ	Reflection angle
λ	Elongation ratio
λ_{fit}	Elongation ratio fitting
λ_{max}	Maximum elongation ratio
σ_{eng}	Engineering stress
σ_{true}	True stress
ϕ_L	Volume fraction of linear block
χ	Flory-Huggins interaction parameter
$\partial\sigma_{true}/\partial\lambda$	Differential modulus

CHAPTER 1

Inspiration from Nature

1.1 Introduction

Many of the greatest human inventions have been inspired by nature[1-3]. For instance, the shape of birds' wings inspired the invention of airplanes. The tactile sensing of fingers motivated engineers in building robots with the same ability. Sonar was invented based on echolocation and sonar system of bats and dolphins[4] (**Figure 1.1**). These abilities of animals have evolved over the course of revolution to increase their chances of survival. Among these fascinating abilities, we are particularly interested in the defensive mechanisms of biological tissues: softness, firmness, and structural coloration as they are crucial in the application of wearable electronics, biomedical devices and soft robotics[5-7]. Many types of biological tissues are soft in order to cushion the intricate biological systems within the body. Meanwhile, tissues are firm as stretching is limited once the strain of tissues exceeds a certain threshold. This restriction prevents tissue from being overly stretched. In addition to softness and firmness, some animal skins are colorful, such as chameleons. They display vivid color, which can also change when exposed to external stimuli. This coloration allows animals to hide from or warn predators and attract spouses.

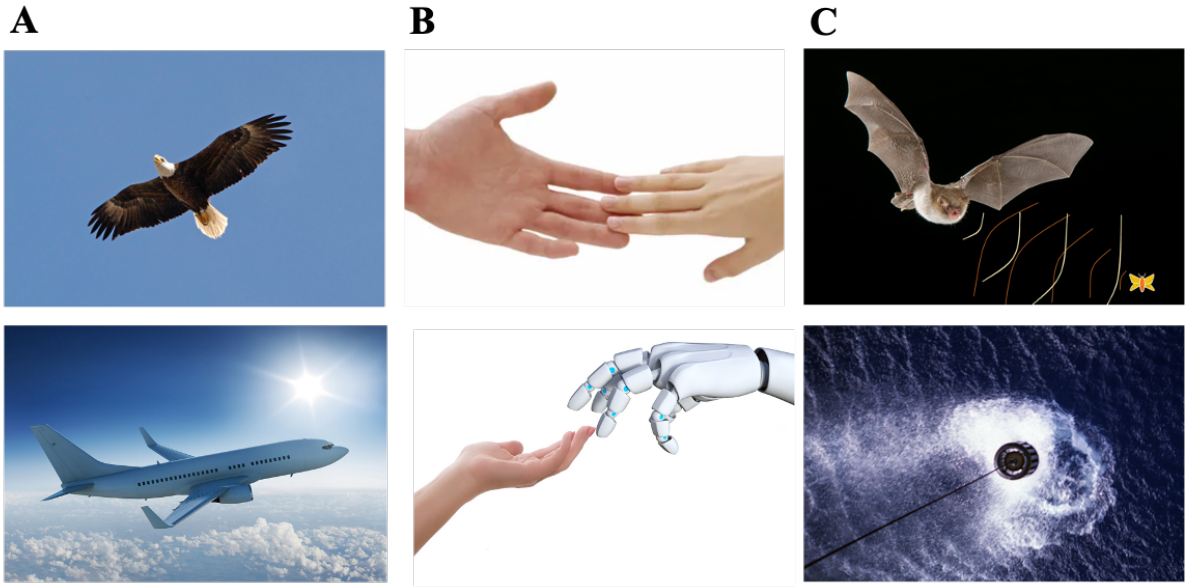

Figure 1.1: Examples of inventions inspired by nature. (A) Airplane inspired by bird wings. **(B)** Tactile sensing of robotics inspired by human hands. **(C)** Sonar system inspired by echolocation of bats.

1.2 Mechanical properties of tissues

The seemingly contradictive mechanical properties of tissues, softness and firmness, are achieved by the two main protein components of tissues: collagen and elastin[8]. Collagen is a type of protein that occupies 30% of the protein mass in the human body[9]. Collagen fibers are formed by three protein chains that assemble into triple helices (**Figure 1.2)**. Each protein chain is composed of tri-amino acid Gly-X-Y repeats, where Gly stands for glycine and X and Y are usually proline and 4-hydroxy-proline, resepctively[10]. Each collagen fiber can then further assemble into different structural organizations such as forming bundles or networks. Meanwhile, elastin is a protein that forms branching networks, which control tissues' stretching and recoiling. Once stretched, the recoil of elastin is driven by two types of entropic forces: the hydrophobic effect which describes solvent entropy, and a high structural disorder of the polypeptide chain, which describes solute entropy[11]. High polypeptide chain

disorder opposes both stretching and tight packing, since both restrict the number of possible confirmations of the protein. While collagen provides tissues with high tensile strength, elastin allows tissues to be elastic and resilient. The combination of these two proteins allows tissues to resist tearing. Even when a small strain is applied, the stress of tissues increases exponentially. Hence, biological tissues are known to have non-linear elasticity mechanical properties[12-14].

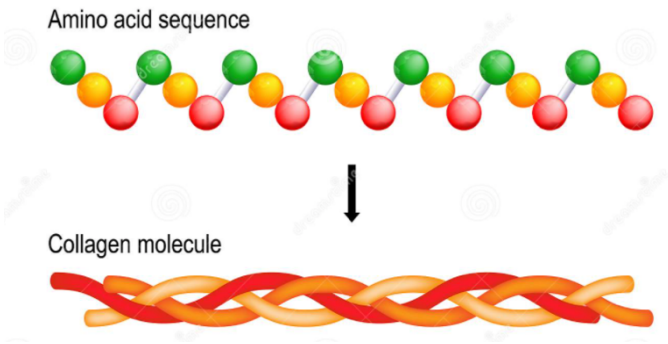

Figure 1.2: Triple helix structure of collagen molecule. Gly-X-Y amino acid sequence repeats assemble into triple helices.

1.3 Coloration in Nature

A rich variety of animals display color, either to attract spouses, scare away predators, or camouflage[7]. There are two types of biological color: pigmentation and structural coloration[5,6] (**Figure 1.3**). In the case of pigmentation, animals such as cephalopods contain cells that are rich in chemicals capable of absorbing wavelengths in the visible range, giving them vibrant colors. On the contrary, components in tissues that have structural coloration are colorless. Rather, nanostructures form periodic morphologies that reflect light with wavelengths in the visible range by constructive interference.

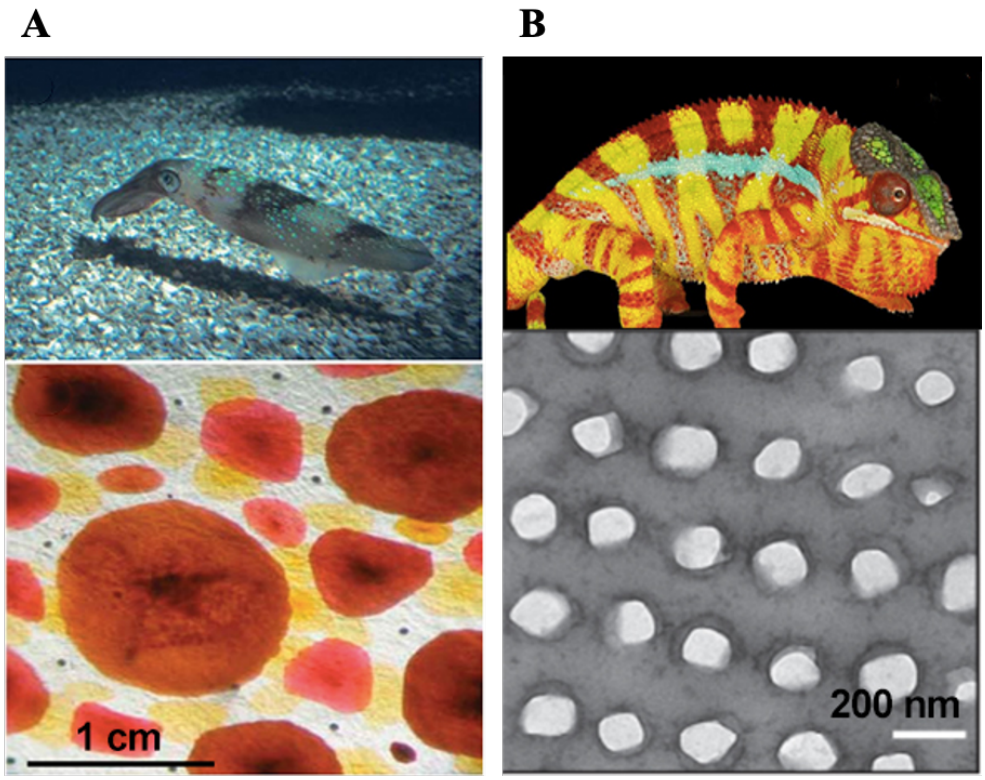

Figure 1.3: Two types of coloration in nature. (A) Pigmentation in cephalopods[5]. **(B)** Structural coloration in chameleons[6].

A representative example of structural coloration in animals is chameleons, which have nanocrystals periodically distributed in the cytoplasm, and in turn, display various colors. Furthermore, chameleons can vary the periodicity to change the color they display. Periodicity can occur in one direction, as in the case of butterflies, two directions, as in the case of peacocks, and three directions, as in the case of chameleons[6, 15, 16] (**Figure 1.4**).

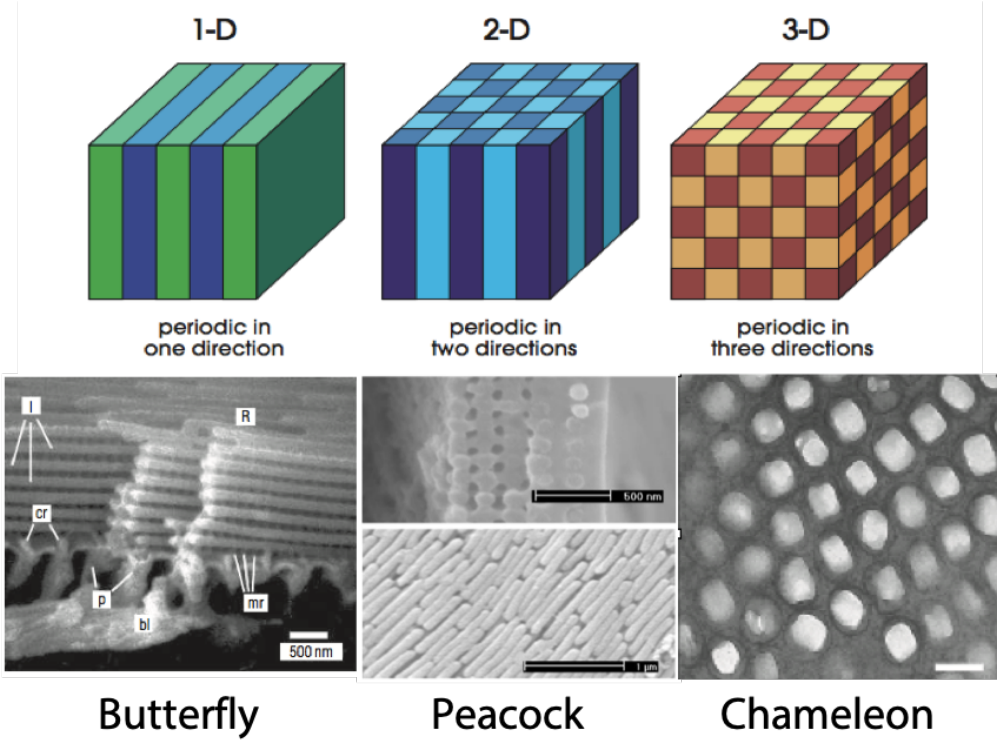

Figure 1.4: Examples of structural coloration in nature.

1.4 Summary and Outline

Being able to incorporate the softness, firmness, and structural coloration into synthetic materials is crucial in the applications of biomedical devices, soft robotics and wearable electronics. Multiple factors need to be considered when selecting a synthetic candidate for these applications, including but not limited to cost, toxicity, and reproducibility. This study aimed to design a material that possesses both mechanical and optical properties of tissues while being cost efficient to produce in bulk, has no leakage, and stable under ambient conditions. **Chapter 2** introduced the unique non-linear elasticity of tissues and the physical model used to characterize this adaptive mechanics for both tissues and synthetic materials throughout this study. **Chapter 3** discussed the origin of the variety

in mechanical properties of biological tissues. It included a thorough study of comparing tissues' mechanical properties according to categories, functions, and structural organization of collagens. **Chapter 4** addressed the current limitations of synthetic materials in mimicking multifunctionalities of biological tissues and strategies to overcome these challenges. **Chapter 5** discussed methods to optimize the synthetic conditions to ensure consistent and robust outcomes. **Chapter 6** discussed controlling the mechanical properties by varying the chemical and architectural parameters of synthetic polymers as well as by mixing different polymers. **Chapter 7** introduced statistical and machine learning models used to predict mechanical properties of synthetic materials. **Chapter 8** discussed the physical origin of structural coloration. **Chapter 9** addressed the control of coloration. Finally, **Chapter 10** discussed future works on this subject.

CHAPTER 2

Mechanical Properties of Tissues

2.1 Unique non-linear elasticity of tissues

Compared to common synthetic materials, biological tissues possess unique mechanical properties[12,17-20]. **Figure 2.1** shows the stress-strain curves of common synthetic materials and tissues, where stress is represented by σ and strain is represented by $\lambda = L/L_0$, which is the ratio between elongated length (L) and initial length of the material (L_0). The deformation of tissues has two phases: low modulus elastic deformation at smaller strains followed by rapid stiffening and yielding at larger deformations[12-14,21,22]. This two-step deformation process is not observed in synthetic materials as shown in **Figure 2.1**. While thermoplastic was stiff, it had a much higher modulus than tissue. Rubber and gel possessed low modulus but was incapable of rapid stiffening. Therefore, common commercial materials can either reproduce tissues' softness or stiffness but not both[18,23-25].

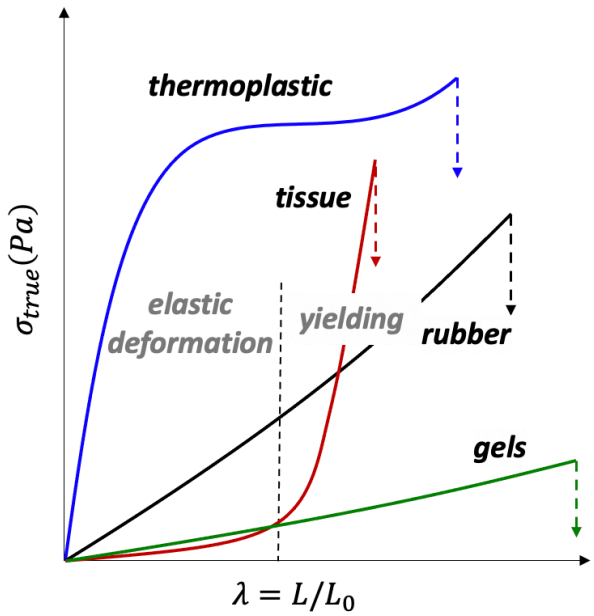

Figure 2.1: Comparison of stress elongation response between tissues and commercial materials. λ: elongation, which is the ratio between elongated length (L) and initial length (L_0). σ_{true}: true stress. $\sigma_{true} = \sigma_{eng}\lambda$, where σ_{eng} is the engineering stress.

The distinction between tissues and synthetic materials can also be observed in the derivative plot in **Figure 2.2**. The partial derivative of with respect to strain (elongation) of tissues displayed a distinguished sigmoid shape, demonstrating the rapid increase in stress upon transitioning into the second deformation step. Meanwhile, the derivatives of synthetic materials did not exhibit such drastic increase. Rather, the derivatives either plateaued or increased slowly, showing linear increase in stress with applied strain.

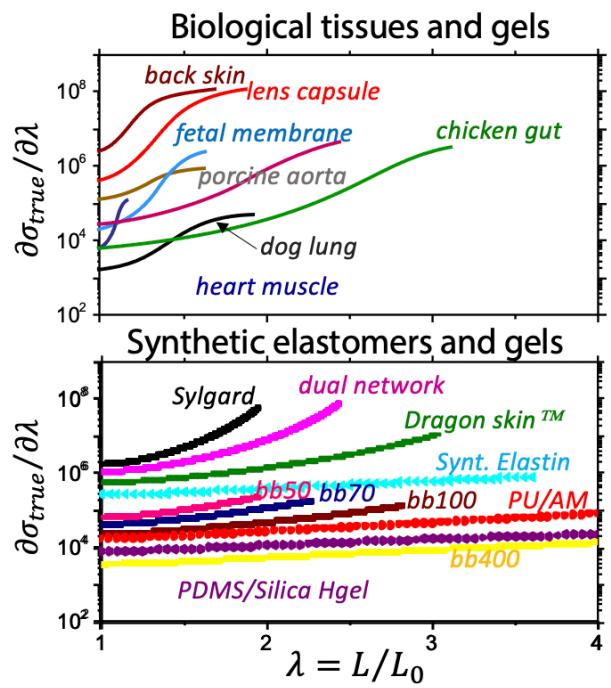

Figure 2.2: Comparison of differential stress between biological tissues and synthetic materials. λ: elongation, which is the ratio between elongated length (L) and initial length (L_0). σ_{true}: true stress. $\sigma_{true} = \sigma_{eng}\lambda$, where σ_{eng} is the engineering stress. $\partial\sigma_{true}/\lambda$: differential true stress with respect to elongation. Synt. Elastin: synthetic elastin. bb50, bb70, bb100, 400: bottlebrush elastomers with degree of polymerization (DP) of backbone = 50, 70, 100, 400. PU/AM: poly(urethane)/acrylamide hydrogel. PDMS: poly(dimethylsiloxane).

2.2 Physical model for characterization of tissues' mechanics

To characterize the mechanical properties of tissues and tissue-like materials, we used an equation of state[26], which describes the relation between the true stress σ_{true} and elongation $\lambda = L/L_0$.

$$\sigma_{true}/(\lambda^2 - \lambda^{-1}) = \frac{E}{3}\left(1 + 2\left(1 - \frac{\beta\left(\lambda^2 + \frac{2}{\lambda}\right)}{3}\right)^{-2}\right) \quad (1)$$

E is the structural modulus and β is the firmness parameter ($\beta = \langle R_{in}^2\rangle/R_{max}^2$), where $\langle R_{in}^2\rangle$is the mean square end-to-end distance between neighboring L-domains and R_{max} is the

contour length of the bottlebrush backbone. Hence, the value of β is always between 0 and 1. Typically, β of linear polymer is lower than 0.1 while that of bottlebrush is higher than 0.8. The higher the β, the less extendable the material, or in other words, the firmer the material. By substituting λ = 1 into the right-hand side of eq 1, we obtain the Young's modulus E_0:

$$E_0 = E(1 + 2(1 - \beta)^{-2})/3. \quad (2)$$

Figure 2.3 demonstrated the effect of firmness on the stress strain curves of materials. Each curve was constructed using the theoretical equation (1). While the structural modulus is constant, the higher the firmness, the more rapidly stiffening the material.

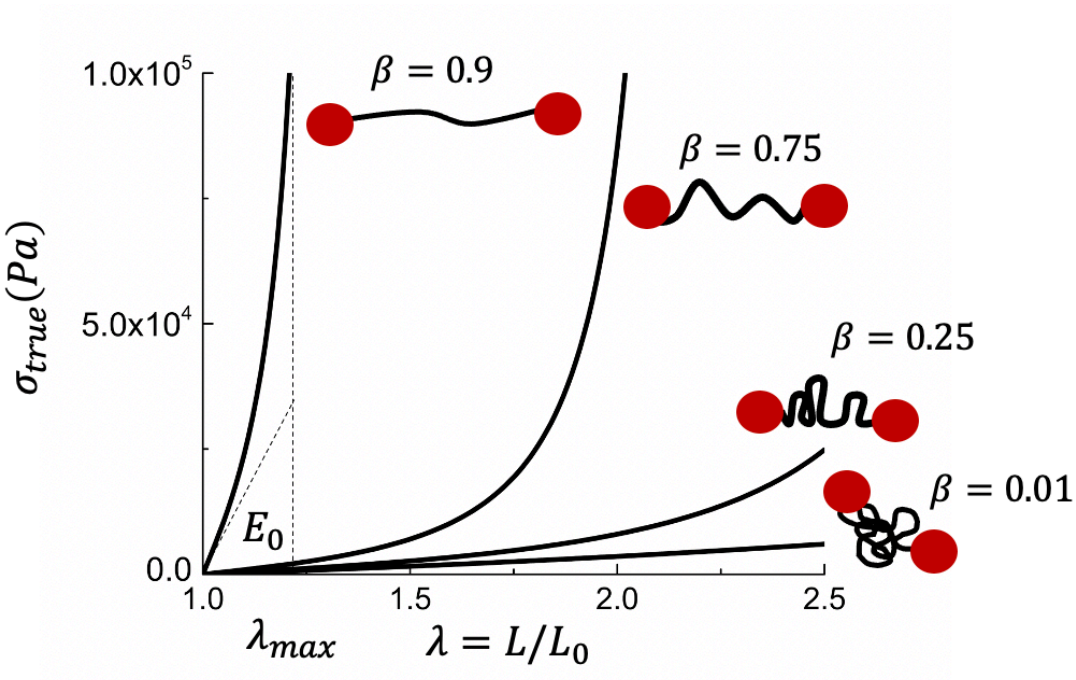

Figure 2.3: Effect of firmness (β) on the shape of the stress-strain curves. λ_{max}: Elongation at which the material breaks. The curves were plotted by substituting E = 3000 Pa into equation (1) while varying the values of β.

In an experimental setting, the stress-strain curves are obtained by tensile stress measurements on a dynamic mechanical analysis (DMA) instrument. The experimental data

are then fitted using equation (1) to obtain structural modulus E and firmness β. **Figure 2.4** showed a few examples of experimental stress-curves of tissues, all of which exhibited similar J shapes to the theoretical curves illustrated in **Figure 2.3**. **Table 2.1** summarized the firmness β and moduli values of the tissues in **Figure 2.4**. The firmness of tissues fell in the range of (0.2, 1), while the order of magnitude of Young's modulus E_0 was in the range of $10^3 - 10^5$ Pa. Hence, the mechanical properties of tissues could be described as soft but firm.

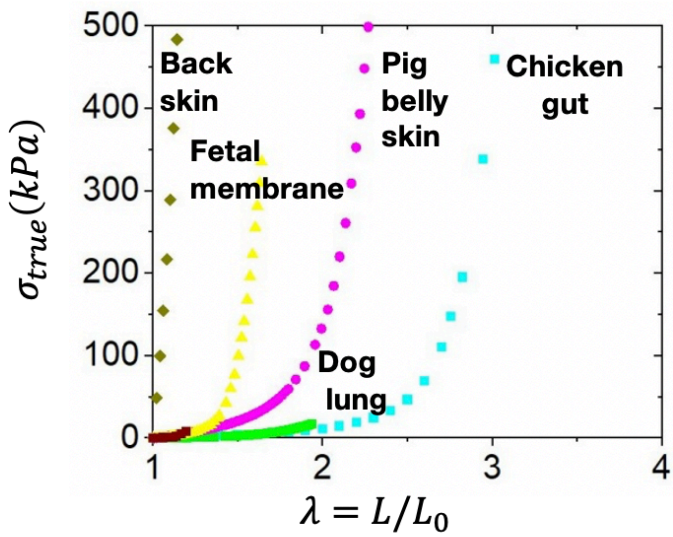

Figure 2.4: Examples of experimental tissues' stress-elongation curves.

Table 2.1: Firmness and modulus of example biological tissues.

Tissue Type	β	E (kPa)	E_0 (kPa)
Back skin	0.90	36.1	2417
Fetal membrane	0.79	1.28	19.8
Dog lung	0.69	0.25	1.8
Pig belly skin	0.45	11.2	28.5
Chicken gut	0.29	3.41	5.6

CHAPTER 3

Variety of Tissues' Mechanical Properties

3.1 Tissue types

Over the course of evolution, human and other invertebrates have developed sophisticated functional systems within their body. Compartmentalized components have a variety of structures and functions to fulfill everyday tasks of biological organisms. For example, each human organ has a unique set of structural compositions and capabilities and can work together with each other to accomplish tasks crucial to human being's survival. One of the defining features that make up organs is tissue[27]. Depending on the location and function of the organ, the tissue's composition and structure differ. There are four main types of tissues in human body: epithelial, connective, muscle, and nervous tissues, and within each type, tissues are further divided into subcategories (**Figure 3.1**)[28]. Epithelial tissues form boundaries between different environments, such as between inside and outside of organs. They protect underlying tissues from radiation, desiccation, and toxins, and regulate excretion and secretion of chemicals[29]. Muscle tissues can be further divided into three categories: skeletal muscle, cardiac muscle and smooth muscle. Skeletal muscles are attached to the skeletal system via tendons and ligaments to maintain posture and control movements. Cardiac muscles are found only in the heart and are in charge of contractions and maintaining blood pressure. Smooth muscles are mostly found in the linings of numerous organs such as stomach and lung[30]. Nervous tissues exist in the central nervous system, which include brain

and spinal cord. Nervous tissues have crucial functions in integration and communication[31]. Connective tissue is a major component in the body and exist in all types of organs and have different functionalities depending on their locations, including but not limited to, binding and support, protection, insulation, and transportation. Loose connective tissues such as areolar and adipose are universal packing materials such as fat and store energy for the human body. Dense connective tissues typically have closely packed bundles of collagen bundles. They transfer movements from bone to muscle and prevent organs from tearing. Cartilage tissues maintain the shape of a specific structure while allowing flexibility and can also act as shock absorption (i.e., intervertebral discs). Bones are osseous tissues that are hard and lightweight in nature[32, 33].

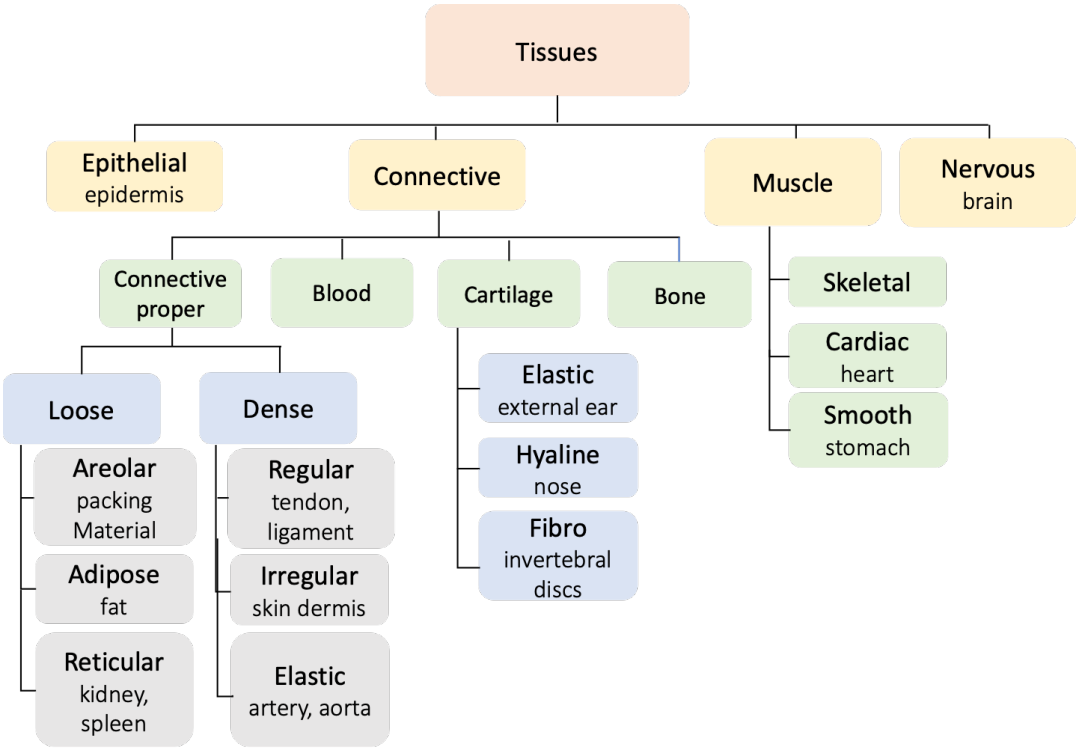

Figure 3.1: Tissue types and examples of organs and body parts that belong to each tissue type.

3.2 Collagen and Elastin

Depending on their categories, types, and functions, tissues exhibit different mechanical properties, namely, firmness and modulus. On structural level, two decisive factors that play important roles in the mechanical properties of tissues are collagen composition and architecture. Collagen occupies about 30% of protein mass in the human body and exists in fiber forms[9,34,35]. Collagen fibers are formed by three peptide chains that assemble into triple helices. To date, there are 28 types of collagens that have been discovered based on the amino acids that make up the peptide chains. Five most common collagens are: collagen I, found in skin, tendon, bone; collagen II, found mostly in cartilage; collagen III: main component of reticular fibers; collagen IV: mostly found in basal lamina, the epithelium-secreted layer of the basement membrane; collagen V: found in cell surfaces such has hair and placenta. Collagens can further be categorized according to their structural organization. The most common category of collagens is fibril-forming collagens, such as collagen I, II, II, V, where collagen fibers align parallelly to form thick cylindrical bundles. Fibril associated collagens with interrupted triple helices (FACIT) collagens, such as collagen IX, XII, XIX, XXI, do not form bundles but attach to other collagen bundles, and are responsible for signaling and cross-linking between collagens. Collagen IV, VIII, X are network forming collagens that can form rhombus or hexagonal shaped networks by covalent cross-linking. Collagen VII are anchoring fibrils that connect epidermis to dermis tissues. Collagen VI forms beaded filaments that are ubiquitous in connective tissues. They bridge and anchors cells to other components of the extracellular matrix.

In addition to collagen, another protein that influences the mechanical properties of tissues is elastin. While collagen contributes to the tensile strength of tissue, elastins help

tissue stretch and recoil, preventing tissue from being overly stretched. Elastins are composed of highly disordered peptide chains that oppose both stretching and tight packing since they restrict the number of conformations available to elastins. Elastic tissue, such as artery and blood vessels, is a subcategory of dense connective tissues that contains a large amount of elastin fibers. The combination of collagen and elastin gives biological tissues their unique nonlinear elasticity. The deformation of tissue is characterized by two stages: an elastic deformation followed by rapid stiffening when a small strain is applied[12-14], as discussed in **Section 2.2**.

3.3 Tissue mechanical properties by categories and functions

Stress-strain curves of 126 soft tissue samples were obtained from 60 literature sources (**APPENDIX 1**). The figures in the literature were digitized in Origin Lab and the data obtained after digitization were fitted according to the process described in **Section 2.2**.

Soft tissues, defined as Young's modulus less than 10^7 Pa, were selected for this study. Each tissue sample obtained from literatures was assigned to a category, based on the most prominent type of tissue in the sample, resulting in 11 categories: adipose, cardiac muscle, cartilage, dense irregular, dense regular, elastic, epithelial, nervous, reticular, and skeletal muscle. **Figure 3.2** showed the average firmness β and Young's modulus E_0 for each tissue category. The average modulus for all tissue categories was between 10^4 - 10^6 Pa, however; a wide range of firmness was observed. The reticular tissues had the lowest average firmness, which could be due to the presence of network-forming collagen fibers, i.e., reticular fibers. Nervous tissue category contained only brain tissues and had the second lowest average firmness. The other 9 categories of tissues had high average firmness in the

range of (0.8, 0.95). Among them, dense regular, cartilage, and cardiac muscle tissues had the highest average firmness around 0.9, indicating that these types of tissues are most resistant to deformation.

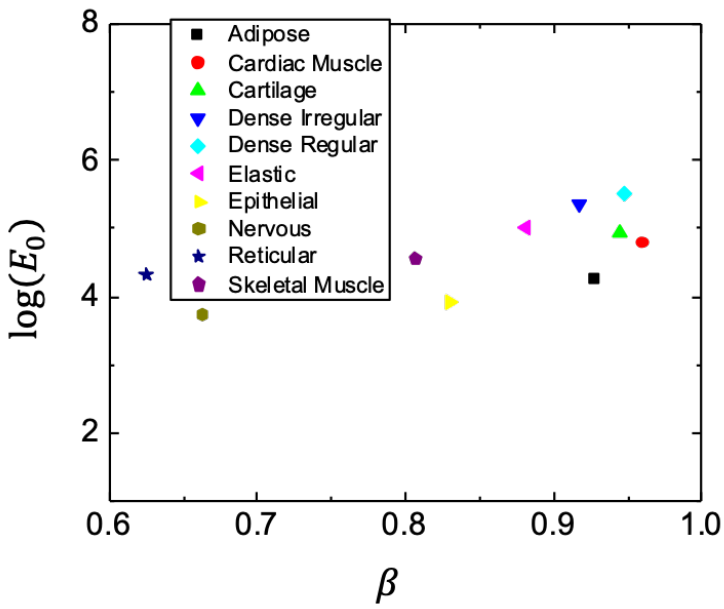

Figure 3.2: Average firmness β and Young's modulus E_0 of tissues according to categories.

Figure 3.3 showed the firmness and Young's modulus of every tissue in this study, grouped by category. Majority of the tissues' firmness were between 0.8 and 0.99 and their average Young's modulus had 10^5 Pa order of magnitude. Dense regular tissues, specifically tendons and ligaments, separated themselves from this group. They had exceptionally high firmness (> 0.9) and high modulus (10^6 Pa). Nervous and reticular tissues had lower modulus (~ 10^4 Pa) and a wider range of firmness. Since majority of tissue categories fell into the same range, the mechanical properties differences in tissues did not originate from tissue types.

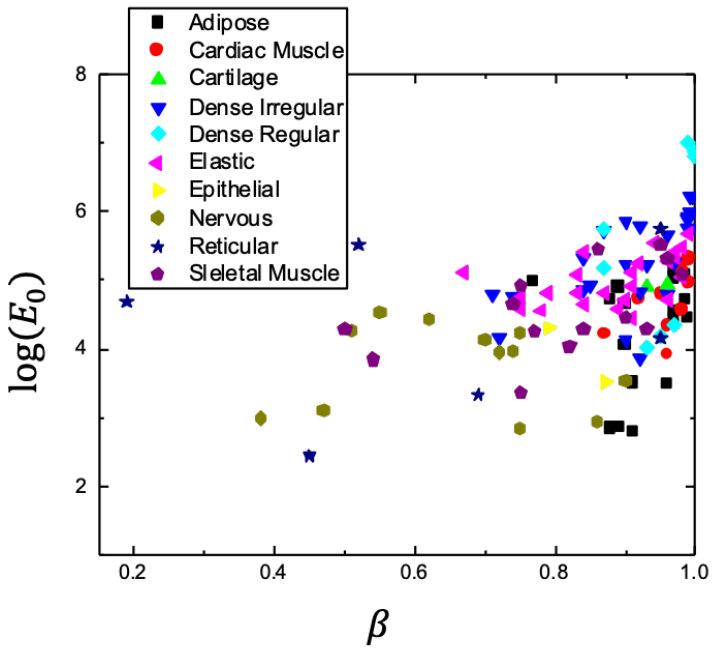

Figure 3.3: Young's modulus E_0 vs. firmness β of tissues grouped by categories.

Next, grouping tissues by their functionalities was investigated. The tissues were divided into 7 groups according to their functions: shock absorbance, barrier, insulation, blood pressure maintenance, movement, tearing prevention, and force transfer. Examples of shock absorbance include intervertebral discs, where fibrocartilages are found between bony vertebrae and knee meniscus. Epithelial tissues, such as fetal membrane, serve as barriers between the organ and its external environments. Tissues such as adipose, areolar, and brains are examples of insulation tissues. Cardiac muscles, such as heart valves, are tissues that maintain blood pressure as they have sophisticated and delicate control of heart contractions and pumping. Movement tissues are essentially skeletal muscles that control the movement of human bodies. Tissues that prevent tearing are mostly dense irregular tissues such as skin dermis, pericardium, and cornea. Dense regular tissues such as ligaments and tendons are in

charge of transfer forces from bone to muscles. According to **Figure 3.4**, tissues that are responsible for insulation has the lowest modulus and a wide range of firmness. Since insulation tissues do not tend to undergo external forces such tension and compression, it has lower Young's modulus and lower firmness. Opposite to insulation tissues, tissues that transfer forces have the highest modulus and firmness, as they need to resist high tensile stress. Right beneath force transfer tissues are tissues that prevent tearing. These tissues are slightly more flexible than tissues that transfer forces as they have a wider range of firmness, but their firmness still fall into the high range. These tissues can be stretched, but not to a great extent.

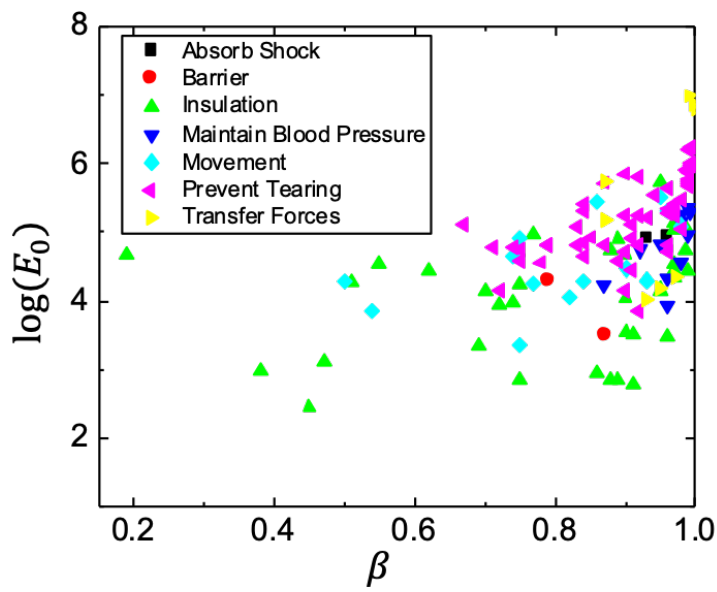

Figure 3.4: Young's modulus E_0 vs. firmness β of tissues grouped by functions.

Though tissues that maintain blood pressure have the same range of modulus to tissues that control movements, but they have a tighter firmness range, to prevent themselves

from being over-stretched. This was reflected in **Figure 3.5**, where the mechanical properties of skeletal muscles (movement) and cardiac muscles (blood pressure maintenance) were compared side to side. Though both groups have the same range of modulus (10^4 - 10^5 Pa), tissues that maintain blood pressure, i.e., cardiac muscles, have much lower range of firmness (0.8 - 0.9) compared to tissues in charge of movement (skeletal muscles). This difference reflects that organs' evolutions are closely tied to their functionalities. Since cardiac muscles have the essential function to control heart's contraction and pumping, it is crucial for them to maintain a stable shape and hence results in very limited flexibility and involuntary movement. On the other hand, skeletal muscles are much more flexible as animals such as invertebrates, need to be able to move around freely and have voluntary control of their movements.

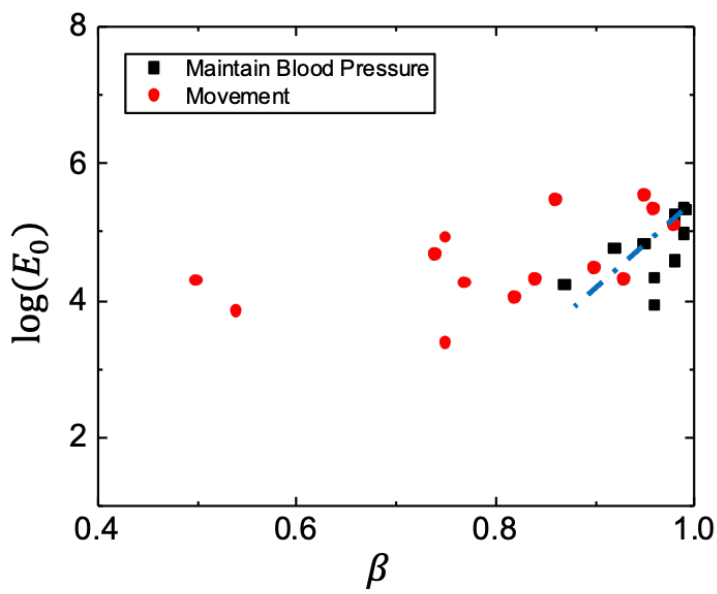

Figure 3.5: Young's modulus E_0 vs. firmness β of muscle tissues grouped by functions.

3.4 Tissue mechanical properties by collagen structural organization

Since the firmness of the majority of the tissues was higher than 0.5, several folds higher than common synthetic tissue mimics, this study focused on tissues with $\beta > 0.5$. As introduced in **Section 3.2**, the structural component responsible for tissues' mechanical properties is collagen fibers. Although the majority of tissues' main collagen component is collagen I, they still exhibit different mechanical properties. For example, both tendon and arteries' major collagen component is collagen I[10], but artery tissues had lower average firmness than tendons. Such distinctions could arise from the difference in collagen architectural organizations. Collagens can assemble into different morphologies and form different types of networks, similar to synthetic polymers can be manufactured to for different networks[9]. To study the influence of collagen architectures of tissues on their mechanical properties, microscopic pictures of each tissue used in this study were examined to find the underlying collagen architecture. Consequently, the tissues were divided according to the 7 types of architectures summarized based on microscopic pictures found in previous literatures[35-54] (**Figure 3.6**): densely aligned bundle, meshlike network, parallel array, multidirectional bundle, interweaving bundle, loosely woven network, rhombus network. Note that there was an 8th category, where very small percent of collagens (< 6%) were scarcely distributed in the extracellular matrix[36]. Furthermore, some literature sources measured singular collagen fibers isolated from the tissue, and hence these samples were referred as "singular fiber".

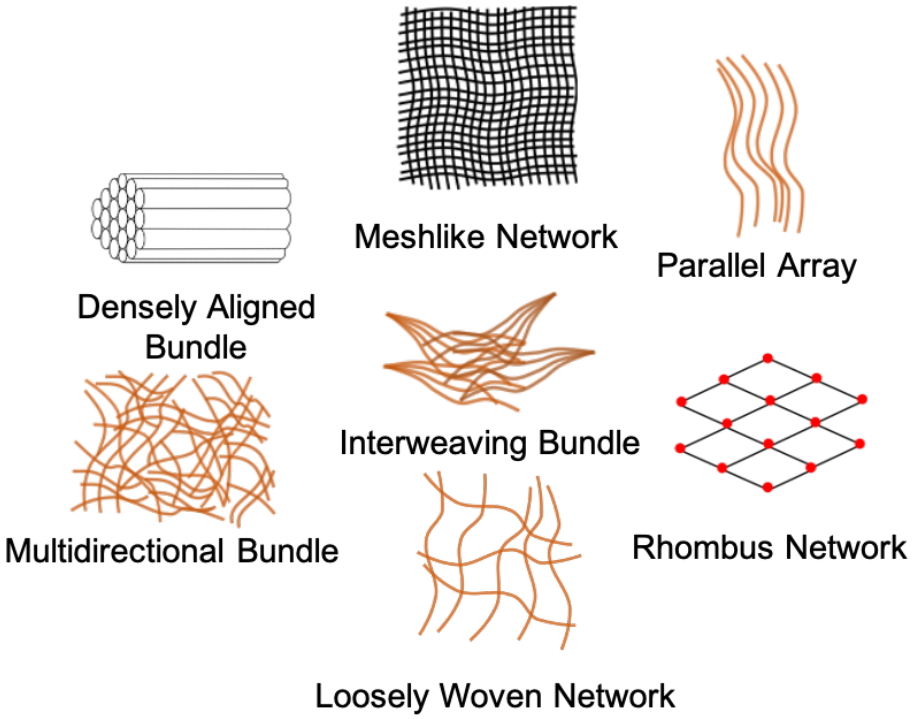

Figure 3.6: Different types of collagen structural organization.

The mechanical properties of tissues grouped according to collagen architectures were displayed in **Figure 3.7**. As shown in **Figure 3.7**, densely aligned bundles[35,37-39] had the highest modulus, close to 10^7 Pa, as well as high firmness, which was in the range of (0.99, 1). Tissues that had mesh-like network collagen architectures[40] also had very high firmness, similar to the densely aligned bundles, with modulus 0.5 - 1 order of magnitude lower. Tissues with multidirectional bundle[41-44] and parallel array[45-49] organizations overlapped in the modulus vs. firmness map. Both had a relatively wide range of firmness (0.6 - 0.95) and a modulus range between 10^4 - 10^5 Pa. Note that although densely aligned bundles and parallel arrays had a similar pattern, they should not be mixed in the same category, as parallel arrays often contain other substances, distributed among the spaces between fibers. For example,

parallel arrays in skeletal muscles have cable-like networks, capable of expanding[47]. Elastic tissues have elastins distributed throughout the parallel collagen fibers, which allow the tissues to stretch and recoil[48]. Tissues with interweaving bundles architecture occupied a unique region in **Figure 3.7**: moderate modulus but high firmness, this corresponded to the cardiac muscles in charge of maintaining blood pressure[51,52]. A high firmness but moderate modulus allow heart muscles to contract and pump blood without being over-stretched. Tissues with loosely woven networks[52,53] had slightly lower modulus compared to parallel arrays and multidirectional bundles. Singular collagen fibers and tissues with very low collagen content scarcely distributed in the extracellular matrix had the lowest modulus and the widest range of firmness, along with tissues with rhombus-shaped network[54].

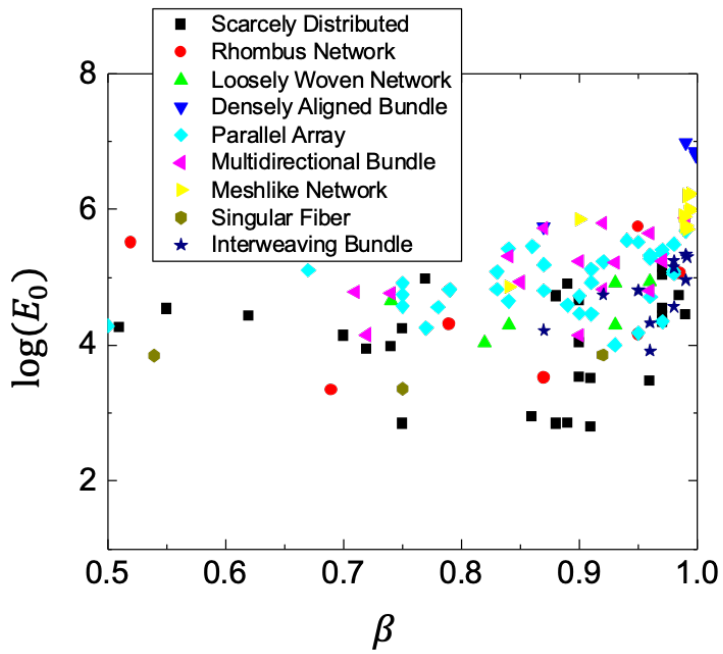

Figure 3.7: Young's modulus E_0 vs. firmness β of tissues grouped by collagen structural organization.

CHAPTER 4

Synthetic Strategy for Bio-mimicking Multifunctional Materials

4.1 Previous work

A plethora of work has been conducted to construct chameleon-like materials that possess both non-linear elasticity and structural coloration. In particular, the lamellar morphology (1D) has been widely used in photonic materials. Grubbs et al. have reported using bottlebrush block copolymer (BBCP) as a multilayer photonic material[55]. Poly(isocyanate) based macromonomers were copolymerized by ring opening metathesis polymerization (ROMP) (**Figure 4.1 A)**. Controlling the degree of polymerization (DP) of each block allowed the BBCP to self-assembly into lamellar structures with varied periodicity. When the DP increased, λ_{max} red shifted according to reflectance spectroscopy, which indicated an increase in domain spacing (**Figure 4.1 B**).

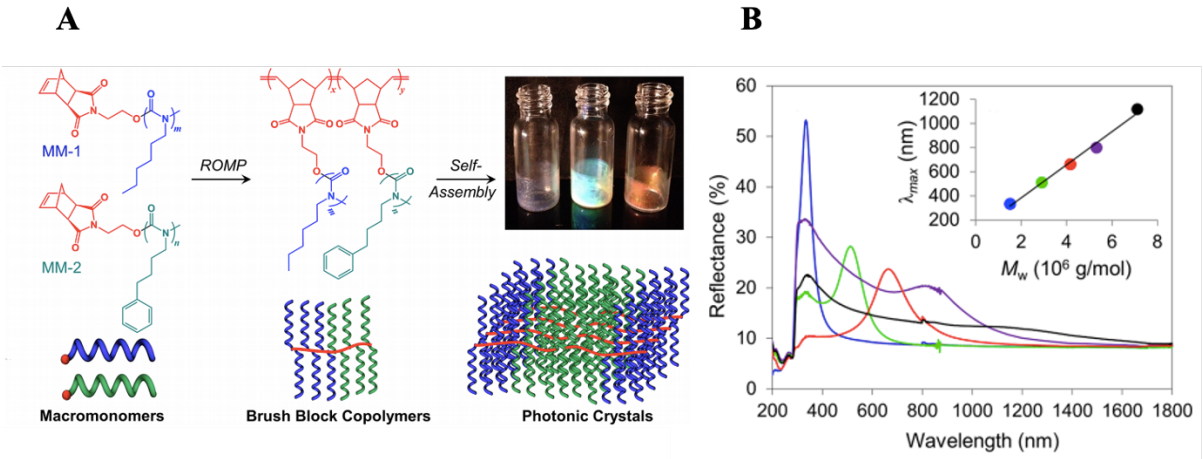

Figure 4.1: 1D multilayer photonic crystal assembled from poly(isocyanate) based bottblebrush copolymers (BBCPs)[55]. (A) Chemical structure and assemble morphology of BBCPs. **(B)** Reflectance spectroscopy of BBCPs.

Although BBCPs have the advantage to quickly assemble into lamellar morphology and display a wide range of color with varied DP of each block, they lack the flexibility of biological tissues, as well as the ability to change their colors once assembled.

Two rationales are commonly used when designing materials with tunable colors: changing refractive indices contrast and changing domain spacing. Miguez et al. constructed lamellar like structures by fabrication of silicon/titanium oxide hybrid nanoparticles. The two-component system was formed by the hybrid material and air. Air has a low refractive index and with the introduction of solvent vapor, a significant decrease in reflectivity occurred due to diminished refractive index contrast (**Figure 4.2**)[56].

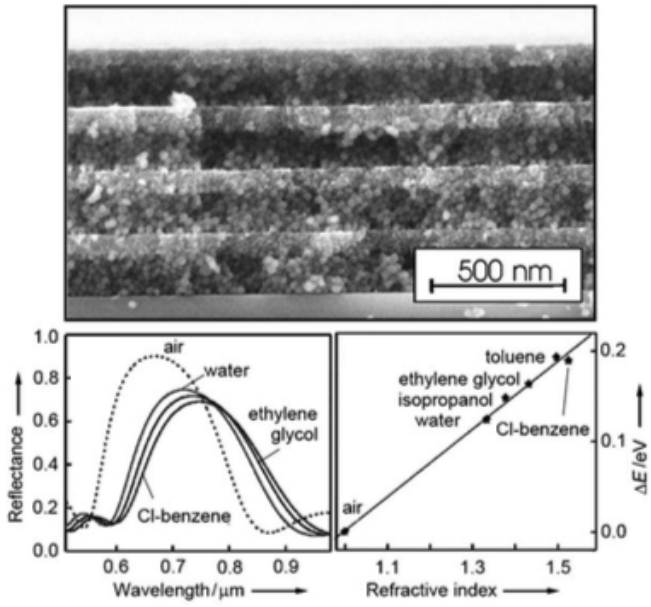

Figure 4.2: Silicon/titanium oxide hybrid nanoparticles macroscopic structure and corresponding reflectance change upon exposure to solvent vapors[56].

While these assembled nanoparticles have tunable reflectivity, they are brittle and stiff, hence lacking the desired stretchable and soft mechanical properties that are commonly observed in biological tissues. In order to introduce elasticity while preserving the lamellar, Gong et al. sandwiched a poly(acrylamide) (PAAm) hydrogel between poly(dodecylglyceryl itaconate (DGI)) layers resulting in materials that possessed lamellar-like macroscopic structure and were flexible at the same time. PolyDGI formed rigid bilayers with interior hydrophilic tails and exterior hydrophobic DGI heads. Compressible PAAm hydrogels were then inserted into these bilayers yielding an orange material at zero strain. When the materials were compressed, the spacing between polyDGI bilayers decreased, which caused the reflected wavelength to blue shift, as shown in both pictures of the material and reflectance spectrum[57] (**Figure 4.3**).

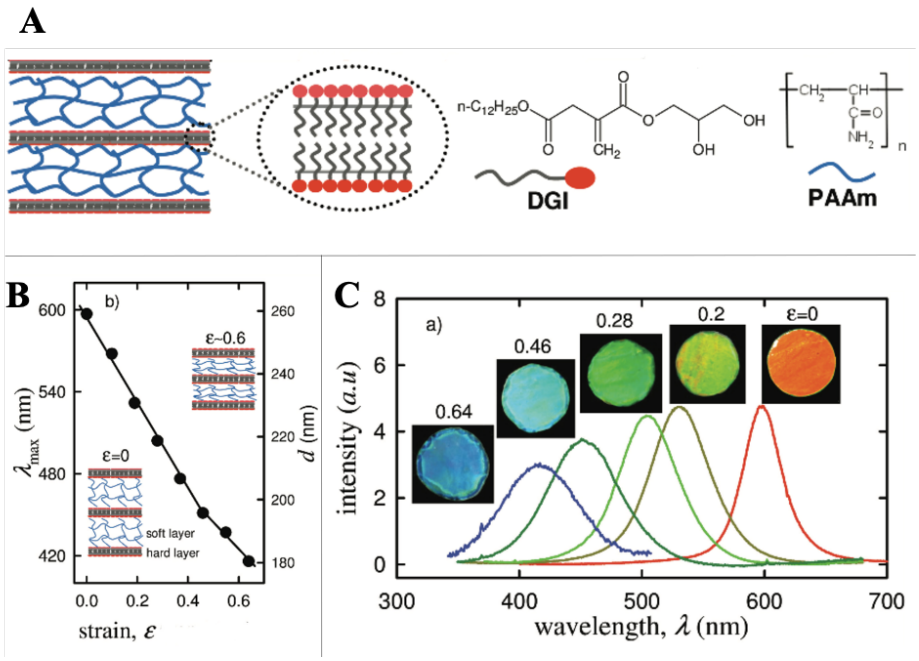

Figure 4.3: 1D photonic materials capable of changing color upon mechanical stimuli[57]. (A) The materials were fabricated by inserting PAAm hydrogel between amphiphilic poly(DGI) layers. **(B)** Reflected wavelength decreased when materials were compressed. **(C)** Reflectance spectroscopy of photonic material with respect to compression.

To summarize, current materials are able to mimic partial properties of chameleon-like tissues. However, these materials either lack tissue-like mechanical properties (as in the case of Grubbs), or requires blending of multiple materials (as in the case of Gong). Therefore, the goal remains: construct materials assembled from one single molecule that possess both tissue-like mechanical properties and change color upon stimuli.

4.2 Synthetic Strategy

To address this challenge, we introduced linear–bottlebrush–linear (LBL) triblock copolymers that microphase separate to yield thermoplastic elastomers (or plastomers) (**Figure 4.4**)[58] analogous to linear triblocks[59-62]. However, bottlebrush strands are architecturally disentangled and extended within LBL networks[63-66], which generates a strong non-linear modulus increase with deformation[63,67,68]. Concurrently, microdomains of flexible linear blocks serve as hidden length reservoirs that unravel at larger deformations[58,69,70]. This oxymoronic combination of *supersoft* matrices composed of *stiff* brush macromolecules and *hard* microdomains composed of *flexible* linear chains creates the tissue-like stress-strain response. Furthermore, specific mechanical properties and optical properties, such as Young's modulus (E_0), firmness (β), and elongation-at-break (λ_{max}), reflected wavelength, can be encoded into the LBL architecture by controlling degrees of polymerization (DP) of linear blocks (n_L), bottlebrush blocks (n_{bb}), and bottlebrush side chains (n_{sc})[68].

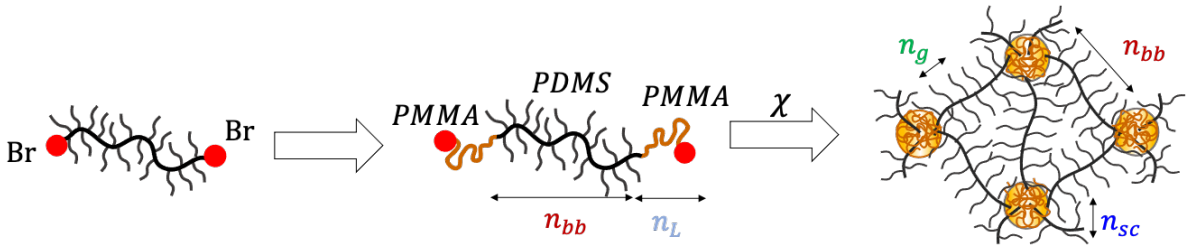

Figure 4.4: Linear-bottlebrush-linear (LBL) triblock copolymers micro-phase separate into physical networks (plastomers). Linear poly(methyl methacrylate) (PMMA) was grown from both ends of the poly(dimethylsiloxane) (PDMS) bottlebrush, resulting in linear-bottlebrush-linear triblock copolymers which self-assemble into physical networks and resemble the mechanical properties of biological tissues. n_{bb}: DP of P(PDMS$_{11}$MA) bottlebrush, n_L: DP of linear PMMA block on each end, n_g: grafting density of P(PDMS$_{11}$MA) bottlebrush, n_{sc}: side chain length of the P(PDMS$_{11}$MA) bottlebrush, χ: Flory-Huggins interaction parameter.

CHAPTER 5

Synthesis of Linear-Bottlebrush-Linear (LBL) Triblock Copolymers

5.1 Synthetic Scheme

To gain precise synthetic control of n_L and n_{bb}, we employed atom transfer radical polymerization (ATRP), to produce polymers with narrow molecular weight distribution and well-defined architectures[71,72]. **Figure 5.1** outlines the two-step synthesis of *LBL* copolymers. First, P(PDMS$_{11}$MA) bottlebrushes with Br-terminated chain ends were prepared by grafting-through polymerization of PDMS$_{11}$MA macromonomers with a difunctional ATRP initiator, 2-EBiB. After reaching a desired n_{bb}, the reaction was quenched, and the bottlebrush solution was precipitated several times into methanol to remove unreacted macromonomer. Purified bottlebrush macroinitiators were then used to grow either linear PMMA or poly(benzyl methacrylate) (PBzMA) at both ends. Typical dispersity of the bottlebrush macroinitiator and the corresponding LBL copolymer was Đ≅1.5 **(Figure 5.2)**.

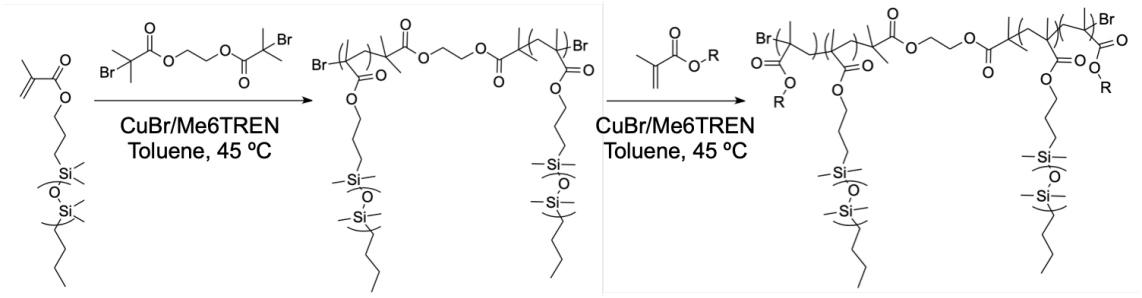

Figure 5.1: Two-step synthesis of linear-bottlebrush-linear triblock copolymers. The triblock contained a P(PDMS$_{11}$MA) bottlebrush block and linear PMMA blocks at both ends. Macromonomer PDMS$_{11}$MA has 11 Si atoms but totally 28 atoms (10 O atoms and 7 C atoms, forming a side chain. We use $n_{sc} = 14$ as a number of effective monomeric units per side chain by analogy with 14 vinyl monomeric units forming a chain with 28 atoms.

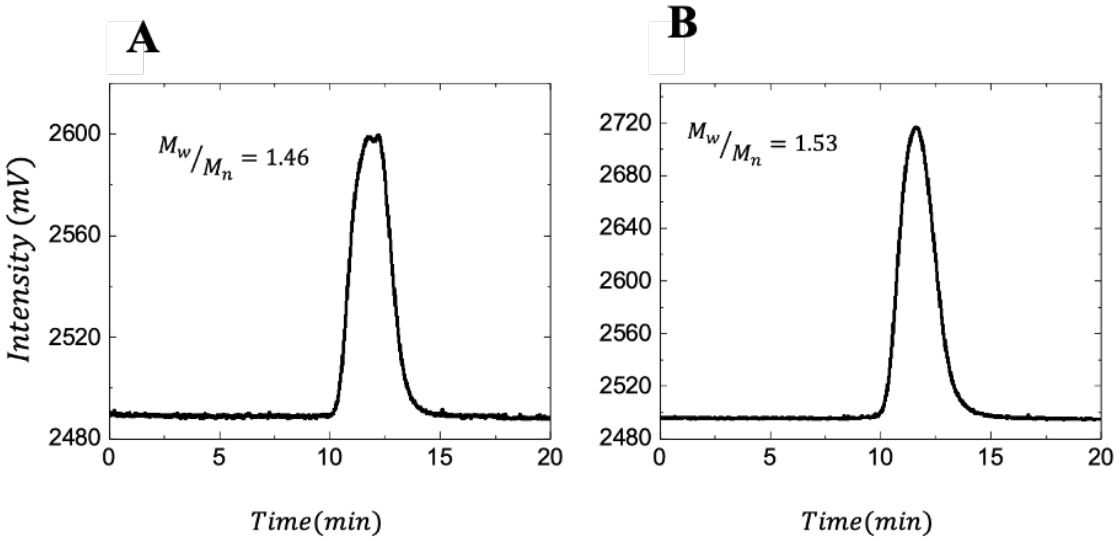

Figure 5.2: Gel permeation chromatography (GPC) spectra of bottlebrush and triblock copolymers. (A) Multi-angle light scattering gel permeation chromotography (MALS-GPC) spectrum of $P(PDMSMA)_{830}$. **(B)** MALS-GPC spectrum of $PBzMA_{500}$-*b*-$P(PDMS_{11}MA)_{860}$-*b*-$PBzMA_{500}$.

5.1.1 Synthesis of ethylene bis(2-bromoisobutyrate) (2-BiB)

The synthesis was adapted from a literature with some modifications[73]. Ethylene glycol (14.43 g, 0.23 mol) was added under nitrogen to a flask containing a magnetic stirring bar and placed in an ice bath. Anhydrous THF was added into the flask. Triethylamine (60 mL, 3 eq.) was added to the reaction mixture. 2-Bromoisobutyryl bromide (120 g, 2.2 eq.) was added dropwise to the reaction mixture with a syringe pump. After a complete addition, the reaction mixture stirred at 0 °C for extra one hour and then at ambient temperature overnight. The mixture was filtered, and the volatile compounds were removed by rotary evaporation. The resulting brown solution was dissolved in chloroform and treated with 1M HCl solution, saturated $NaHCO_3$ solution and three times with deionized water. The organic layer was dried over dry $MgSO_4$. The volatile compounds were removed with vacuum to give a light brown solid. This sample passed through a column to purify and achieve pure creamy white crystal

after drying sample. Nuclear magnetic resonance (NMR) spectrum was used to confirm the success of synthesis (**Figure 5.3**).

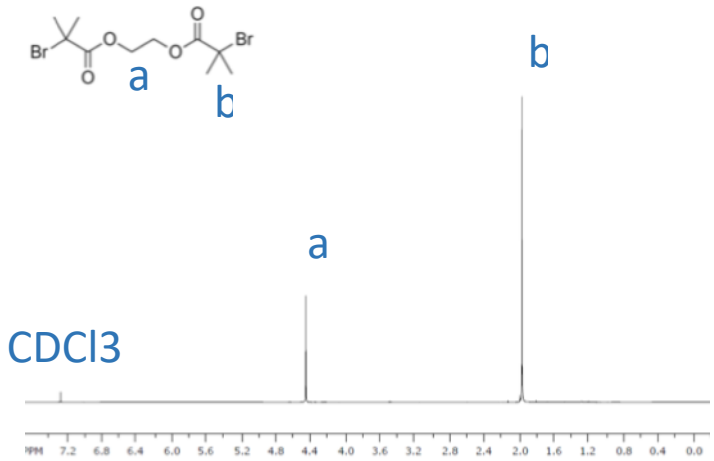

Figure 5.3: ^{1}H-NMR spectrum of purified 2-BiB in $CDCl_3$ (400 MHz).

5.1.2 Synthesis of $PDMS_{11}MA$ bottlebrush

In a typical synthesis, $PDMS_{11}MA$ macromonomer (MW = 1000 g/mol, $n_{sc} = 14$) was dissolved in toluene, as a 0.4 M solution. Difunctional initiator ethylene bis(2-bromoisobutyrate) (2-BiB) was added according to a targeted DP, which was calculated by $[M]_0$:[I], along with $Cu^{(I)}Br$, and tris[2-(dimethylamino)ethyl]amine (Me_6TREN), where the molar equivalents of the catalyst and ligand relative to initiator were [I]:[$Cu^{(I)}Br$]:[Me_6TREN] = 1:2:2 ([I] was calculated as the moles of 2-BiB divided by the volume of the reaction volume). The reaction temperature was kept at 45 ºC for the duration of the polymerization. The conversion was confirmed by ^{1}H NMR. After desired conversion was reached, the reaction was quenched by air and the reaction mixture was washed in methanol six times to remove unreacted macromonomers and copper catalysts. The purified

bottlebrush was dried overnight. **Figure 5.4** showed the NMR of a purified $PDMS_{11}MA$ bottlebrush.

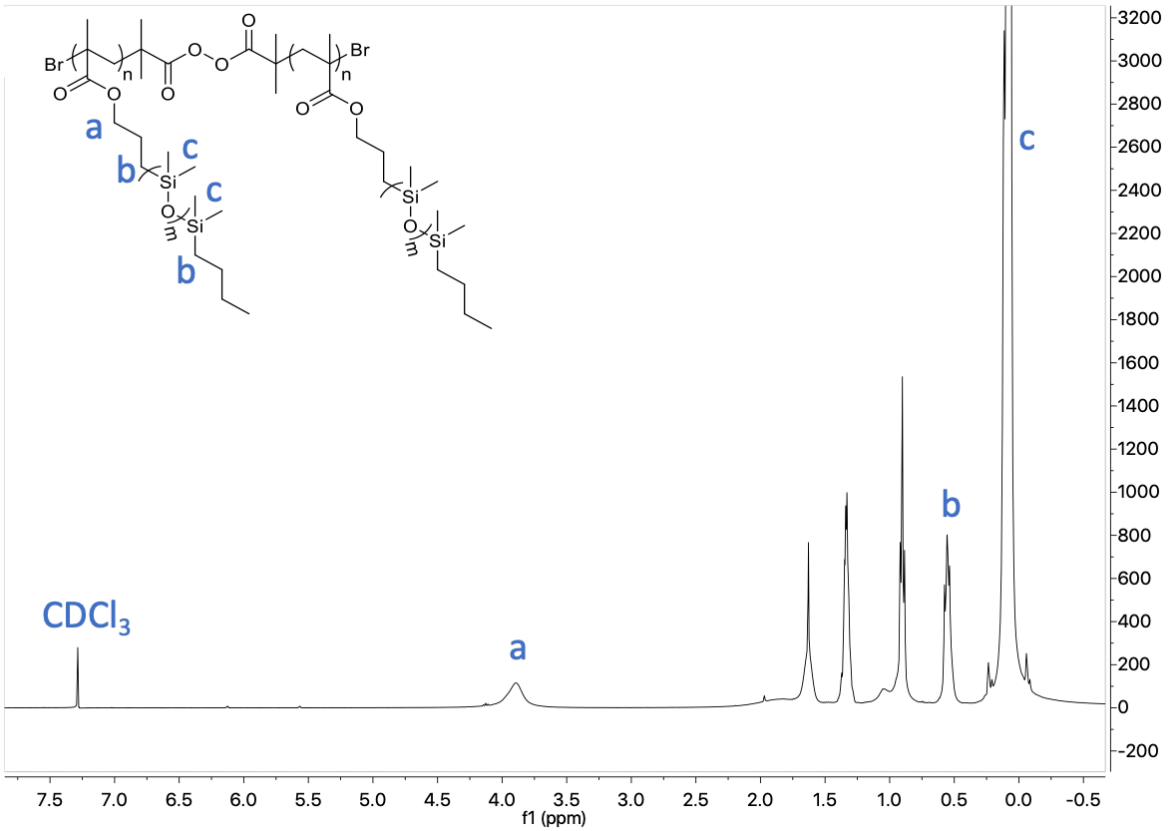

Figure 5.4: ^{1}H-NMR spectrum of purified $PDMS_{11}MA$ bottlebrush in $CDCl_3$ (400 MHz).

5.1.3 Synthesis of L-B-L Linear-Bottlebrush-Linear triblock copolymer

To prepare L-B-L triblock copolymers, synthesized and purified PDMS bottlebrushes were used as macroinitiators to grow linear methacrylate side-blocks at both ends. Here we use poly(benzyl methacrylate)-bbPDMS-poly(benzyl methacrylate) (PBzMA-bbPDMS-PBzMA) as an example. In a typical synthesis, 5.44 g of bbPDMS macroinitiator (n_{bb} = 860, 6.33 µmol), 5 g of BzMA (280 mM), 6.6 µL Me6TREN (25 µmol), and 30 mL toluene were added to a 100

mL Schlenk flask equipped with a stir bar. The solution was degassed by nitrogen gas for 1.5 hrs and then 3.6 mg of CuBr (25 25 µmol) was quickly added to the Schlenk flask and the reaction mixture was then degassed for another 5 minutes. The flask was immersed in a 45ºC oil bath until desired conversion was reached (verified by 1H-NMR). The reaction was then quenched by exposure to air and dried. The crude product was dissolved in DCM and precipitated in methanol three times to remove unreacted BzMA monomers and copper catalysts. The pure products were dried with airflow to remove DCM and methanol. and vacuumed overnight. The DP and mass ratio of linear end bocks were measured by 1H-NMR (CDCl3, Brüker 400 MHz spectrometer) as shown in **Figure 5.5** for PBzMA-*b*-P(PDMS$_{11}$MA)-*b*-PBzMA

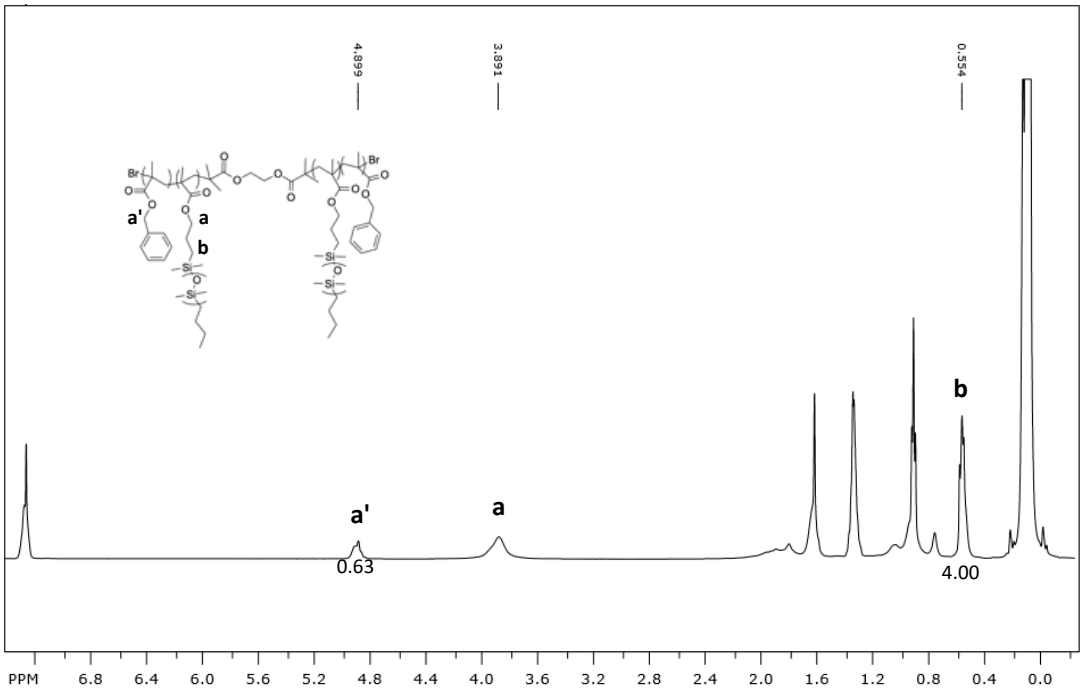

Figure 5.5: **^{1}H-NMR of PBzMA-*b*-P(PDMS$_{11}$MA)-*b*-PBzMA (400 MHz, CDCl3)**: 3.89 (-C**H2**-O-C=O, br, 2H), 4.9 (O-C=O-C**H2**-C6H5, s, 2H), 0.54 (COO-CH2-CH2-C**H**2-Si(CH3)2, t, 4H). $n_L = {Area(a')}/{2} * {Area(b)}/{4} * n_{bb}$.

Using the same method described above poly(methyl methacrylate)-*b*- P(PDMS$_{11}$MA)-*b*-poly(methyl methacrylate) (PMMA-*b*-P(PDMS$_{11}$MA)-*b*-PMMA) was synthesized (**Figure 5.6)**.

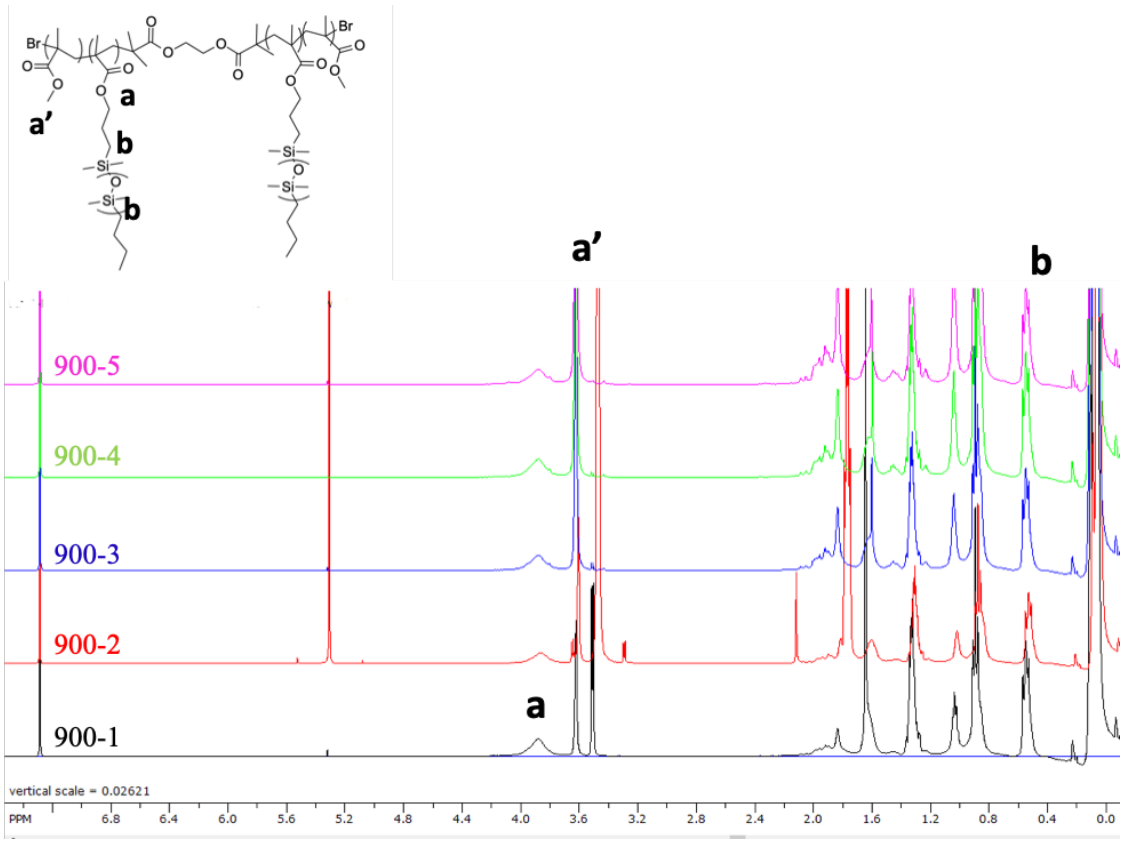

Figure 5.6: ^{1}H-NMR of PMMA-*b*-P(PDMS$_{11}$MA)-*b*-PMMA (400 MHz, CDCl3): 3.9 (-C**H2**-O-C=O, br, 2H), 3.62 (COO-C**H3**, s, 3H), 0.54 (COO-CH2-CH2-C**H**2-Si(CH3)2, t, 4H).$n_L = {Area(a')}/{3} * {Area(b)}/{4} * n_{bb}$.

5.2 Synthetic challenges

Despite this highly optimized method, termination events such as biradical combination or chain transfer remain a challenge when employing ATRP for grafting-through polymerization of macromonomers. Compared to small molecules, bulky macromonomers have slower rates of propagation and observable equilibrium monomer concentrations where

the rate of propagation equals the rate of depropagation when [M] reaches its equilibrium monomer concentration, $[M]_e$. Polymerization does not occur when $[M]_0 < [M]_e$[74]. The slow rate of polymerization, relative to the rates of chain breaking reactions such as termination and transfer reactions, and the contribution of depolymerization could lead to a greater challenge in achieving both high yield and chain end functionality. Loss of chain end functionality is detrimental to the synthesis of LBL triblock copolymer as it results in undesired linear–bottlebrush diblocks (LB) and bottlebrush homopolymer (B) impurities (**Figure 5.7A**). Due to the high molecular weight and similar solubility parameters, these side products are difficult to isolate by common purification techniques such as precipitation or dialysis; therefore, they could remain in the final materials and affect their mechanical properties. The effect of these impurities on the stress-strain response of LBL plastomers was demonstrated by varying polymerization conditions (**Figure 5.7B**). Plastomers with the same targeted chemical and architectural composition from two different batches demonstrated significant difference in mechanical properties (**Table 5.1, 5.2**).

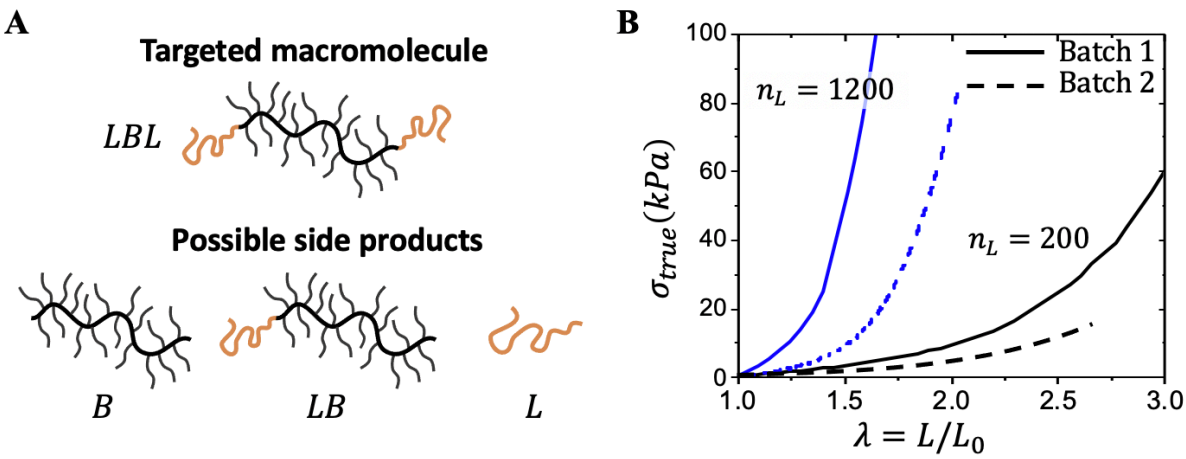

Figure 5.7: Possible side products that caused inconsistencies in plastomer mechanical properties. (A) Possible side products of *LBL* synthesis: bottlebrush homopolymer (*B*), linear-bottlebrush diblock (*LB*), linear PMMA homopolymer (*L*). **(B)** Two batches of two different plastomers $PMMA_{1200}-b-P(\text{PDMSMA})_{900}-b-PMMA_{1200}$ (blue) and $PMMA_{200}-b-P(PDMSMA)_{900}-b-PMMA_{200}$ (black) demonstrate significant variation of stress-elongation curves upon uniaxial extension at $\dot{\varepsilon}= 0.008s^{-1}$,T = 25°C. For both batches, the initial macromonomer concentration were 0.4 M and the reaction were run in toluene at 45 ºC. Macroinitiator synthesis for batch 1 was quenched at 74% conversion and that for batch 2 was quenched at 83% to reach the same $P(PDMSMA)_{900}$ chain length.

Table 5.1: **Mechanical parameters of $PMMA_{1200}$-b-P(PDMSMA)$_{900}$-b-$PMMA_{1200}$**

Batch	β	E_0 (kPa)
1	0.67	39.3
2	0.58	9.19

Table 5.2: **Mechanical parameters of $PMMA_{200}$-b-P(PDMSMA)$_{900}$-b-$PMMA_{200}$**

Batch	β	E_0 (kPa)
1	0.29	5.40
2	0.20	2.95

Accordingly, comparison of two identical plastomers before and after extraction with hexane (**Figure 5.8**) showed significant stiffness increase after removal of free bottlebrushes

(**Table 5.3, 5.4**), which were present between 25-29 wt% relative to the total yield of LBL plastomer (**Table 5.5, Figure 5.9**).

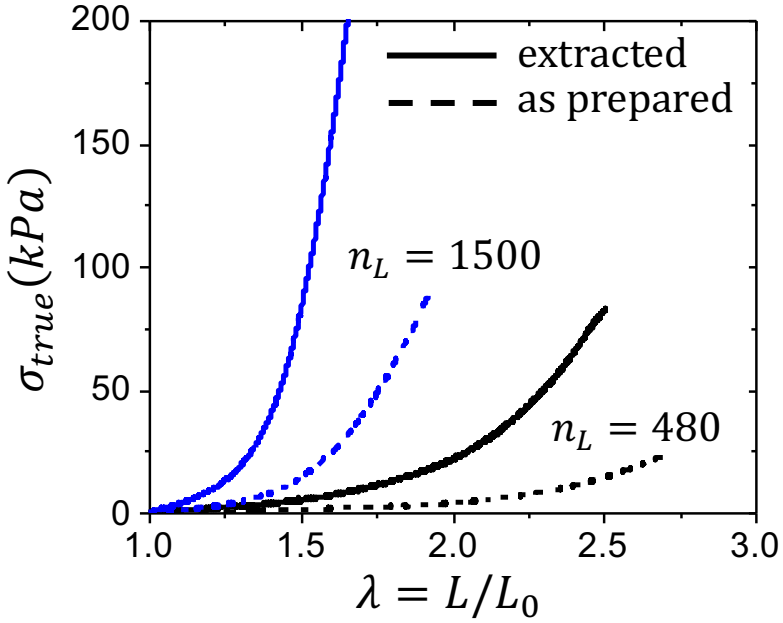

Figure 5.8: Difference between stress-elongation curves of plastomers before and after extraction. Stress-elongation curves of two LBL plastomers $PMMA_{1500} - b - P(PDMSMA)_{940} - b - PMMA_{1500}$ (blue) and $PMMA_{480} - b - P(PDMSMA)_{940} - b - PMMA_{480}$ (black) show significant difference in stress-elongation response before (dashed lines) and after (solid lines) extraction of free B-blocks from the plastomer samples.

Table 5.3: Mechanical parameters of $PMMA_{1500}$-b-$P(PDMSMA)_{900}$-b-$PMMA_{1500}$ before and after extraction with hexane

	β	E_0 (kPa)
Before	0.65	10.8
After	0.75	35.4

Table 5.4: Mechanical parameters of $PMMA_{480}$-b-$P(PDMSMA)_{900}$-b-$PMMA_{480}$ before and after extraction with hexane

	β	E_0 (kPa)
Before	0.28	2.1
After	0.36	8.3

Table 5.5: Free $P(PDMS_{11}MA)$ bottlebrushes extracted from LBL plastomers (Figure 5.8)

n_{bb}	n_L	wt% of $P(PDMS_{11}MA)$ extracted
940*	480	25
	840	24
	1500	29

* Degree of polymerization of bottlebrush backbone after 83.3% on macromonomer conversion at a targeted $n_{bb} = 1125$.

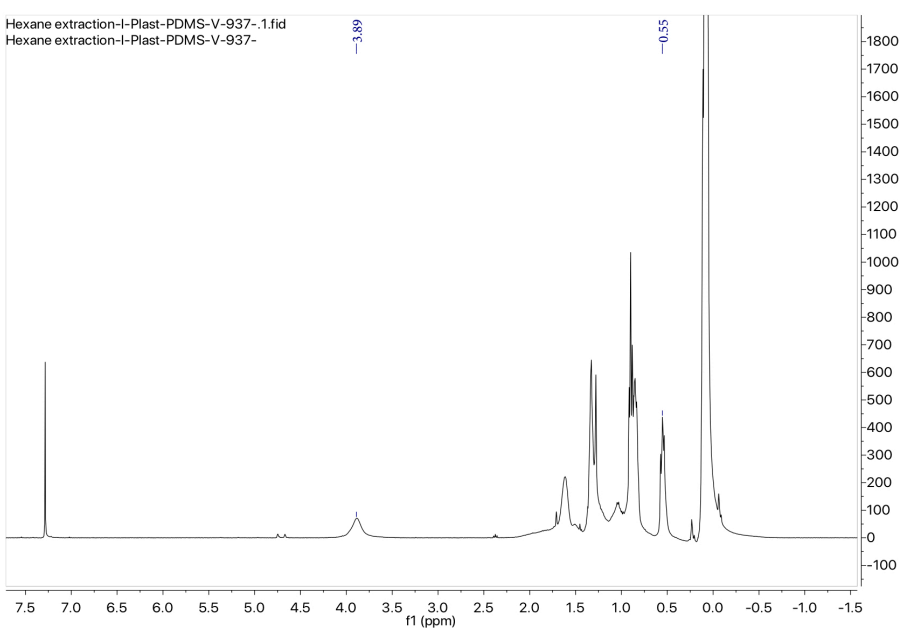

Figure 5.9: NMR of hexane extracted substance from triblock copolymers.

Conversely, we deliberately mixed P(PDMS$_{11}$MA) bottlebrush homopolymers with triblock copolymers during network self-assembly to demonstrate the plasticization effect on the stress-strain response (**Figure 5.10**). A significant decrease in modulus (~3.5x) is observed after the addition of only 21 wt% P(PDMS$_{11}$MA) bottlebrushes (**Table 5.6**), which is counter to traditional network swelling theory[75] as the presence of free P(PDMS$_{11}$MA) significantly alters the LBL plastomer self-assembly pathway of the L-domains. Therefore, the mechanics of LBL, LB, and B mixtures warrants a future study that will investigate specific contributions of free brush fraction and their architectural dimensions (n_{sc}, n_g, n_{bb}).

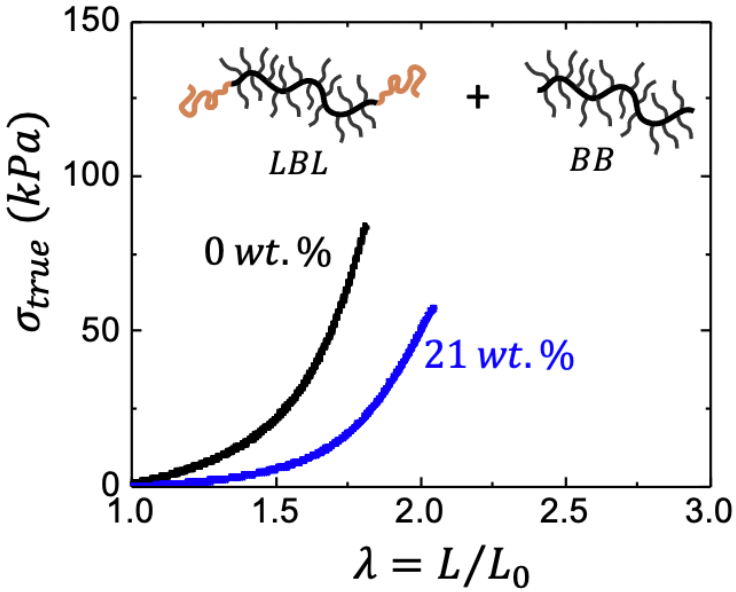

Figure 5.10: Effect of free bottlebrush impurities on plastomer stress-elongation response. The stress-elongation response changes upon adding 21 wt.% of free P(PDMS$_{11}$MA) (n_{bb} = 860) bottlebrushes to PBzMA$_{540}$-*b*-P(PDMS$_{11}$MA)$_{860}$-*b*-PBzMA$_{540}$ plastomers.

Table 5.6: Effect of bottlebrush impurity on the mechanical properties of $PMMA_{540}$-b-$P(PDMSMA)_{860}$-b-$PMMA_{540}$

Wt% of impurtity	β	E_0 (kPa)
0	0.54	25.5
21	0.52	7.1

Note that termination and chain transfer may also occur during linear block polymerization as observed by extractable linear homopolymers (**Figure 5.11**), but this does not significantly affect the resulting mechanical properties as (i) terminated LBLs are still mechanically active and average out over the entire network, and (ii) free homopolymer constitutes small fractions (2-4wt%). To test the impurity hypothesis, we mixed linear homopolymers into purified triblocks during self-assembly. Their mechanical performance did not noticeably deviate from the pure triblock (**Figure 5.11, Table 5.7**) and stresses the importance of minimizing termination and chain transfer in $P(PDMS_{11}MA)$ polymerization.

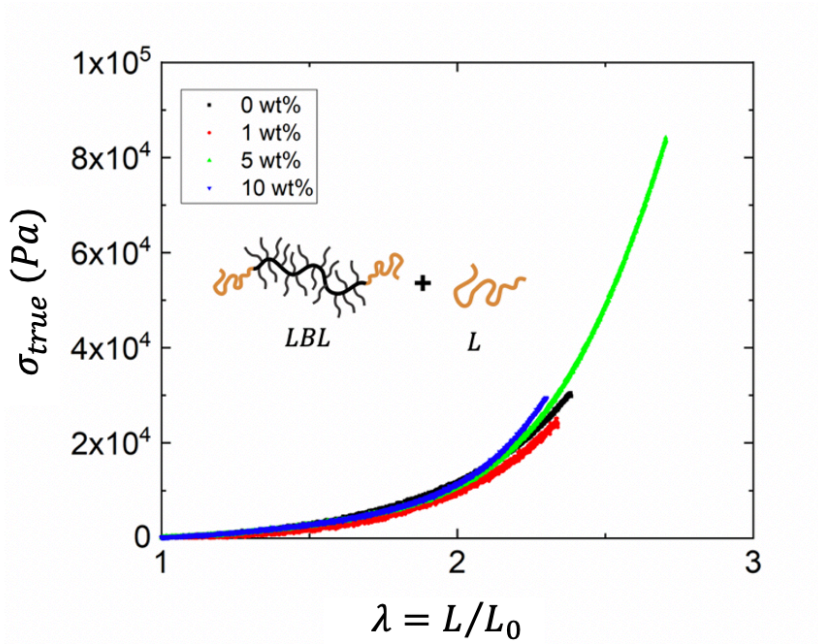

Figure 5.11: Effect of linear homopolymer impurity on plastomer stress-elongation response. The stress-elongation response changes upon adding 1.wt%, 5.wt%, and 10.wt% of free P(BzMA) homopolymers to $PBzMA_{330}$-*b*-$P(PDMS_{11}MA)_{900}$-*b*-$PBzMA_{330}$ plastomers.

Table 5.7: Mechanical properties of pure triblocks and mixtures with linear homopolymers.

Wt%	β	E_0 (kPa)
0	0.29	5.7
1.0	0.33	4.1
5.0	0.34	4.5
10.0	0.34	4.6

5.3 Optimizing synthesis conditions

To summarize, impurities such as bottlebrush homopolymers and linear-bottlebrush diblocks affect the mechanical properties LBL copolymers. Therefore, we investigated in synthetic conditions of grafting-through of $PDMS_{11}MA$ macromonomers to produce

difunctional P($PDMS_{11}MA$) macroinitiator brushes with high $n_{bb}\sim1000$, chain-end fidelity, and yield. Specifically, we explored the following synthetic parameters: (i) targeted DP of bottlebrush backbone, (ii) initial monomer concentration, (iii) solvent type, and (iv) ATRP techniques.

Grafting-through polymerization of $PDMS_{11}MA$ macromonomers was set up according to the procedure described in **Section 5.1**. Kinetic aliquots were taken at different timepoints to determine conversion by ^{1}H NMR. The extent of termination in a grafting-through polymerization was assessed by deviation from a linear trend by a reversible first-order kinetic equation. This equation accounts for the reversibility in a grafting-through polymerization as [M] approaches the equilibrium monomer concentration $[M]_e$ of $PDMS_{11}MA$. When a polymerization reaches $[M]_e$, the rate of propagation is equal to the rate of depropagation and polymerization stops[75-79]. $[M]_e$ in a grafting-through polymerization is solvent and temperature-dependent[80]. The $[M]_e$ was estimated by the dead-end monomer concentrations ($[M]_\infty$) of conventional radical polymerizations performed at $[M]_0$ = 100 – 400 mM[81,82]. In a typical experiment, 16 g (0.016 mol) of PDMS macromonomer was dissolved in 20 mL toluene in a 100 mL Schlenk flask charged with a stir bar, resulting in a 400 mM solution. 0.159 g AIBN (0.97 mM) was added and the solution was degassed for 1 hour under nitrogen. The flask was then immersed in a 50 ºC oil bath and samples were taken every 1, 2, 4, 6, 8 hours and then every 15 – 20 hours until the concentration of the monomer remained constant. This concentration was the equilibrium monomer concentration ($[M]_e$) (**Figure 5.12**). The conversion of the macromonomer was confirmed by 1H NMR. The above process was repeated for 200 mM and 100 mM initial monomer concentration as well as in *tert*-butylbenzene.

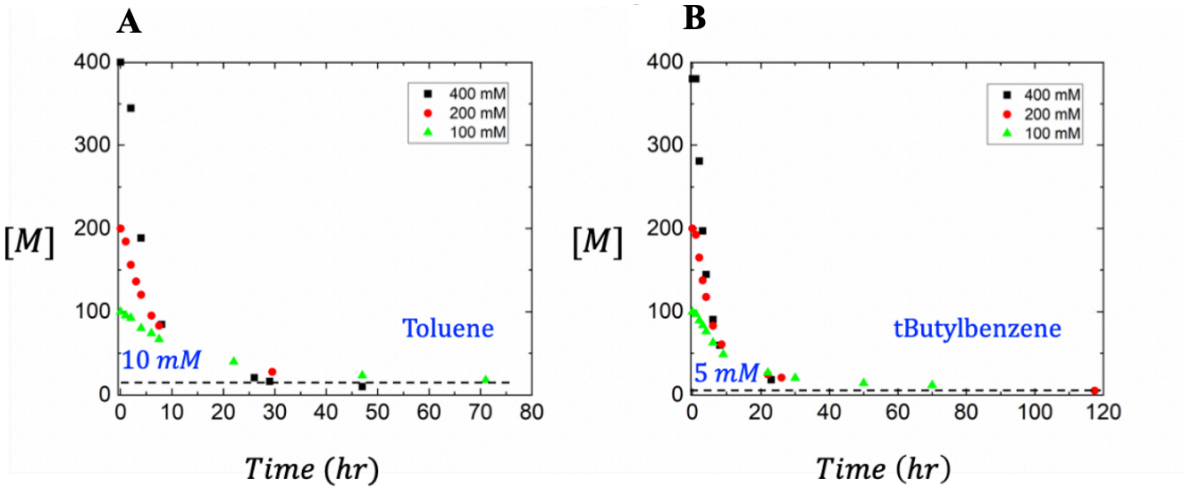

Figure 5.12: Equilibrium monomer concentration kinetic plot. Concentration versus time for free radical polymerization of PDMS macromonomer in **(A)** toluene and **(B)** *tert*-butylbenzene. $[M]_e$ in toluene was determined to be 10 mM and that in *tert*-butylbenzene was determined to be 5 mM.

A decrease in the slope $k_{p,\,app}$ can be attributed to a change in radical concentration. In a normal ATRP, a decrease in slope would correspond to an increase in $[CuBr_2]$ with radical termination according to the persistent radical effect[83]. All 10% decreases in $k_{p,\,app}$ are denoted and used to assess livingness in model polymerizations.

As shown in **Figure 5.13A**, a decrease in rate of polymerization was observed at lower conversion when targeting higher DP of the bottlebrush backbone. Polymerizations which targeted n_{bb}= 900, and 1200, exhibited a 10% decrease in apparent rate of polymerization ($k_{p,app}$) at 85 and 70 % conversion, respectively. Polymerization with a low targeted n_{bb} = 360 showed no noticeable decrease in $k_{p,app}$. Note that a higher targeted n_{bb} required a lower initiator and CuBr/Me_6TREN catalyst concentration. Control in a polymerization with only CuBr/Me_6TREN activator will rely on radical termination to generate $CuBr_2$/Me_6TREN deactivator, which can lead to a gradual improvement in polymerization control via faster

exchange reaction between active and dormant species but at the expense of the loss of chain end functionality and polymerization rate.

Next, the effect of initial monomer concentration was investigated (**Figure 5.13B**). For the same targeted $n_{bb} = 1200$, a significant decrease in polymerization rate occurred at lower conversions with a lower $[M]_0$. Specifically, 10% decreases in $k_{p,app}$ observed after reaching 70 and 60% conversion for polymerizations conducted at $[M]_0$ = 0.40 M and 0.25 M, respectively. From these studies, we concluded that high chain end functionality of P(PDMS$_{11}$MA) can be improved by polymerization at a high initial monomer concentration, targeting lower conversion. This agrees with general rules for controlled radical polymerization[84].

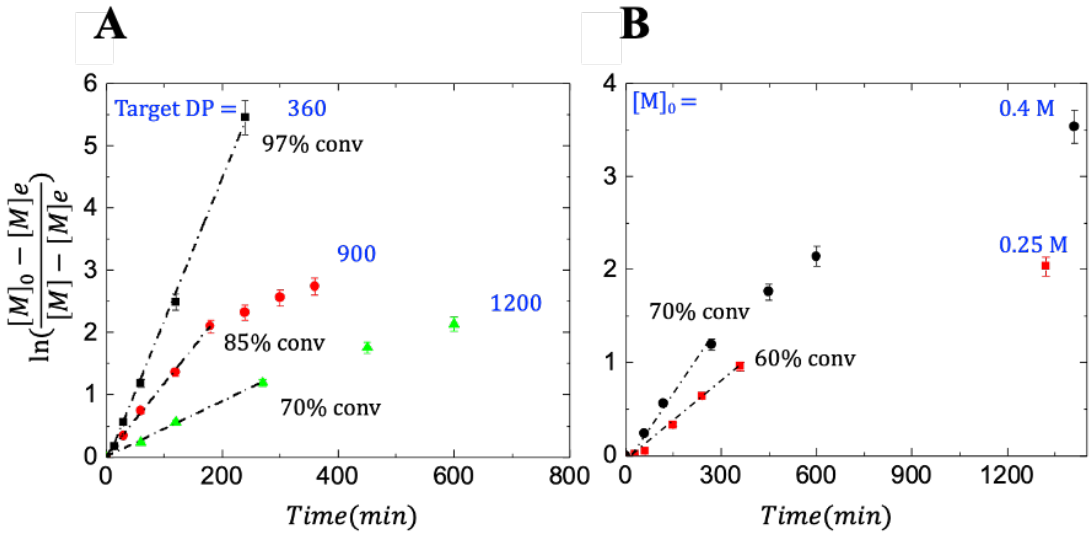

Figure 5.13: Effect of target n_{bb} and initial monomer concentration on kinetics of grafting-through polymerization of PDMS$_{11}$MA macromonomer. (A) Effect of target n_{bb} on kinetics of grafting through of PDMS$_{11}$MA macromonomer. The initial concentration was 0.4M. As target DP increased, termination started occur at lower % conversion. **(B)** Effect of initial monomer concentration on kinetics of grafting through of PDMS$_{11}$MA macromonomer. The target n_{bb} was kept at 1200. As initial monomer concentration decreased, termination started to occur at lower % conversion. $[M]_e$ in toluene = 10 mM.

To verify the effect of chain-end fidelity on plastomer mechanical properties, we synthesized three batches of P(PDMS$_{11}$MA) with the *same* final DP of $n_{bb} = 850 \pm 10$, calculated as conversion×targeted n_{bb}. All three batches were synthesized using 0.4 M initial monomer concentration. Batch 1 had targeted $n_{bb} = 1075$, and the reaction was quenched at 80% conversion. Targeted backbone DP for Batch 2 was 1200 and the reaction was quenched at 70% conversion. Finally, Batch 3 had targeted $n_{bb} = 1600$, and the reaction was quenched at 53% conversion. Using 3 different P(PDMS$_{11}$MA) macroinitiators, series of PBzMA-*b*-P(PDMS$_{11}$MA)-*b*-PBzMA triblocks with various n_L were synthesized. Films of each plastomer were prepared by slow solvent evaporation and followed by tensile stress measurements. The measurement was performed three times for each sample. The complete set of stress strain curves of the three batches of plastomers as well as their corresponding mechanical parameters were included in **Figure 5.14** and **Table 5.8 – 5.10**. The mechanical parameters, Young's modulus E_0 and firmness β, were obtained using the equation described in **Section 2.2**.

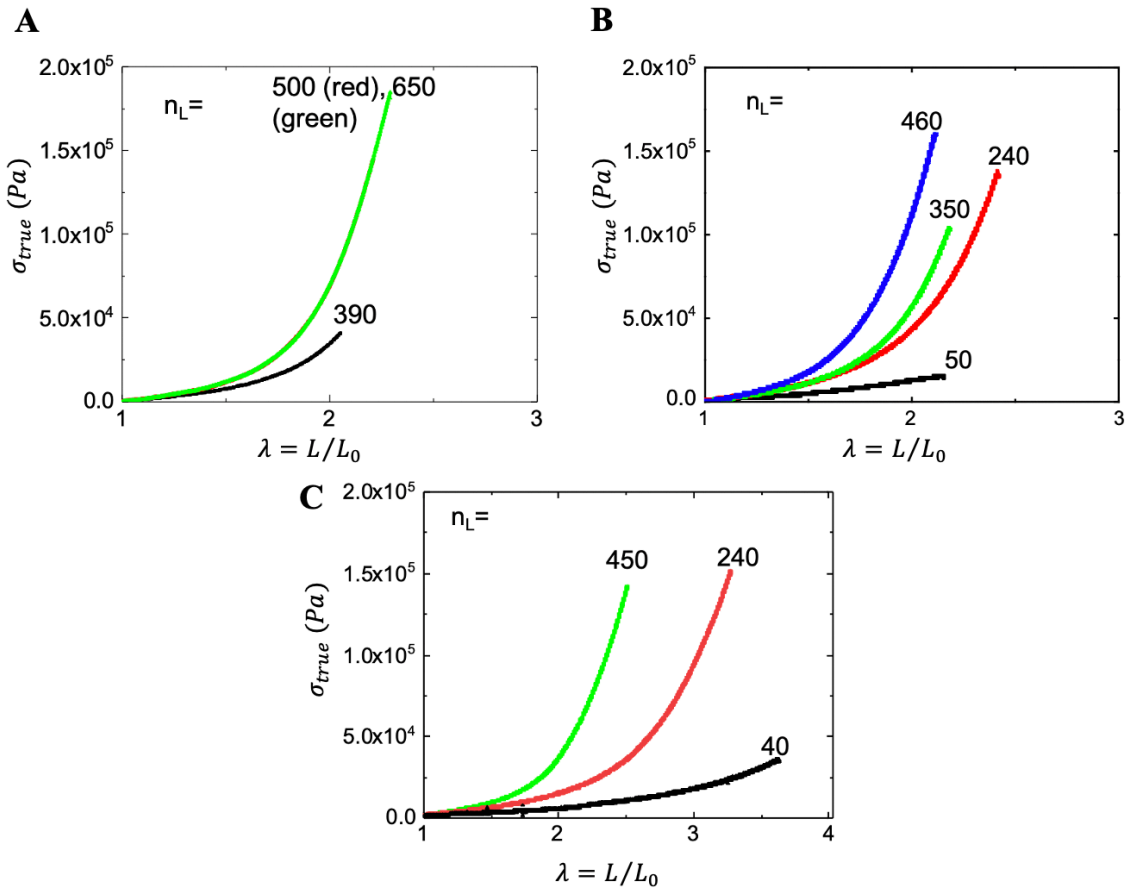

Figure 5.14: The strain-elongation response of three batches of PBzMA-*b*-P(PDMS$_{11}$MA)-*b*-PBzMA triblocks. (A) The stress-elongation responses of batch 1 PBzMA-*b*-P(PDMS$_{11}$MA)-*b*-PBzMA plastomers. n_{bb}= 860, n_L= 390, 500, 650. **(B)** The stress-elongation responses of batch 2 PBzMA-*b*-P(PDMS$_{11}$MA)-*b*-PBzMA plastomers. n_{bb}= 850, n_L= 50, 240, 350, 460. **(C)** The stress-elongation responses of batch 3 PBzMA-*b*-P(PDMS$_{11}$MA)-*b*-PBzMA plastomers. n_{bb}= 850, n_L= 40, 240, 450.

Table 5.8: Mechanical properties of batch 1 PBzMA-b-P(PDMSMA)-b-PBzMA plastomers

n_{bb}	n_L	β	E_0 (kPa)
860	390	0.38±0.03	11.3±0.52
860	500	0.46±0.02	15.5±1.7
860	650	0.44±0.03	16.7±1.0

Table 5.9: Mechanical properties of batch 2 PBzMA-b-P(PDMSMA)-b-PBzMA plastomers

n_{bb}	n_L	β	E_0 (kPa)
850	50	0.22±0.01	7.5±0.3
850	240	0.34±0.01	16.8±0.4
850	350	0.42±0.01	16.6±0.25
850	460	0.50±0.01	22.5±0.1

Table 5.10: Mechanical properties of batch 3 PBzMA-b-P(PDMSMA)-b-PBzMA plastomers

n_{bb}	n_L	β	E_0 (kPa)
850	40	0.08±0.002	4.5±0.1
850	240	0.19±0.01	9.9±0.3
850	450	0.35±0.02	14.2±0.9

Figure 5.15A shows example stress-strain curves of LBL triblocks with the same n_{bb}, n_L, and n_{sc} using P(PDMS$_{11}$MA) macroinitiators from batch 1, 2, and 3. Despite similar composition, plastomers assembled from these three triblocks exhibited different mechanical properties. By plotting E_0 vs. β, we compared the mechanical properties of three series of plastomers synthesized from different batches (**Figure 5.15B**). Each series consisted of 3-4 plastomers with different n_L. The slope of batch 1 was approximately the same as batch 2, but the positions of batch 2 plastomers were above batch 1. **Figure 5.15B** suggests that plastomers synthesized using batch 2 macroinitiators are stiffer compared to batch 1 plastomers. This observation corroborated our hypothesis as reactions quenched at lower conversions (batch 2) lead to bottlebrushes with higher chain-end fidelity and less

unfunctional BB impurities. However, a drop in modulus and firmness was observed when the targeted n_{bb} was highest with batch 3. However, a drop in modulus and firmness was observed when the targeted nbb was highest with batch 3. Batch 3 had the highest [M] relative to [2-BiB], which could lead to a lower [$Cu^{(II)}Br_2$] concentration and poor deactivation. This suggests the need to balance yield (batch 1) and [$Cu^{(II)}Br_2$] concentration (batch 3) to improve chain end fidelity and achieve optimal reaction conditions (batch 2) which are consistent with conventional ATRP kinetics.

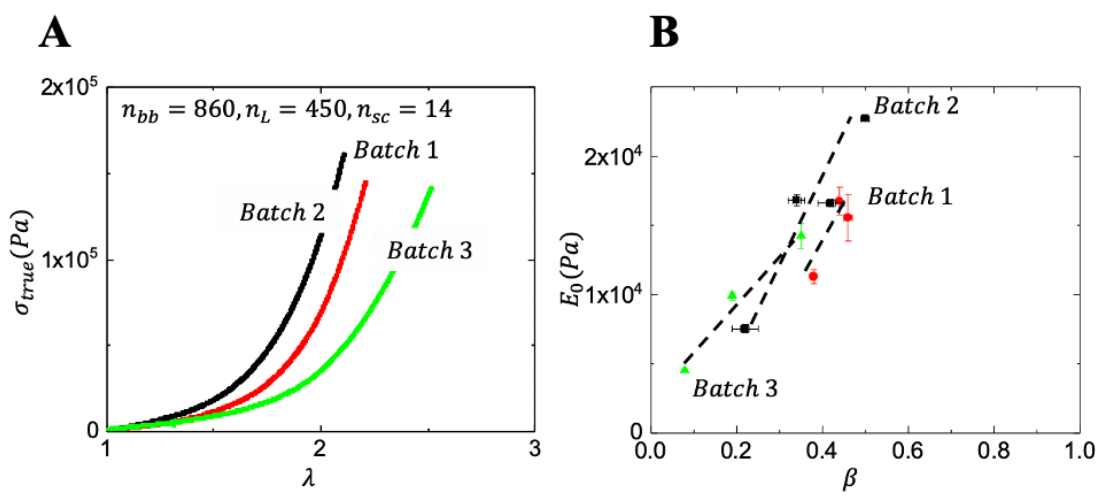

Figure 5.15: Comparison of mechanical properties of three batches of PBzMA-*b*-P(PDMS$_{11}$MA)-*b*-PBzMA triblocks. (A) Stress-strain curves of plastomers assembed from triblocks with the same architectural parameters ($n_{bb} = 860, n_L = 450, n_{sc} = 14$) but synthesized using different batches of P(PDMS$_{11}$MA) macroinitiators. **(B)** Young's modulus (E_0) vs. firmness parameter (β) for three series of plastomers that were synthesized using the same P(PDMS$_{11}$MA) macroinitiator from three different batches. Batch 1: Targeted n_{bb} = 1075, % conversion = 80%; Batch 2: Targeted n_{bb} = 1200, % conversion = 70%; Batch 3: Targeted n_{bb} = 1600, % conversion = 53%.

The above experiments confirmed that lower chain-end fidelity of the bottlebrush macroinitiator affects the mechanical properties of plastomers. A primary cause of chain-end fidelity loss during radical polymerization could be radical termination or chain transfer of a growing polymer to monomer or to solvent. Generally, ATRP proceeds faster in polar solvents due to improved solubility of catalysts and an increase in K_{ATRP}[85]. In the case of the $PDMS_{11}MA$ macromonomer, polar solvent selection is limited because the nonpolar PDMS sidechain has a particularly low Hildebrand solubility parameter of $\delta = 7.3 cal^{1/2} cm^{-3/2}$[86]. An ideal solvent for the grafting-through polymerization of $PDMS_{11}MA$ would have a large difference in Hansen solubility parameter to limit thermodynamic barriers (increase yield) while also having a low transfer coefficient[79]. Transfer of a H-atom from solvent to growing polymer radical can become important at high monomer conversion where rate of propagation is low due to a low [M], while the concentration of growing radical polymer chain ([P*]) and H-atom capped solvent ([S-H]) remain high. This can slow a polymerization if the solvent derived dormant species (for example benzyl bromide formed from toluene) is much less ATRP active (has ca. 2 orders of magnitude lower k_{act}) than the dormant $P(PDMS_{11}MA)$-Br polymer chain[87-89].

tert-Butylbenzene and chlorobenzene were assessed as solvents for $PDMS_{11}MA$ polymerization due to their anticipated lower transfer coefficients collected from literature (**Table 5.11**). Both solvents have similar solubility profiles to toluene but lack functional groups with readily extractable benzylic protons. Polymerization of $PDMS_{11}MA$ in tetrahydrofuran (THF) exhibited an earlier decrease in $k_{p,app}$ relative to toluene and was not investigated further (**Figure 5.16**).

Table 5.11: Transfer coefficients for polymerization of methyl methacrylate[a]

Material	Cs (x 10^4)	Temperature (°C)
Toluene	0.200	60
Xylene	0.43	60
1,4- Dioxane	0.222	80
THF[b]	0.5	60
Chlorobenzene	0.074	60

[a] $Cs = \frac{k_{tr}}{k_p}$. All values collected from the Polymer Handbook, 4th Ed. [b]C_s is given for a styrene polymerization in THF conducted at 60 °C.

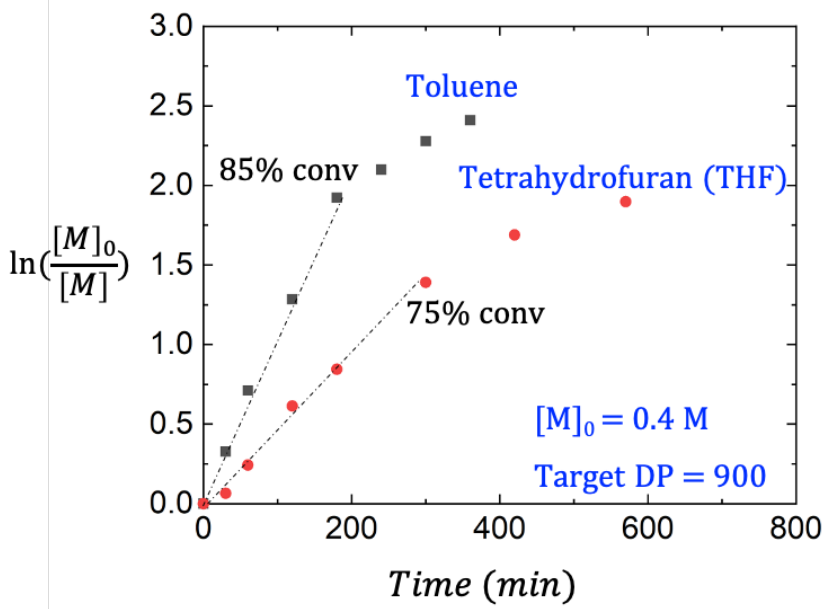

Figure 5.16: Comparison of reaction kinetics in toluene and THF. Both reactions were run at 45 °C, and the initial monomer concentration was 0.4 M. The targeted DP of the bottlebrush backbone was $n_{bb} = 900$, and [I]:[$Cu^{(I)}$]:[Me_6TREN] = 1:2:2. For the reactions that occurred in toluene, termination occurred after the conversion reached 85%, while termination started to occur at 75% conversion for the reaction in THF.

Polymerizations were run in three different solvents (toluene, *tert*-butylbenzene, and chlorobenzene) under the same $[M]_0$=0.4M, targeted $n_{bb} = 1200$, and [I]:[$Cu^{(I)}Br$]:[Me_6TREN] = 1:2:2 ([I] was calculated as the mole of 2-BiB divided by the volume of the reaction volume). Comparison of the reversible first order kinetic plots shows that reactions in *tert*-butylbenzene and chlorobenzene proceeded to > 90% conversion before a significant decrease in $k_{p,app}$ was observed, while polymerization in toluene gradually slowed after reaching 70% conversion, (**Figure 5.17**). This systematic study suggested that solvent choice is important in maintaining the chain end functionality of P($PDMS_{11}MA$) bottlebrushes. Using solvents such as *tert*-butylbenzene and chlorobenzene, we were able to avoid formation of solvent derived dormant species which would slow polymerization as well as maintaining an efficient rate of ATRP. Hence, this modification in solvents provided a more reliable method of synthesizing P($PDMS_{11}MA$) bottlebrushes with high chain end fidelity.

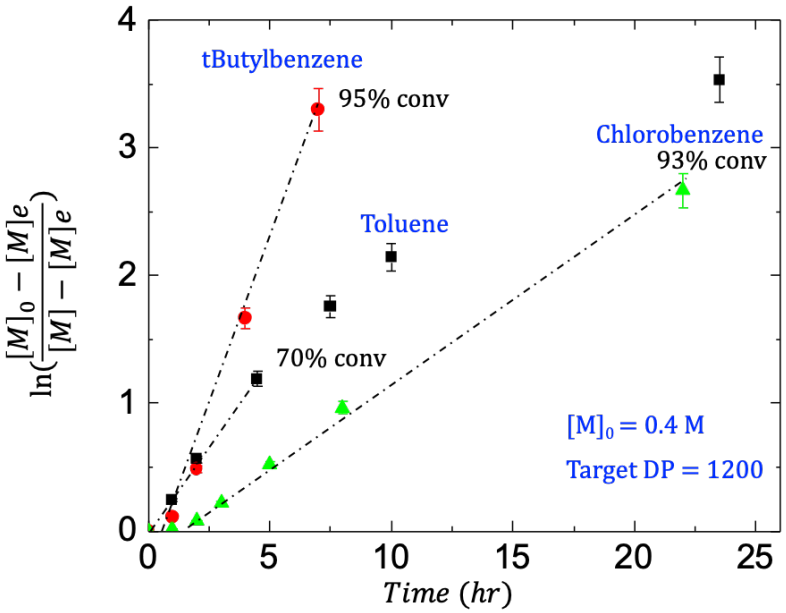

Figure 5.17: Comparison of reaction kinetics in different solvents. All reactions were run at 45 ºC, and the initial monomer concentration was 0.4 M. The targeted DP of the bottlebrush backbone was $n_{bb} = 1200$, and [I]:[$Cu^{(I)}$]:[Me_6TREN] = 1:2:2. For the reactions that occurred in *tert*-butylbenzene and chlorobenzene, termination occurred after the conversion reached 90%, while termination started to occur at 80% conversion for the reaction in toluene. $[M]_e$ in toluene = 10 mM. $[M]_e$ in *tert*-butylbenzene = 5 mM

Another approach to decrease the probability of chain breaking reactions during grafting-through polymerization of $PDMS_{11}MA$ macromonomers is to improve catalytic systems. To extend the livingness of controlled radical polymerization as well as decrease the amount of catalysts used, several alternatives to the traditional ATRP methods such as activators regenerated by electron transfer (ARGET) ATRP, initiators for continuous activator regeneration (ICAR) ATRP, eATRP, photoinduced ATRP were recently developed[90]. In our study, we selected supplemental activator and reducing agent (SARA) ATRP technique[91]. SARA ATRP is a subset of ARGET ATRP, where $Cu^{(0)}$ is used as a reducing agent, but it can also serve as a supplemental activator for halogen terminated initiators and polymer chain-ends. $Cu^{(0)}$ can comproportionate with $Cu^{(II)}$ to produce two equivalences of $Cu^{(I)}$ while in the

reverse process, two equivalents of $Cu^{(I)}$ disproportionate into one equivalent of Cu(0) and one equivalent of $Cu^{(II)}$ (**Figure 5.18**)[92]. The benefits of using SARA ATRP include a lower catalyst loading, a higher concentration of deactivating $Cu^{(II)}$ species, and lower sensitivity to oxygen.

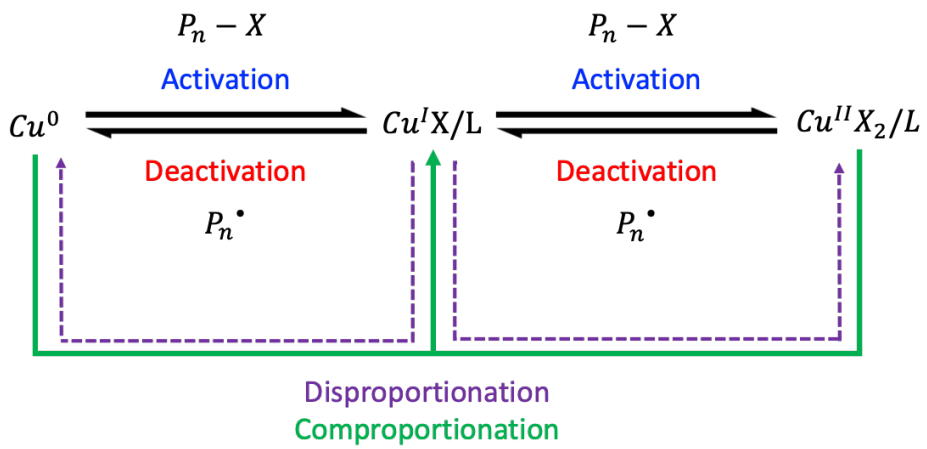

Figure 5.18: Mechanism of SARA ATRP.

In this study, copper wire with 1 mm diameter was used as the source of $Cu^{(0)}$, initial $PDMS_{11}MA$ macromonomer concentration was 0.40 M, and [I]:[$Cu^{(II)}Br_2$]:[Me_6TREN] = 1:0.1:2. In order for the reaction to proceed more efficiently, solvent effects should also be taken into account. One of the factors that affects the rate of SARA ATRP is the rate at which $Cu^{(I)}$ is extracted from the surface of $Cu^{(0)}$ and dissolved in solution[93]. Here, tetrahydrofuran (THF) was investigated in SARA ATRP in comparison to toluene used in traditional ATRP. The targeted backbone DP for both experiments was n_{bb}=1200. As seen in **Figure 5.19**, termination took place after 70% conversion for the reaction using normal ATRP. However, SARA ATRP was able to achieve 92% conversion, at which the reaction was quenched, before the rate decrease started to occur. There was also an induction period of > 5 hours in the kinetic

plot in SARA ATRP. Note that although $Cu^{(0)}$ itself can act as an activator, the activating efficiency is significantly lower than that of $Cu^{(I)}$ [91]. Furthermore, as shown in **Figure 5.19**, the reactions in SARA ATRP were 3-fold slower compared to the traditional ATRP method. This was expected due to the induction period as well as more $Cu^{(II)}$ in the system causing the deactivation rate to be faster, hence the overall rate of ATRP was slower and accompanied by less termination[94].

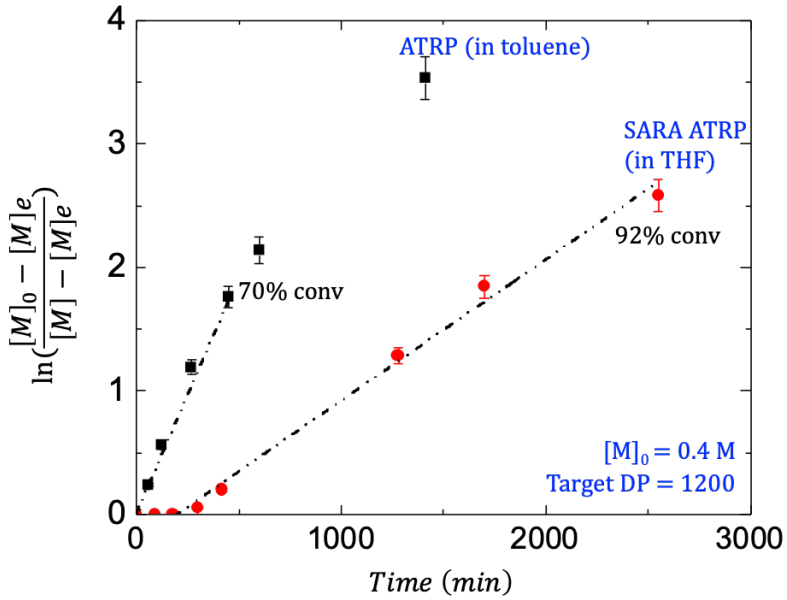

Figure 5.19: Comparison between traditional ATRP and SARA ATRP. Targeted $n_{bb} = 1200$, $[Cu^{(0)}] = 0.08$ cm²/mL, $[Cu^{(II)}] = 10$ mol%, $[Cu^{(II)}Br_2]$:$[Me_6TREN]$ = 1:20. Initial monomer concentration was 0.4 M for both reactions, temperature was set to 45 ºC. In toluene, $[M]_e$=10 mM.

5.4 Closing remarks

In this chapter, we demonstrated that the unique tissue-mimetic plastomer platform is sensitive to synthetic impurities caused by loss of chain end functionality during macromonomer polymerization, which elucidates observed discrepancies in the mechanical properties of plastomers with similar architecture targets. Grafting-through polymerization of PDMSMA is challenging due to the limited selection of solvents which are not prone to

chain breaking reactions and a slow rate of propagation which is in competition with depropagation[95]. We were able to provide synthetic insights to overcome the challenges to prepare difunctional P($PDMS_{11}MA$) macroinitiators with high chain end fidelity.

In particular, we performed kinetic studies of grafting-through polymerization of a $PDMS_{11}MA$ macromonomer under systematically different conditions. Kinetic studies showed that chain breaking reactions can become significant in polymerizations conducted at low initial monomer concentrations in solvents with high transfer coefficients. Increasing macromonomer concentration, targeting higher polymerization DP, and stopping polymerization at lower conversion decreased the extent of terminated chains. Polymerization in *tert*-butylbenzene and chlorobenzene had better polymerization control due to a decreased rate of chain transfer reactions compared to toluene. Additionally, SARA ATRP was successful in synthesizing P($PDMS_{11}MA$) with high targeted backbone DP and chain-end fidelity. In conclusion, the best synthetic conditions to minimize LB and B impurities were as follows: 1) $[M]_o > 0.4$ M; 2) solvents without moieties to undergo chain transfer reactions, such as *tert*-butylbenzene and chlorobenzene; and 3) methods which produce a higher fraction $CuBr_2$/L deactivating catalyst without relying on RT, such as SARA ATRP.

Additionally, we developed a novel method to qualitatively assess loss of chain end functionality in macromonomer polymerization by the mechanical properties of final LBL triblocks. All of these efforts will facilitate future LBL triblock design to achieve robust and consistent mechanical properties.

CHAPTER 6

Controlling the Mechanical Properties of Plastomers

6.1 Effect of n_L on stress-elongation responses of plastomers

The mechanical properties of plastomers are controlled by the architectural encoding of the linear-bottle-linear (LBL) triblock copolymer. As discussed in **Section 4.2**, various architectural and chemical parameters can be decided and tuned at the synthetic level, including degrees of polymerization (DP) of linear blocks (n_L), bottlebrush blocks (n_{bb}), and bottlebrush side chains (n_{sc})[26]. To investigate the effect of individual parameter on the mechanical properties of plastomers, we synthesized a series of PBzMA-*b*-P(PDMS$_{11}$MA)-*b*-PBzMA LBL triblocks with the same n_{bb} and n_{sc} but differed in n_L. **Figure 6.1** showed the stress-elongation curves of the series and the fitting results were shown in **Table 6.1**. As mentioned previously, the chemically and architecturally linear and bottlebrush components microphase separate into physical networks, with linear domains distributed in the soft bottlebrush matrix[58-60]. The diameter of the linear domain R is proportional to n_L. Hence, plastomers with higher n_L will form larger spherical domains. Larger domain has higher curvature, causing the bottlebrush to be more pre-strained, which in turn increases the firmness of the plastomer. Furthermore, higher n_L also increases the entanglement in the linear domain, which causes the modulus of the plastomers to increase.

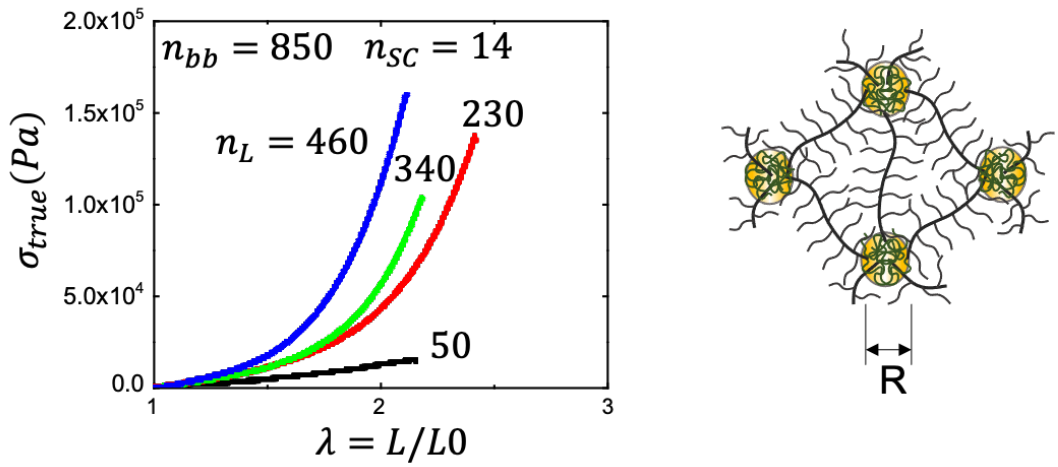

Figure 6.1: Stress-elongation response of PBzMA-*b*-P(PDMS$_{11}$MA)-*b*-PBzMA triblock copolymers with varied n_L.

Table 6.1: **Fitting results of PBzMA-*b*-P(PDMS$_{11}$MA)-*b*-PBzMA with varied n_L**

n_L	E (kPa)	E_0 (kPa)	β	R
50	5.3	7.5	0.22	
230	9.0	16.8	0.34	
340	7.2	16.6	0.42	
460	7.5	22.5	0.50	

6.2 Effect of n_{bb} on stress-elongation responses of plastomers

Interested in the effect of n_{bb}, a different series of PBzMA-*b*-P(PDMS$_{11}$MA)-*b*-PBzMA triblocks were synthesized where the volume fraction of the linear block ϕ_L (calculated as $V_L/(V_L + V_{bb})$, where V_L was the total volume of the linear blocks and V_{bb} was the volume of the bottlebrush block) and the n_{sc} were held constant and n_{bb} was varied. **Figure 6.2** showed

the stress-elongation curves of the series and the fitting results were shown in **Table 6.2**. As n_{bb} increased, the bottlebrush backbone is less strained, causing β and modulus to decrease.

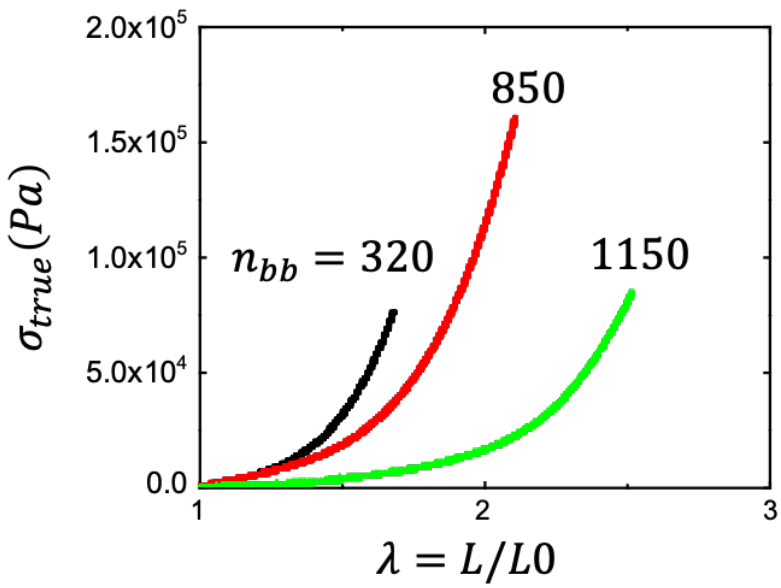

Figure 6.2: Stress-elongation responses of PBzMA-*b*-P(PDMS$_{11}$MA)-*b*-PBzMA triblock copolymers with varied n_{bb}. n_{sc} = 14, ϕ ~ 0.12.

Table 6.2: **Fitting results of PBzMA-*b*-P(PDMS$_{11}$MA)-*b*-PBzMA with varied n_{bb}**

n_{bb}	n_L	ϕ_L	E (kPa)	E_0 (kPa)	β
320	150	0.12	5.6	19.6	0.54
850	460	0.13	7.5	22.7	0.50
1150	470	0.11	3.7	6.9	0.33

6.3 Decoupling firmness and modulus

Noticeably, the above data showed that firmness and modulus increased concurrently. Interested in whether it was possible to decouple firmness and modulus and control each

parameter separately, we conducted a series of mixing experiments. PMMA-*b*-P(PDMS$_{11}$MA) diblock was synthesized and mixed with PMMA-*b*-P(PDMS$_{11}$MA)-*b*-PMMA triblocks. The two components had the same ϕ_L.The effect of the weight percentage (wt%) of the diblock was shown in **Figure 6.3**, which demonstrated that increase in wt% of diblock mixture would decrease the modulus, but the modulus was not affected. Since the diblock only had one end of linear chain, it created dangling ends upon microphase separation, triggering the decrease in modulus.

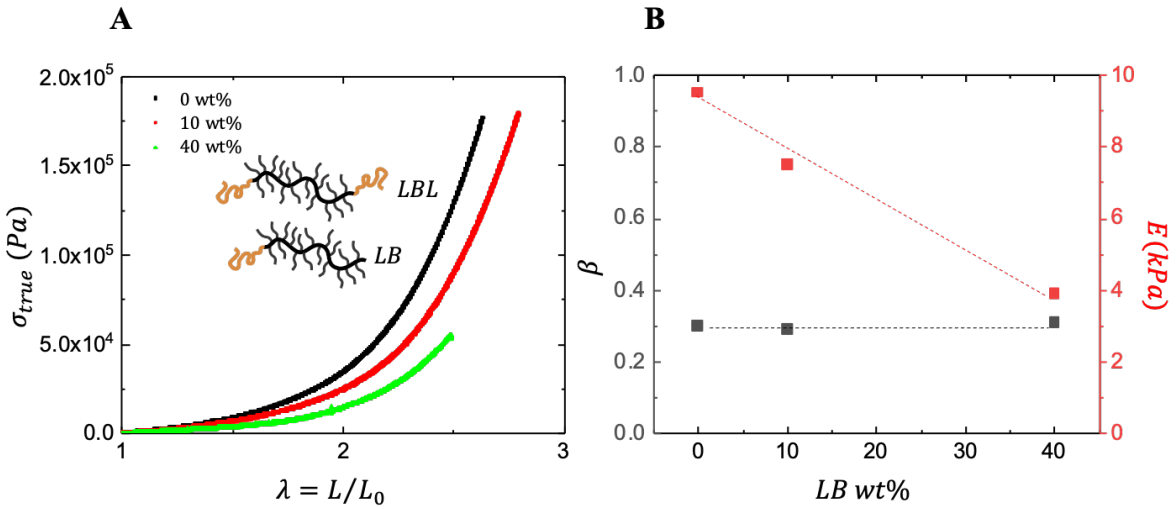

Figure 6.3: Adding linear-bottlebrush (LB) deblocks decreased modulus of the linear-bottlebrush-linear (LBL) triblocks. (A) The stress-elongation response change upon adding 10. wt%, 40. wt% of linear-bottlebrush PMMA$_{170}$-*b*-P(PDMS$_{11}$MA)$_{440}$ diblocks to PMMA$_{360}$-*b*-P(PDMS$_{11}$MA)$_{940}$-*b*-PMMA$_{360}$ plastomers. $n_{sc} = 14$ for both polymers. **(B)** Effect of wt% of LB mixtures on the mechanical properties of LBL triblocks.

6.4 Mixing experiments of triblocks

Additionally, we conducted a series of mixing experiments between different triblocks. First, we mixed two triblocks with the same ϕ_L, n_{sc}, and chemical composition, but different

n_{bb} . The two triblocks, PBzMA$_{470}$-*b*-P(PDMS$_{11}$MA)$_{1150}$-*b*-PBzMA$_{470}$ and PBzMA$_{150}$-*b*-P(PDMS$_{11}$MA)$_{320}$-*b*-PBzMA$_{150}$, were co-dissolved in toluene in 50:50 weight ratio. The film was prepared by slowly evaporating the solvent. **Figure 6.4** and **Table 6.3** showed the mechanical behavior of the pure plastomers and the mixed plastomers. The Young's modulus and firmness of the mixture were between that of the two pure plastomers.

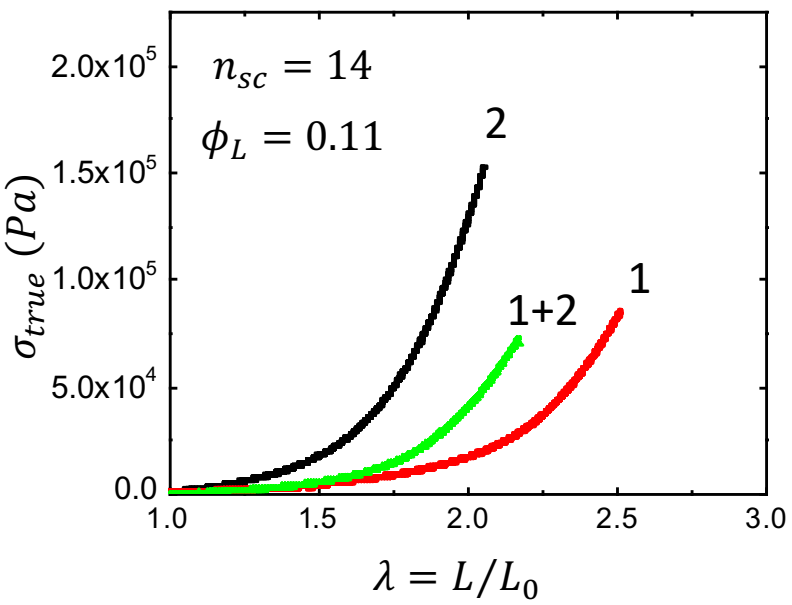

Figure 6.4: Strain-elongation responses of PBzMA-*b*-P(PDMS$_{11}$MA)-*b*-PBzMA triblock copolymer mixtures with varied n_{bb}. 1: PBzMA$_{470}$-*b*-P(PDMS$_{11}$MA)$_{1150}$-*b*-PBzMA$_{470}$ plastomers. 2: PBzMA$_{150}$-*b*-P(PDMS$_{11}$MA)$_{320}$-*b*-PBzMA$_{150}$ plastomers. The ϕ_L for both plastomers is 0.11. 1+2: Mixture of 1 and 2 in 50:50 weight ratio.

Table 6.3: Mechanical parameters of two PBzMA-*b*-P(PDMS$_{11}$MA)-*b*-PBzMA plastomers with different n_{bb} and their mixture (50:50 weight ratio).

Sample	n_{bb}	n_L	ϕ_L	E (kPa)	E_0 (kPa)	β
1	1150	470	0.11	3.7	6.9	0.33
1+2	-	-	-	2.7	7.8	0.48
2	320	150	0.12	5.6	19.6	0.54

Same conclusion could be made by mixing two triblocks with the same n_{bb}, n_{sc}, and chemical species, but different ϕ_L(**Figure 6.5**, **Table 6.4**). It was expected that the size of the linear domain of the mixture would be between that of the two pure plastomers, hence causing the Young's modulus and firmness to fall in between the two pure plastomers.

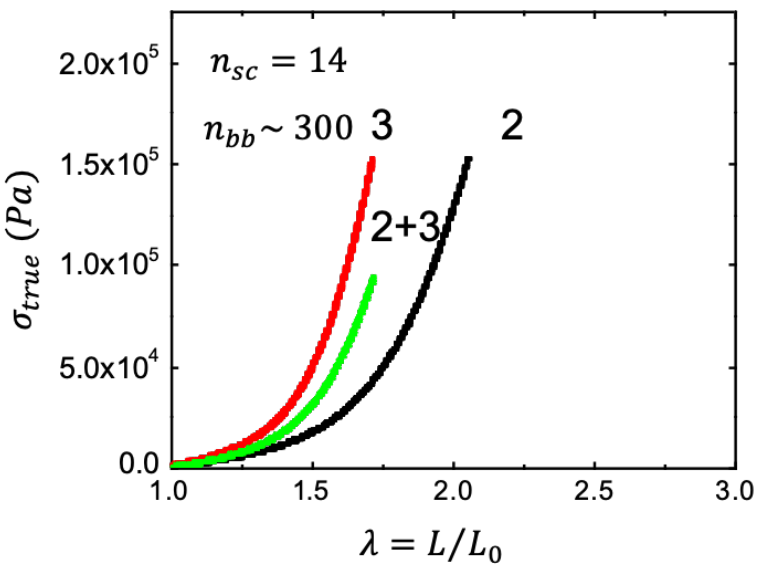

Figure 6.5: Strain-elongation responses of PBzMA-*b*-P(PDMS$_{11}$MA)-*b*-PBzMA triblock copolymer mixtures with varied ϕ_L. 2: PBzMA$_{150}$-*b*-P(PDMS$_{11}$MA)$_{320}$-*b*-PBzMA$_{150}$ plastomers. 3: PBzMA$_{260}$-*b*-P(PDMS$_{11}$MA)$_{320}$-*b*-PBzMA$_{260}$ plastomers. 2+3: Mixture of 2 and 3 in 50:50 weight ratio.

Table 6.4: Mechanical parameters of two PBzMA-*b*-P(PDMS$_{11}$MA)-*b*-PBzMA plastomers with different ϕ_L and their mixture (50:50 weight ratio).

Sample	n_{bb}	n_L	ϕ_L	E (kPa)	E_0 (kPa)	β
2	320	150	0.12	5.6	19.6	0.54
2+3	-	-	-	4.6	26.8	0.65
3	320	260	0.19	5.6	34.6	0.68

Finally, we performed a series of experiments using two triblocks with the chemical structure, n_{bb}, n_{sc}, but different n_L. The mixture was composed of different weight ratio of the two plastomers. **Figure 6.6 and Table 6.5** showed the mechanical behaviors of the mixtures. Overall, as we increased the percentage of the plastomer with higher n_L, both modulus and firmness increased. This corroborated with our observations when the mixture was in 50:50 ratio.

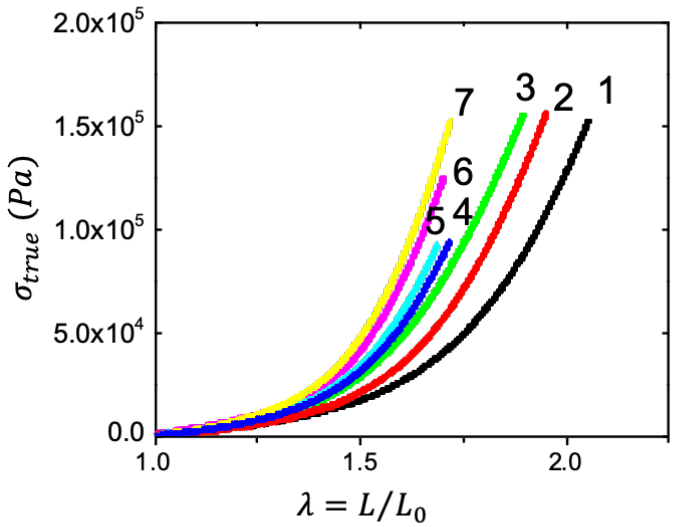

Figure 6.6: Strain-elongation responses of two PBzMA-*b*-P(PDMS$_{11}$MA)-*b*-PBzMA triblock copolymers mixed with varied weight ratios: 1: 100% PBzMA$_{150}$-*b*-P(PDMS$_{11}$MA)$_{320}$-*b*-PBzMA$_{150}$ plastomers. 7: 100% PBzMA$_{260}$-*b*-P(PDMS$_{11}$MA)$_{320}$-*b*-PBzMA$_{260}$ plastomers. 1:7 = 90:10 (2), 70:30 (3), 50:50 (4), 30:70 (5), 10:90 (6).

Table 6.5: Mechanical parameters of two PBzMA-*b*-P(PDMS$_{11}$MA)-*b*-PBzMA plastomers mixed with different weight ratios

No.	Ratio of 1:7	E (kPa)	E_0 (kPa)	β
1	100:0	5.6	19.6	0.54
2	90:10	5.3	22.0	0.58
3	70:30	5.6	26.4	0.61
4	50:50	4.6	26.8	0.65
5	30:70	5.2	28.3	0.64
6	10:90	5.5	31.8	0.65
7	0:100	5.1	34.6	0.68

6.5 Closing remarks

In conclusion, we uncovered means to control the mechanical properties of plastomers. Furthermore, we demonstrated methods to decouple modulus and firmness. Finally, by mixing triblock copolymers with various weight ratios, we discovered that the mixtures of plastomers covered a wide range of mechanical properties. Hence, in order to control the mechanical properties of plastomers, we can not only vary the architectural and chemical parameters of the triblocks, but also mix different plastomers so that we do not need to synthesize new materials. However, so far we only established qualitatives relationships between change in Young's modulus and firmness with respect to the ratio of mixtures. Further study can be done to discover the quantitative correlation.

CHAPTER 7

Machine Learning Assisted Strategic Synthesis Planning

7.1 Challenges in cost-efficient production of plastomers

The mechanical properties of plastomers can be precisely controlled by a series of chemical and architectural encoding: degree of polymerization (DP) of the bottlebrush backbone n_{bb}, DP of linear block n_L, side chain length n_{sc}, grafting density of the bottlebrush backbone n_g, Flory-Huggins interaction parameter χ, and average melting temperature of the bottlebrush and linear blocks T_g. These parameters can be controlled during synthesis, which is a two-step atomic transfer radical polymerization (ATRP): the grafting-through polymerization of macromonomers of choice followed by chain extension of the macroinitiator (**Chapter 5**). Using the protocol developed in **Chapter 5**, we have produced materials that mimicked tissues' high firmness and soft modulus. Plastomers produced in our group have provided some general trend in correlation between [n_{bb}, n_L, n_{sc}, n_g, χ, T_g] and [β, E_0]. For example, we demonstrated in **Section 6.1** and **Section 6.2** that higher n_{bb} and lower n_L lead to lower firmness and modulus and vice versa. However, we still yet to uncover the relative importance of these parameters in the mechanical properties of plastomers. Furthermore, we still need yet to establish a quantitative correlation between all six parameters and the mechanical properties of plastomers. Establishing such a relationship will allow strategic planning of the plastomer synthesis to target desired quantatitive values of

mechanical properties, which in turn saves cost in both time and raw materials. To solve this problem, we have decided to utilize statistical and machine learning modeling.

7.2 Introduction to machine learning

Machine learning is a subset of data analytic algorithms and modeling. The name comes from the fact that machines are able to process and model complex and high-dimensional datasets by going through training processes. It has proven to be powerful and effective in solving challenging problems in many different fields, such as finance, retail, technology, and healthcare. Starting from several years ago, machine learning has been applied in chemistry research, such as drug discovery, retrosynthesis of small organic molecules, reaction prediction, just to name a few[96-101]. Although machine learning has been used to predict material properties such as inorganic materials and metalloids[102-107], applications in prediction of soft materials' mechanic properties are still lacking. In this study, we utilized decision tree, random forest, gradient boosting, and deep neural network models which were trained using a dataset of previously synthesized triblocks to predict the firmness and modulus of plastomers. Decision tree breaks the dataset into smaller and smaller subsets, and distributes these subsets to different leaf nodes, until the subsets at a leaf node cannot be further broken down. Since there are many possible schemes to branch out from a root, a branching scheme that results in the lowest standard deviation in each branch is selected[108-110]. As its name suggests, random forest is an ensemble of decision trees. The dataset is broken into multiple subsets randomly and each subset is distributed to a decision tree and the results from each tree are averaged to produce the final prediction[111,112]. Similar to random forest, gradient boosting also consists of multiple decision trees. However, the

algorithm focuses on improving the performance of the worst decision tree[113-115]. Last but not the least, neural network is inspired by the neuron network in human brain. Neural network contains multiple nodes divided into three types of layers: input layer, hidden layer, and output layer[116,117]. All nodes are interconnected, analogous to the neurons in human brains. The input layer refers to the dataset that gets passed to a hidden layer, or multiple hidden layers. The output layer can consist of multiple nodes, depending on the number of outputs. In this study, it consists of two nodes, since the model is predicting numerical results for firmness and modulus. Neural network uses a user-specified loss function, which computes the difference between predicted values from the output layer and actual values. The goal is to minimize the loss after numerous iterations.

7.3 Motivation and rationale

Previously, we reported on linear-block-linear triblock copolymers that microphase separated into linear domains distributed in bottlebrush matrix (**Figure 7.1A**) and have demonstrated their resemblance to biological tissues[58]. Remarkably, the advantage of using the triblock approach was the ability to encode the mechanical properties into the material assembled from one single molecule without the need for composites or cross-linkers. Interested in the mechanical performance all of the plastomers we have produced, we plotted plastomers and tissues on the Young's modulus (E_0) vs. firmness (β) map (**Figure 7.1B**). The plastomers shown in **Figure 7.1B** differed in degree of polymerization (DP) of the bottlebrush backbone n_{bb}, DP of linear block n_L, side chain length n_{sc}, grafting density of the bottlebrush backbone n_g, Flory-Huggins interaction parameter χ, and average melting temperature of the bottlebrush and linear blocks T_g. Noticeably, the mechanical properties of

plastomers overlapped with those of tissues in the left region of the graph, which had firmness below 0.8 and modulus between 10^4 - 10^5 Pa. However, a gap still existed in the high firmness (> 0.8) and high modulus region (> 10^5 Pa).

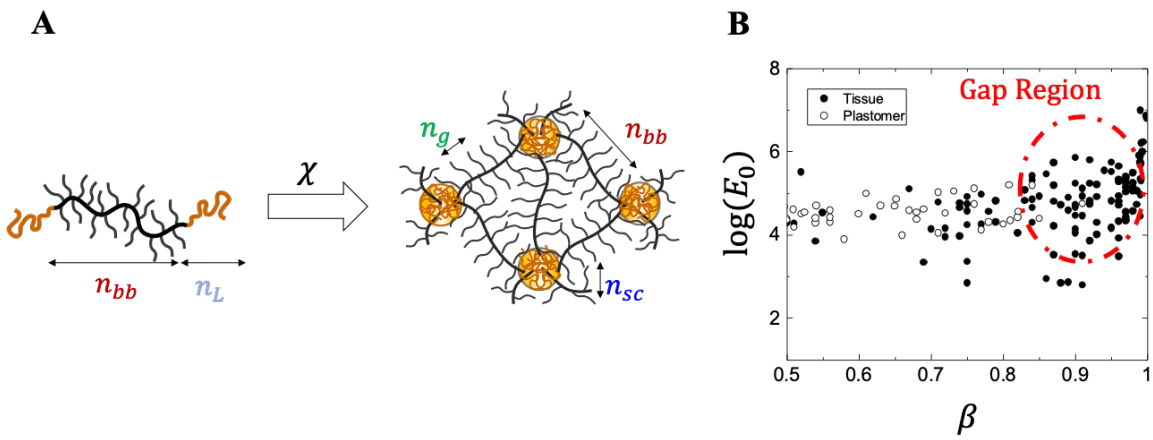

Figure 7.1: Mechanical property gap between synthetic plastomers and tissues. **(A)** Linear-bottlebrush-linear (LBL) triblock copolymer microphase-separate into linear domains distributed in bottlebrush matrix, forming plastomers. n_{bb}: Degree of polymerization (DP) of the bottlebrush backbone; n_L: DP of linear block; n_{sc}: Side chain length; n_g: grafting density of the bottlebrush backbone; χ: Flory-Huggins interaction parameter. **(B)** Comparison between the mechanical properties of soft biological tissues and synthetic plastomers.

To bridge the gap between plastomers and tissues, plastomers with high firmness and modulus need to be synthesized. However, due to the large number of tunable parameters involved, it was difficult to select the correct combination to result in a plastomer with targeted mechanical properties. Although previously, we have established understanding of qualitative and physical effects of n_{bb}, n_L, and n_{sc} on firmness and modulus of the plastomers[70], we still lacked a quantitative model that correlates all synthetic parameters with the resulting mechanical properties. Previously, the triblock copolymers were synthesized based on a trial-and-error process: a polymer was synthesized and then prepared for

mechanical property measurement. If the result of the measurement did not satisfy the targeted firmness and modulus, the entire process was repeated after tweaking synthetic parameters until the desired mechanical properties were obtained. Establishing a model that accurately predicts the firmness and modulus mechanical parameters of plastomers based on chemical and architectural parameters saves both cost and time.

7.4 Data preparation

A collection of plastomers was established, using previously synthesized and characterized materials (**APPENDIX 2**). The collection consisted of a wide range of architectural parameters as well as a variety of chemical compositions. In particular, the features being considered were degree of polymerization (DP) of the bottlebrush backbone n_{bb}, DP of linear block n_L, side chain length n_{sc}, grafting density of the bottlebrush backbone n_g, Flory-Huggins interaction parameter χ, and average melting temperature of the bottlebrush and linear blocks T_g. Four models were used: decision tree, random forest, gradient boosting, and neural networks. Prior to being fed into the model, the plastomer dataset was first standardized so that all values were in the range of (0,1). This scaling stabilized the variance of the variables, standardized the variables to have the same range so that their contribution could be compared, and accelerated the convergence during the training phase of the neural network. The dataset was divided into training set and test set. The training set was used to tune the parameters of the models while the test set was used to evaluate the prediction performance and generalizability of the models. Mean absolute error, computed as the average between absolute error of firmness and modulus, and percent error,

computed as the difference between predicted and actual value divided by the actual value, were used as the metrics for prediction accuracy.

7.5 Multiple Linear Regression

A multiple linear regression model (MLR) was used as the baseline model, since it's a simpler model than the ones introduced in **Section 7.2**. It assumed that the firmness β and Young's modulus E_0 are linear combinations of [n_{bb}, n_L, n_{sc}, χ, T_g] (equation 3, 4).

$$\beta = c_0 + c_1 n_{bb} + c_2 n_L + c_3 n_{sc} + c_5 T_g \quad (3)$$

$$E_0 = c_0 + c_1 n_{bb} + c_2 n_L + c_3 n_{sc} + c_4 \chi + c_5 T_g \quad (4)$$

Table 7.1 displayed the fitting results for the MLR model of firmness. As shown by the estimates of the coefficients, firmness decreased with increasing n_{bb} and T_g and increased with increasing the other three parameters. This observation was in accordance with our previous conclusions from mechanical testing (**Section 6.2**). The R^2 value was 0.676, implying that the fitting performance was moderate but not exceptional. The p-values of the coefficients for χ and T_g were both larger than 0.1, indicating that these two parameters might not be significant in deciding the value of β. Therefore, we used forward selection to select the combination of parameters to include in the model that minimized the Akaike information criteria (AIC). **Table 7.2** showed the fitting result using forward selection. The Flory-Huggins interaction parameter χ was not included in the new model. The p-values were all less than 0.1, indicating that all parameters were significant. The R^2 value of the new model was 0.671, which was relatively similar to the model that included all parameters.

Therefore, excluding χ did not compromise the fitting performance. Judging by the absolute values of the coefficients in **Table 7.2**, n_{sc} contributed most significantly to β, followed closely by n_L. T_g contributed negatively to β and had the smallest effect.

Table 7.1: Fitting results summary of the multiple linear regression model of firmness $\boldsymbol{\beta}$.

Coefficient	Estimate	Std. Error	P-value
c_0	0.30	3.9E-2	3.25E-11
c_1	-1.58E-4	4.2E-5	3.7E-4
c_2	3.02E-4	5.5E-5	4.9E-7
c_3	5.8E-3	6.9E-4	1.5E-12
c_4	4.3E-3	3.8E-3	0.27
c_5	-1.67E-3	1.19E-3	0.17

Table 7.2: Fitting results summary of the multiple linear regression model of firmness $\boldsymbol{\beta}$ fitted with forward selection.

Coefficient	Estimate	Std. Error	P-value
c_0	0.56	0.036	1.26E-5
c_1	-0.32	0.085	3.0E-4
c_2	0.45	0.080	3.0E-7
c_3	0.44	0.053	2.0E-12
c_5	-0.27	0.15	0.084

The same forward selection process was used to fit Young's modulus E_0. To stabilize the variance, we fitted the standardized logarithmic E_0. **Table 7.3** displayed the fitting results of logarithmic E_0. In this case, the forward selection kept three predictors, n_{bb}, n_L, and χ. The p-values for all coefficients were smaller than 0.1, indicating that all three predictors were significant in affecting the Young's modulus. The coefficient for n_{bb} was negative, indicating that increasing n_{bb} decreased modulus, which corroborated with our observations from mechanical testing (**Section 6.2**). Furthermore, n_{bb} contributed most significantly to modulus among these predictors while χ contributed the least.

Table 7.3: Fitting results summary of the multiple linear regression model for logarithmic Young's modulus E_0 fitted with forward selection.

Coefficient	Estimate	Std. Error	P-value
c_0	0.57	0.033	< 2E-16
c_1	-0.86	0.079	< 2E-16
c_2	0.36	0.079	1.52E-5
c_4	0.26	0.10	0.013

7.6 Complicated statistical models

The R^2 values for the multiple linear regression (MLR) models in **Section 7.5** suggested that the MLR models were underfitting and the relationship between architectural parameters [n_{bb}, n_L, n_{sc}, n_g, χ, T_g] and the mechanical parameters [β, E_0] needed to be described by more complicated models. Therefore, we trained decision tree, random forest, and gradient descent models. We tested both in-sample and out-of-sample performances of

these models to ensure that the models not only had high prediction accuracy, but also did not overfit the data. We used R^2 values to evaluate the in-sample fitting performance and percent error as the metrics for prediction performance. In addition to the types of models, we also investigated in the hyperparameters for each model to select the combination of hyperparameters that resulted in models with best fitting results as well as generalizability.

7.6.1 Decision Trees

To tune the performance of the decision tree model, we tuned the minimum sample split hyperparameter, which is the minimum number of samples required at each node before splitting. The smaller the minimum sample split, the more complicated the model is. **Figure 7.2** showed the effect of the minimum sample split on the percent error and the R^2 value of the decision tree model. As minimum sample split increased, the percent error increased and the R^2 value decreased, indicating that both in-sample and out-of-sample fit performances worsened. This observation was expected as the decision tree regression algorithm aims to minimize the standard deviation of each node. The more samples at each node, the higher the standard deviation.

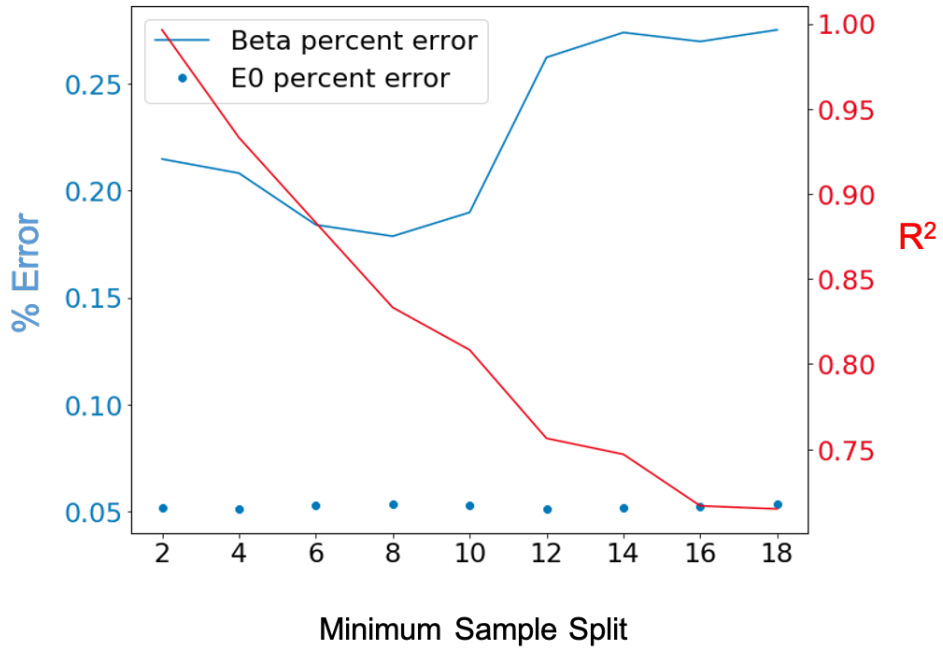

Figure 7.2: Effect of minimum sample split on in-sample and out-of-sample performance of the decision tree model. % Error = |predicted value – actual value| / actual value x 100%.

Next, we tested the effect of max depth of the tree parameter of the decision tree model. Once the tree's max depth is reached, it will not allow further splitting. **Figure 7.3** showed the effect of the max depth on the percent error and the R^2 value of the decision tree model. As we increased the maximum depth of the tree, R^2 increased and the percent error decreased, indicating the improvement of both in-sample and out-of-sample performance. However, it was noticeable that once the maximum depth exceeded 12, the improvement in R^2 and percent error became much less significant. Therefore, we could cap the max depth at 12 for the decision tree model to guarantee both model performance and efficiency.

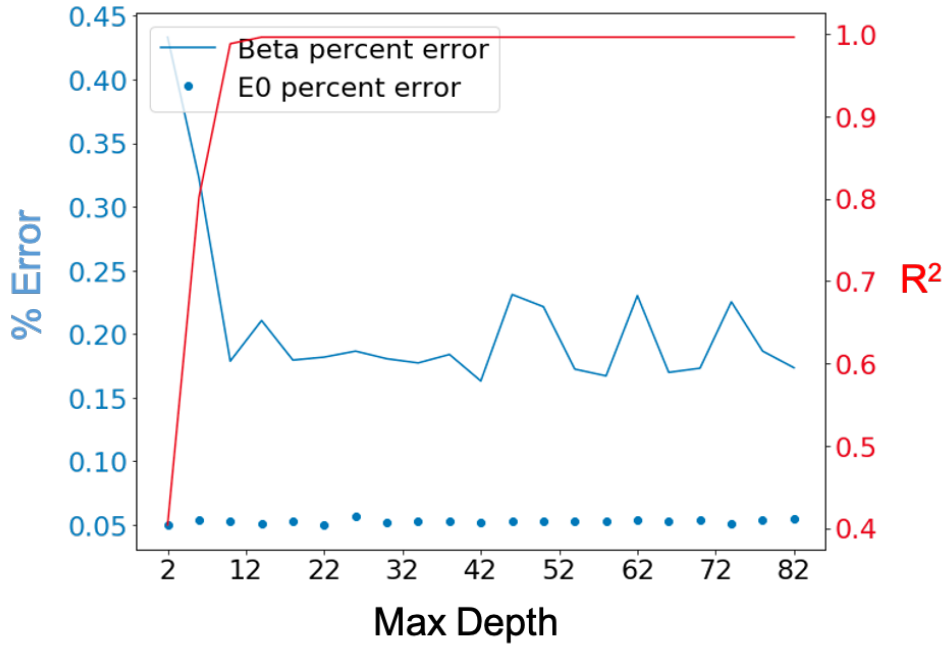

Figure 7.3: Effect of maximum depth of the tree on in-sample and out-of-sample performance of the decision tree model. % Error = |predicted value – actual value| / actual value x 100%.

An advantage of using decision tree was that it allowed us to view the importance of each feature in predicting the firmness and Young's modulus. **Figure 7.4** showed the feature importance of the decision tree model that was trained on standardized dataset. The parameter that had the highest influence over firmness and modulus was n_{sc}, which accounted for approximately 50% of the contribution. The next important feature was n_{bb}, which contributed to 30% of the mechanical properties. n_L, DP of the linear block, weighted 10% towards the firmness and modulus of the plastomers. The two parameters that contributed the least to the mechanical properties were the Flory-Huggins interaction parameter and the average glass transition temperature. Note that $n_g = 1$ for all samples in the training set, and therefore it was trivial to compute the feature importance of n_g.

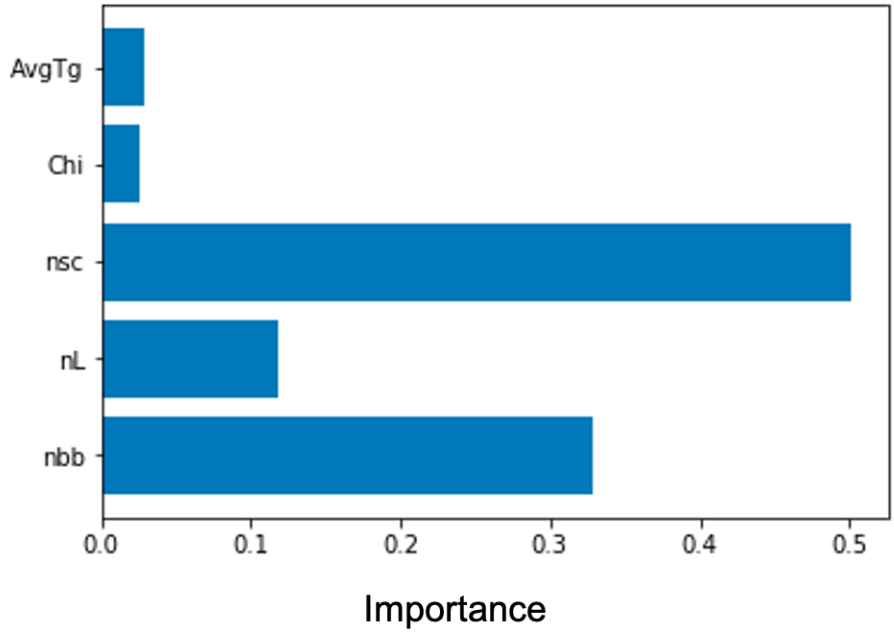

Figure 7.4: Feature importance of the decision tree model for predicting firmness and Young's modulus. AvgTg: average glass transition temperature between the linear block and the bottlebrush block; Chi: χ, Flory-Huggins interaction parameter; n_{sc}: Side chain length; n_L: DP of linear block; n_{bb}: Degree of polymerization (DP) of the bottlebrush backbone.

7.6.2 Random Forest

As introduced in **Section 7.2**, random forest model is an ensemble of decision trees. Therefore, in addition to the hyperparameters for decision trees, we were also able to tune the number of decision trees used in a random forest model. **Figure 7.5** showed the effect of number of decision trees on the percent error and R^2. As we increased the number of trees, R^2 increased, indicating that the in-sample fitting improved. However, after 40 trees, the percent error for firmness increased again, suggesting that the model was overfitting. Therefore, the optimal number of trees to use was 40.

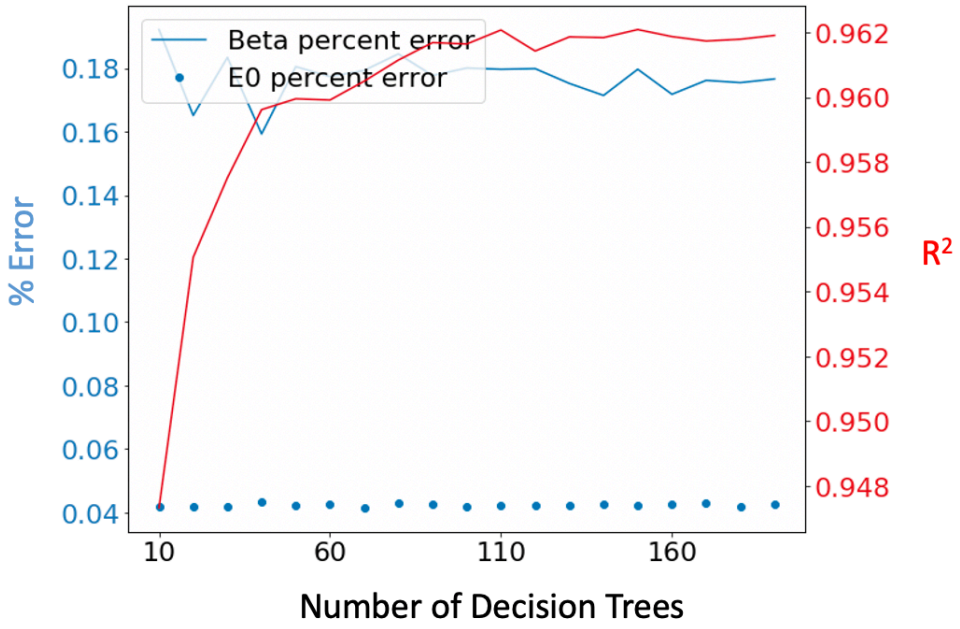

Figure 7.5: Effect of number of decision trees on in-sample and out-of-sample performance of the random forest model. % Error = |predicted value – actual value| / actual value x 100%.

7.6.3 Gradient Boosting

Similar to random forest, gradient boosting model also consists of multiple decision trees. Therefore, we also varied the number of trees used in the gradient boosting model. **Figure 7.6** showed the effect of number of decision trees on the percent error and R^2. As we increased the number of trees, R^2 increased and percent error decreased, indicating that both the in-sample and out-of-sample fitting improved. This was different from the conclusion we obtained for the random forest model. The reason for this phenomenon was due to the different mechanism of random forest and gradient boosting. Training samples are randomly distributed to the decision trees concurrently in random forest and the results are averaged, whereas gradient boosting model is built in a stage-wise manner and aims to improve the

worst performing tree's outcome at each stage. Therefore, having more trees allows further improvements and do not necessarily overfit the model.

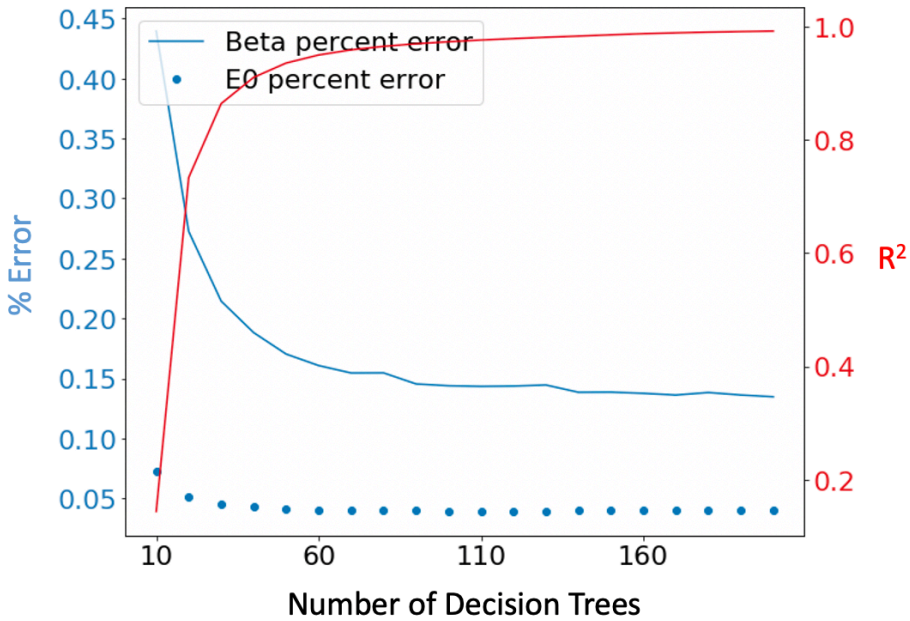

Figure 7.6: Effect of number of decision trees on in-sample and out-of-sample performance of the gradient boosting model. % Error = |predicted value – actual value| / actual value x 100%.

7.7 Neural Networks

The architecture of a typical neural network was shown in **Figure 7.7**. Our aim was to feed in a dataset containing all six features of the plastomers, [n_{bb}, n_L, n_{sc}, n_g, χ, T_g], and the model would in turn predict the [β, E_0] values based on these features.

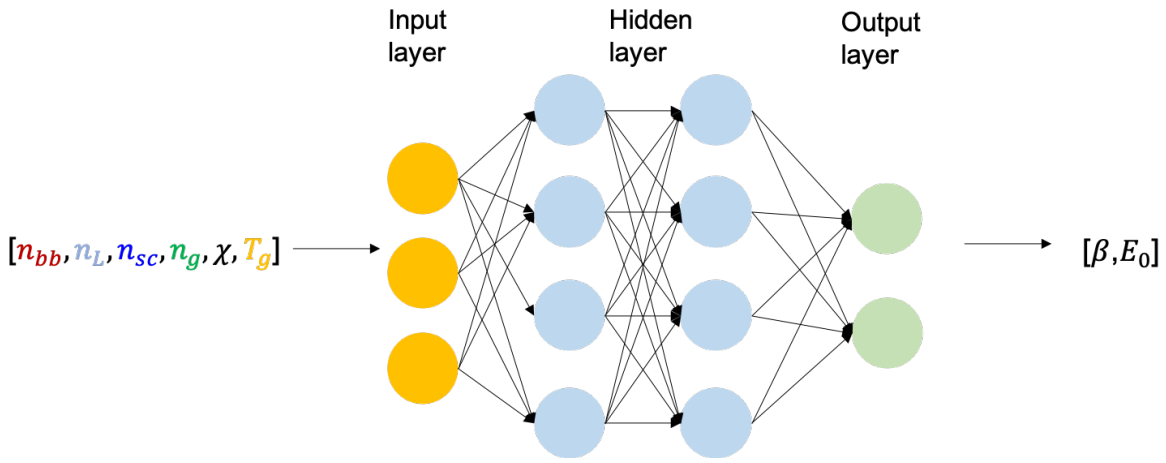

Figure 7.7: Architecture of a typical neural network.

Since each node in the neural network adds to the total number of parameters, the neural network can easily have a large number of parameters, causing the model to overfit. Therefore, in this study, we paid particular attention to the out-of-sample prediction performance to evaluate the generalizability of the neural network models. Two typical techniques used in neural networks to prevent overfitting are drop out and early stopping. The first method assigns a dropout probability to each node in the neural network, which is the probability that the value of a node will be turned to zero at an iteration. In this way, we decrease the number of parameters trained in the neural network. The second method keeps track of the loss at each iteration and stops the training early once the loss stops improving. **Figure 7.8** showed an example of the obtainable minimum mean absolute error (MAE), which was calculated by averaging the MAE of firmness and Young's modulus, when drop out or early stopping was applied. For all three models in **Figure 7.8**, the number of nodes in each hidden layer was 20. Neither drop out or early stopping was applied to the model in **Figure 7.8A**. Drop out was applied to **Figure 7.8B** and early stopping was applied to **Figure**

7.8C. Minimum MAE decreased when drop out or early stopping was applied, suggesting that these two techniques were effective in decreasing overfitting in neural networks. Note that the effect of applying both drop out and early stopping to neural networks was also investigated. However, the fitting performance of this scenario was worse compared to all three models in **Figure 7.8**, indicating that the model was underfitting when both techniques were used. Finally, **Figure 7.8** also showed that increasing the number of layers, which in turn increased the complexity of the model, did not result in higher prediction accuracy.

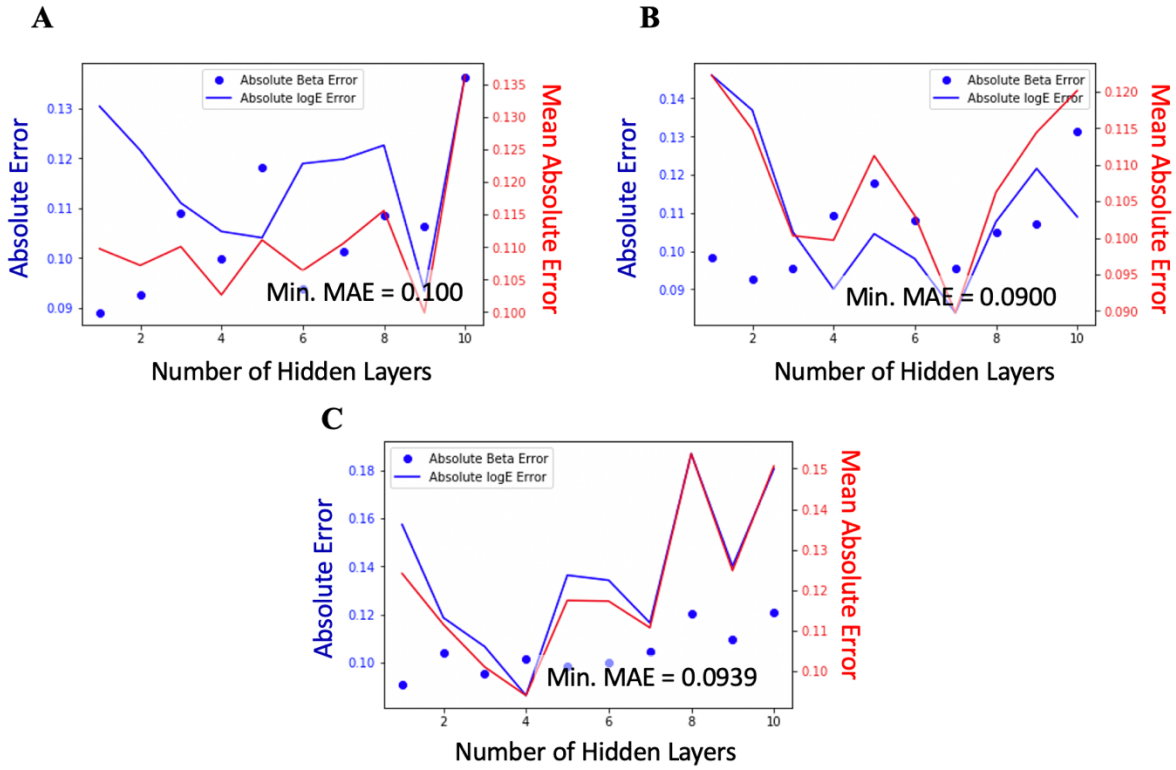

Figure 7.8: Decreasing the extent of overfitting of neural networks by drop out and early stopping. (A) Neither drop out or early stopping was applied. **(B)** Drop out was applied. **(C)** Early stopping was applied. The size of each layer was 20 for all three models. The mean absolute error (MAE) was calculated by averaging the MAE of firmness and Young's modulus.

7.8 Model performance summaries and comparisons

To compare the four models, we evaluated both in-sample and out-of-sample performances of the models using mean absolute error as a metric. The training dataset, which contained all plastomers produced in our group, was used to test the in-sampe performance. For out-of-sample performance, we used several samples synthesized by another research group in Carnegie Mellon University. All samples in the test set had unique combinations of [n_{bb}, n_L, n_{sc}, n_g, χ, T_g] that were never seen by any of the models during the training phase (**Table 7.4)**.

Table 7.4: Chemical and architectural composition of samples in the test set.

L block	BB block	n_{bb}	n_L	n_{sc}	n_g	χ	Avg T_g(°C)	β	$log(E_0)$
PNiPAM	POEOMA	399	328	25	2.7	1.44	31.5	0.60	4.86
PNiPAM	POEOMA	399	544	24	2.7	1.44	31.5	0.47	4.88
PNiPAM	POEOMA	399	1200	13	2.7	1.44	31.5	0.78	5.70
PNiPAM	POEOMA	399	1200	24	2.7	1.44	31.5	0.60	5.36
PNiPAM	POEOMA	399	1200	67	2.7	1.44	31.5	0.67	5.65
PNiPAM	POEOMA	399	2435	26	2.7	1.44	31.5	0.78	5.53
PNiPAM	POEOMA	399	3311	32	2.7	1.44	31.5	0.92	5.98

Table 7.5 displayed the training set and set mean absolute (MAE) errors using the models in **Section 7.5 – 7.7**, using the performance of multiple linear regression as a reference. As shown in **Table 7.5**, all four models outperformed the linear regression model in both in-sample and out-of-sample prediction performance. Although the neural network model only improved MAE by less than 0.05 compared to decision tree, random forest, and gradient boosting, it performed significantly better in the out-of-sample prediction using the

test set. This indicated that the neural network was the most generalizable compared to other models. Therefore, neural network was selected to be the final model used in strategic planning of plastomer production. The average percent error of firmness was 13.6% while that for Young's modulus was 6.07%, indicating that the neural network was accurate in predicting the mechanical properties of plastomers based on architectural encodings. However, it was more challenging for the model to predict firmness compared to Young's modulus.

Table 7.5: Mean absolute errors (MAE) of the training and test set using different statistical and machine learning models.

Model	Training set MAE	Test Set MAE
Multiple linear regression	0.090	0.19
Decision tree	0.076	0.14
Random forest	0.063	0.15
Gradient boosting	0.059	0.14
Neural network	0.058	0.095

The finalized and trained neural network model had three hidden layers and each hidden layer consisted of 20 nodes. Drop out was applied, with drop out probability = 50%. A candidate table was generated, containing possible combinations of [n_{bb}, n_L, n_{sc}, n_g, χ, T_g] (**APPENDIX 3**) that led to plastomers with firmness > 0.8 and modulus > 10^5 Pa. Guided by the table of possible candidates, as well as taking synthetic feasibility into consideration, two combinations were selected among the possible candidates. Two linear-bottlebrush-linear triblocks, PnBMA$_{280}$-*b*-P(PDMS$_{11}$MA)$_{100}$-*b*-PnBMA$_{280}$, and PBzMA$_{250}$-*b*-P(PDMS$_{11}$MA)$_{100}$-

b-PBzMA$_{250}$, were synthesized and plastomer films were prepared for mechanical measurements. **Table 7.6** and **Table 7.7** showed the proposed chemical structures vs. actual chemical structures of the synthesized triblocks, as well as the predicted mechanical properties vs. experimentally measured properties. Although the proposed n_L was 1100 for both blocks, due to synthetic limitation, we could only grow the DP of the linear blocks to 280 and 250 respectively. However, the resulting firmness and modulus were still higher than the predicted values. This indicated that our neural network underestimated the firmness and modulus when making predictions based on the combinations listed in **Table 7.6** and **Table 7.7**. This could be caused by two reasons: 1) our training data lacked samples with extremely high β (> 0.8) and E_0 (> 10^6 Pa), and 2) only a very small region of the stress-elongation responses of the samples could be characterized by the equation of state (**Figure 7.9, Section 2.2**), causing the fitting to be challenging. To solve these two problems, we can include more samples with extremely high firmness and modulus into the training data as well as seeking alternative synthetic systems other than LBL triblocks.

Table 7.6: Comparison between predicted and actual structures and mechanical properties of PnBMA$_{280}$-*b*-P(PDMS$_{11}$MA)$_{100}$-*b*-PnBMA$_{280}$

	n_{bb}	n_L	n_{sc}	n_g	χ	Avg T_g(°C)	β	$log(E_0)$
Predicted	100	1100	14	1	3	-50	0.80	5.33
Actual	100	280	14	1	2.89	-52	0.93	6.61

Table 7.7: Comparison between predicted and actual structures and mechanical properties of PBzMA$_{250}$-*b*-P(PDMS$_{11}$MA)$_{100}$-*b*-PBzMA$_{250}$

	n_{bb}	n_L	n_{sc}	n_g	χ	Avg T_g(°C)	β	$log(E_0)$
Predicted	100	1100	14	1	7	-20	0.81	5.37
Actual	100	250	14	1	6.76	-22.5	0.98	6.81

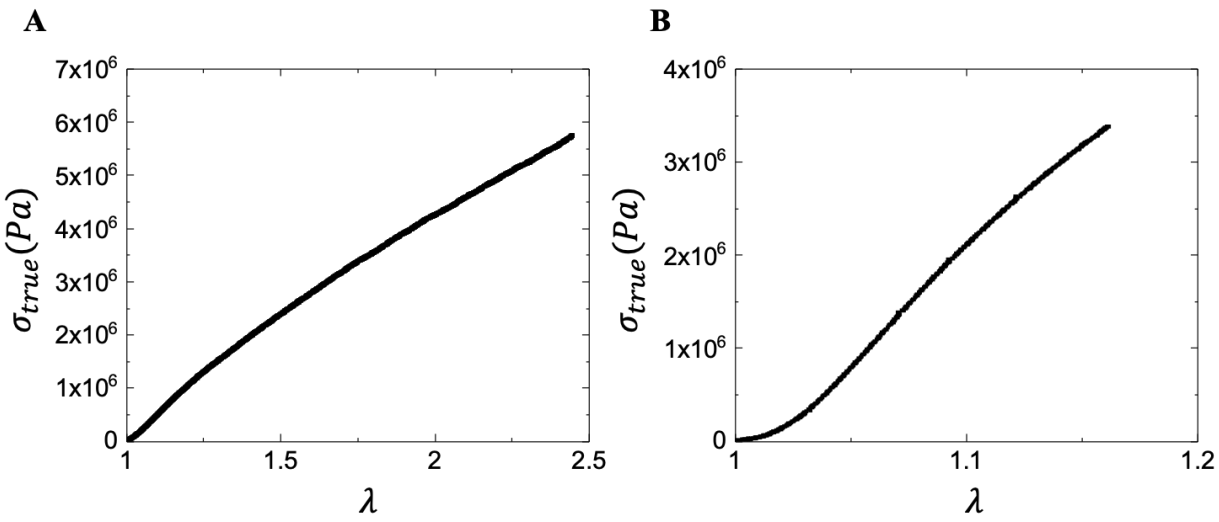

Figure 7.9: Stress-elongation responses of two triblocks synthesized using neural network guidance. (A) PnBMA$_{280}$-*b*-P(PDMS$_{11}$MA)$_{100}$-*b*-PnBMA$_{280}$ **(B)** PBzMA$_{250}$-*b*-P(PDMS$_{11}$MA)$_{100}$-*b*-PBzMA$_{250}$

Figure 7.10 displayed the position of the PnBMA$_{280}$-*b*-P(PDMS$_{11}$MA)$_{100}$-*b*-PnBMA$_{280}$ and PBzMA$_{250}$-*b*-P(PDMS$_{11}$MA)$_{100}$-*b*-PBzMA$_{250}$ on the tissue-plastomer map. = The strategically synthesized plastomers were able to fill in the gap between plastomers and tissues (**Figure 7.10A**). Moreover, the PBzMA$_{250}$-*b*-P(PDMS$_{11}$MA)$_{100}$-*b*-PBzMA$_{250}$ sample was able to recreate the stress-elongation response of posterior cruciate ligament (PCL) (**Figure 7.10B**).

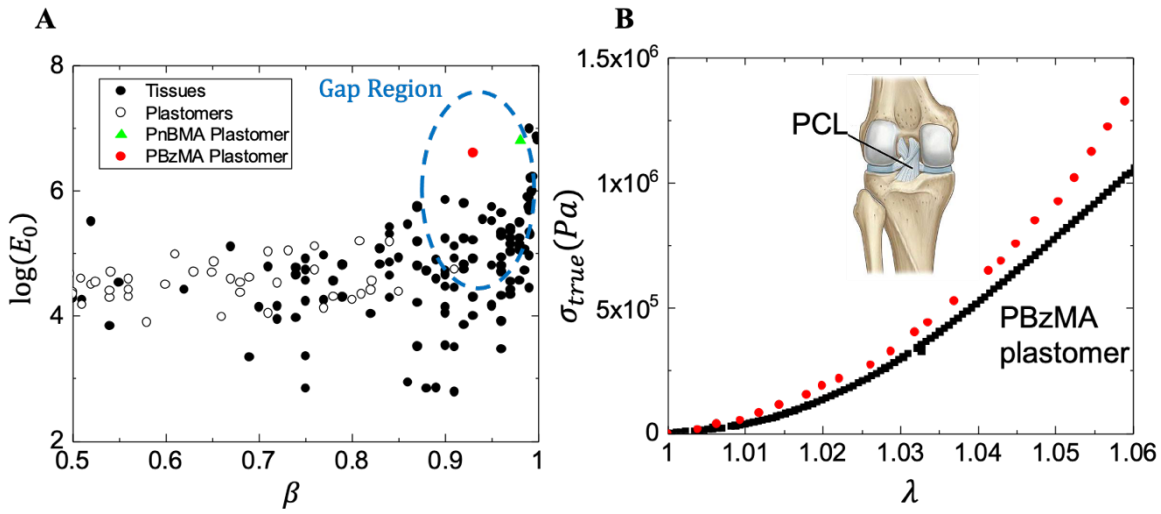

Figure 7.10: Strategically planned synthesis produced plastomers. (A) Machine learning assisted synthesis produced plastomers that fell into the gap region between tissues and synthetic plastomers. **(B)** Strategically planned synthesis of $PBzMA_{250}$-*b*-$P(PDMS_{11}MA)_{100}$-*b*-$PBzMA_{250}$ closely mimicked the stress-elongation response of posterior cruciate ligament (PCL).

7.9 Closing remarks

The large amount of tunable architectural encodings of the triblocks makes precisely targeting tissue-like mechanical properties challenging. This study overcame this challenge by adapting complex machine learning models to predict the modulus and firmness of the plastomers according to their architectural and chemical parameters accurately. The most accurate result was obtained by the neural network model. Hence, we successfully demonstrated the effectiveness and efficiency of utilizing advanced machine learning models in strategic planning of plastomer synthesis. This strategy provided a valuable method in target-oriented tissue-like material synthesis.

CHAPTER 8

Physical Origin of Structural Coloration

Structural coloration is produced by constructive interference of reflected lights at the boundary between each pair of layers[118,119]. In order for structural coloration to occur, two requirements need to be met: periodicity of two components, and difference in refractive indices of the two components. **Figure 8.1** showed the mechanism of two cases of structural coloration. In case 1 (**Figure 8.1A)**, when there are three layers and refractive indices $n_1 < n_2 < n_3$, the constructive interference can be described by $2n_2 d cos\theta_2 = m\lambda$, where d is the periodicity, θ_2 is the reflected angle, m is the number of repeated layers, and λ is the reflected wavelength. In order for the reflected light to fall in the visible range, the periodicity needs to be proportional to $\lambda/2$. In case 2 (**Figure 8.1B**), when there are two layers and refractive indices $n_A < n_B$, the constructive interference can be described as $2n_B d_A cos\theta_B = (m - \frac{1}{2})\lambda$, where d_A is the periodicity between B layers, θ_B is the reflection angle from the surface of layer B. In this case, periodicity d needs to be proportional to $\lambda/4$ to reflect light in the visible range. Overall, the wavelength of the reflected light can be tuned by tuning the length of the periodicity and the refractive indices of the two components.

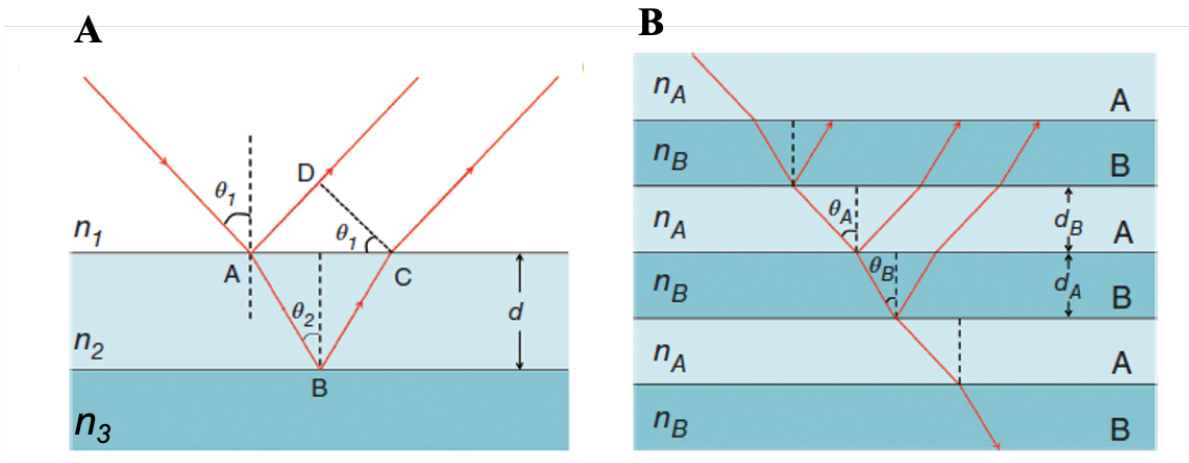

Figure 8.1: Mechanism of structural coloration. (**A**) Case 1: three layers, refractive indices $n_1 < n_2 < n_3$. (**B**) Case 2: two layers, refractive indices $n_A < n_B$.

CHAPTER 9

Controlling the Structural Coloration of Linear-Bottlebrush-Linear (LBL) Triblocks

9.1 Overview and Strategy

As mentioned in **Chapter 8**, the premises of materials displaying structural coloration are periodicity and contrast in refractive index. The microphase separation of linear-bottlebrush-linear triblock copolymers formed hard linear domains distributed uniformly in soft bottlebrush matrix. Therefore, there existed periodic patterns in plastomers similar to chameleons (**Section 1.3**). This theory was confirmed by tapping mode atomic force microscopy (AFM) as shown in **Figure 9.1**.

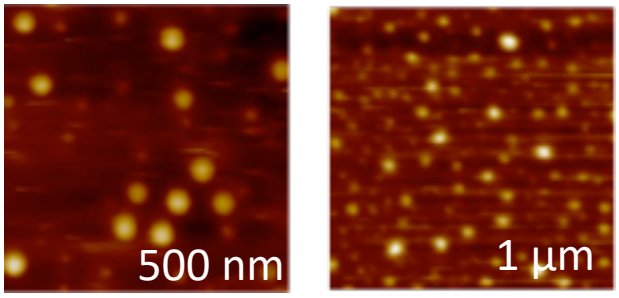

Figure 9.1: AFM of PBzMA$_{1100}$-*b*-P(PDMS$_{11}$MA)$_{940}$-*b*-PBzMA$_{1100}$ triblocks triblock copolymer.

Two strategies can be used to control the color of the plastomers with structural coloration. Recall that the reflected wavelength λ can be described by 1) $2n_2 d cos\theta_2 = m\lambda$, where d is the periodicity, θ_2 is the reflected angle, m is the number of repeated layers, and

2) as $2n_B d_A cos\theta_B = (m - \frac{1}{2})\lambda$, where $d_A$is the periodicity between B layers, θ_B is the reflection angle from the surface of layer B (**Chapter 8**). Therefore, to shift the reflected wavelength into the visible range, we can either increase the periodicity d or increase the refractive index n. In this study, our primary candidate for the linear block is PBzMA as its average refractive index is ~1.57, which is higher than PMMA or poly(n-butyl methacrylate) (PnBtMA). Using the protocol optimized in **Chapter 5**, we synthesized series of PBzMA-*b*-P(PDMS$_{11}$MA)-*b*-PBzMA triblock copolymers (**Table 9.1**). The entries highlighted in blue were the ones that displayed blue color. The rest were colorless with the exception of PBzMA$_{1100}$-bbPDMS$_{940}$-PBzMA$_{1100}$, which was white. The samples that displayed blue color either had high linear block volume fraction ϕ_L or high n_{bb}, both cases increased the periodicity.

Table 9.1: PBzMA-*b*-P(PDMS$_{11}$MA)-*b*-PBzMA architectural parameters[a].

n_{sc}	n_{bb}	n_L	ϕ_L
14	320	150	0.12
	320	260	0.19
	850	50	0.02
	850	230	0.07
	850	340	0.10
	850	460	0.13
	940[b]	**1100**	**0.25**
	1010	170	0.05
	1010	230	0.06
	1010	340	0.09
	1150	250	0.06
	1150	470	0.11

a. The entries highlighted in blue were samples that displayed blue color. b. Although sample had high n_L and ϕ_L, it displayed an opaque white color.

9.2 Effect of n_L on reflected color

Figure 8.2 showed the reflectance spectroscopy of a series of PBzMA-*b*-P(PDMS$_{11}$MA)-*b*-PBzMA where n_{bb}=850, n_{sc}=14, and n_L=50, 230, 340, and 460. Triblocks with n_L=50, 230 did not show reflectance in the visible region (400 – 700 nm), where triblocks with n_L=340 and 460 showed positive %reflectance at 400 nm. The reflectance of n_L= 460 triblock was slightly higher than that of n_L= 340 as longer n_L increased the periodicity by increasing the radius of the linear domains (**Section 6.1**).

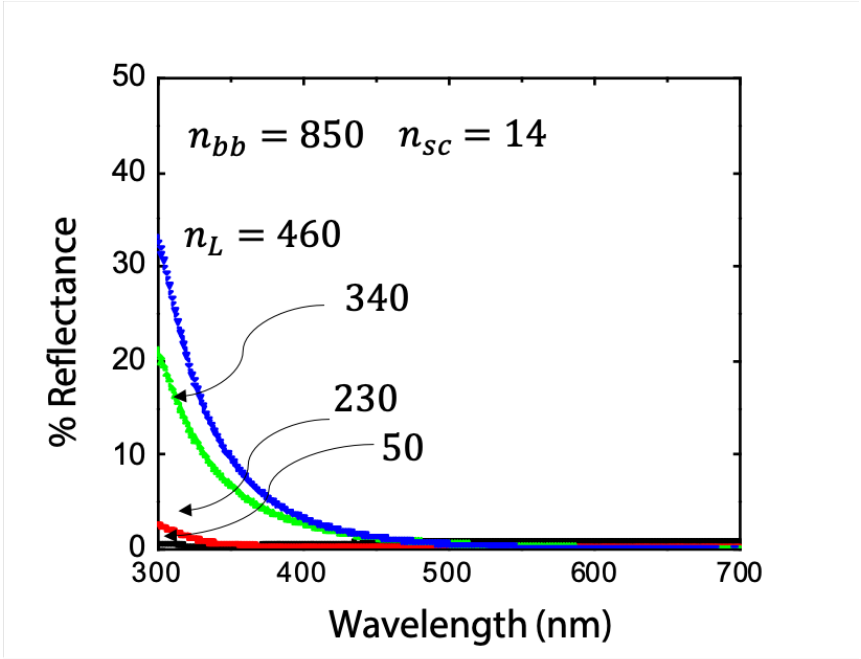

Figure 9.2: Effect of n_L on the reflectance of PBzMA-bbPDMS-PBzMA triblocks.

9.3 Effect of swelling on reflected color

The difference in coloration in the above series was caused by varying chemical structure and architectural parameters. Another method of controlling coloration was from external stimuli. Although some dried plastomers did not show visible color, they displayed color while dissolved in solution. We hypothesized that this was due to the triblock being swollen while dissolved, increasing its periodicity. To test this hypothesis, we performed a drying experiment using a series of PBzMA-*b*-P(PDMS$_{11}$MA)-*b*-PBzMA with n_{bb} = 1150, n_{sc}= 14 and varied ϕ_L.

A drop of 25 wt% PBzMA-*b*-P(PDMS$_{11}$MA)-*b*-PBzMA in toluene solution was dropped onto a smooth surface for each sample. Pictures were taken at 10 min, 20 min, and 40 min intervals. The drying process was shown in **Figure 9.3**. Initially, all three droplets were blue, and as time went by, the color gradually blue-shifted, which was due to the shrinkage of periodicity while the material was being dried.

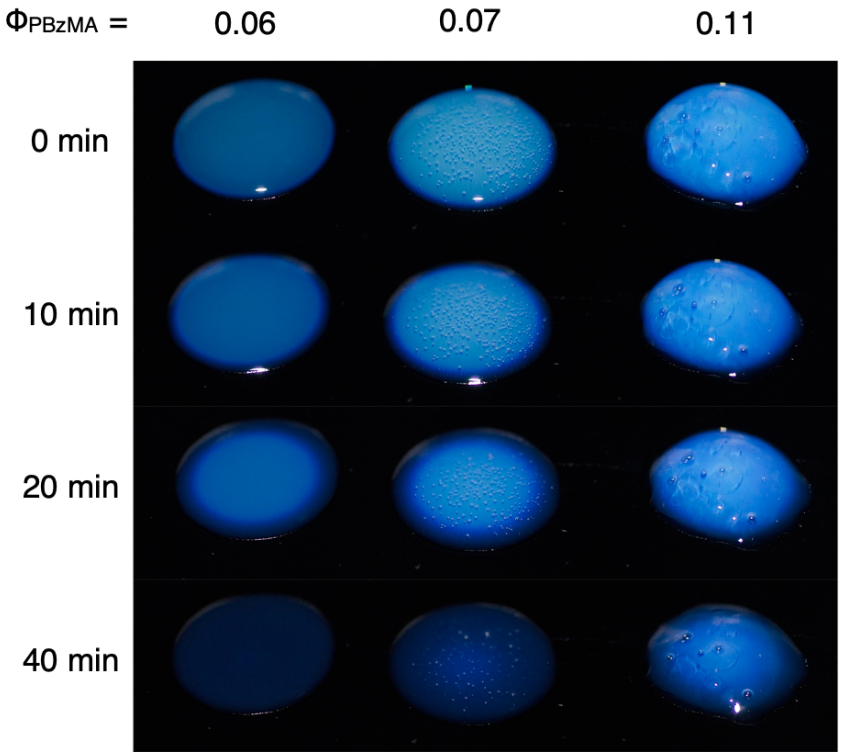

Figure 9.3: Drying process of PBzMA-*b*-P(PDMS$_{11}$MA)-*b*-PBzMA from toluene.

Next, we performed a deswelling experiment in which we swelled PBzMA$_{470}$-bbPDMS$_{1150}$-PBzMA$_{470}$ with hexane and then let the hexane evaporate. Hexane selectively swelled the bottlebrush backbone, and the linear block was insoluble in hexane. As shown in **Figure 9.4**, the swollen plastomer appeared turquoise, and the color blue-shifted while the hexane was evaporating. When the bottlebrush backbone was swollen, the space between the

spherical linear domain increased, which increased periodicity, causing the plastomer to appear turquoise. When the hexane evaporated, the periodicity decreased to the original value, and hence the color blue-shifted.

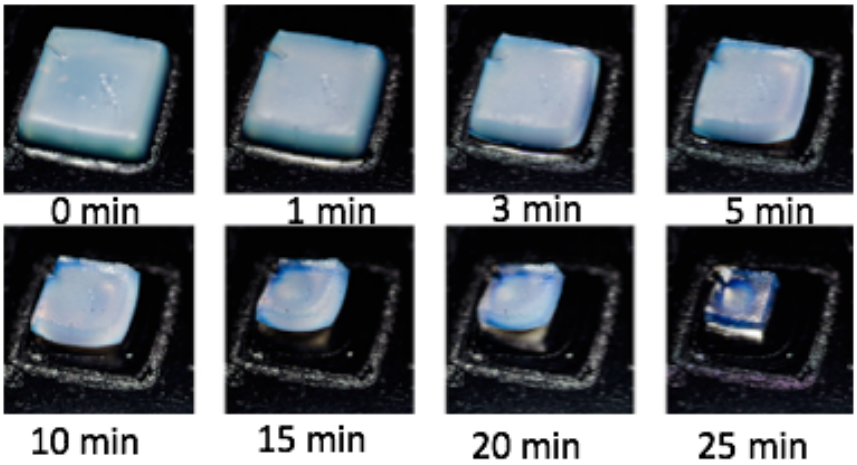

Figure 9.4: Deswelling of PBzMA-*b*-P(PDMS$_{11}$MA)-*b*-PBzMA triblock from hexane.

Finally, we measured the swelling effect on structural coloration quantitively via UV-Vis spectrophotometer. 0.1 mL PDMS$_{11}$MA macromonomer was absorbed by each dry piece of PBzMA-*b*-P(PDMS$_{11}$MA)-*b*-PBzMA triblock, where n_{bb}=850, n_{sc}=14, and n_L=50, 230, 340, and 460. Each piece was approximately 1 cm^2 in area and 0.5 mm in thickness. Once the macromonomer droplet was absorbed, the reflectance of each film was measured and compared to its dry state. As shown in **Figure 9.5**, the reflectance of the swollen plastomer films all increased compared to the dry films. Since PDMS$_{11}$MA macromonomer only dissolves the P(PDMS$_{11}$MA) bottlebrush backbone, the distance between linear domains of the plastomer increased upon swelling, causing the reflectance to red shift.

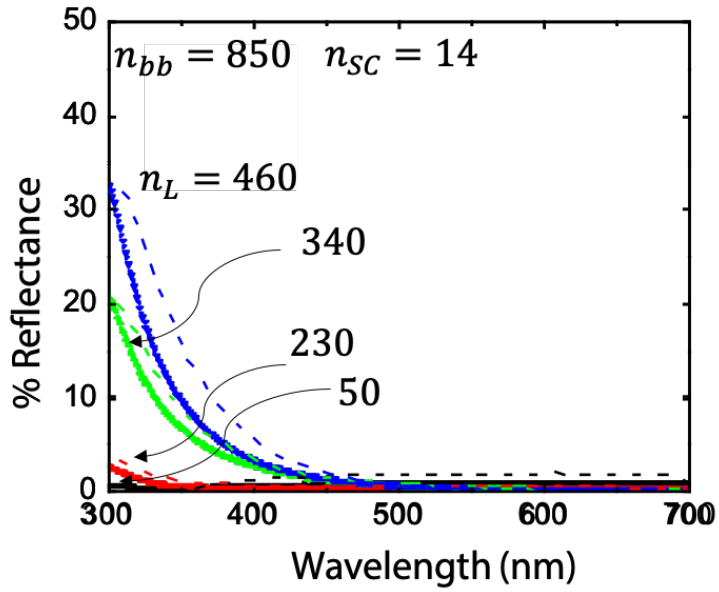

Figure 9.5: Effect of swelling on the reflectance of PBzMA-*b*-P(PDMS$_{11}$MA)-*b*-PBzMA triblocks. Solid: dry plastomer. Dashed: swollen with PDMS macromonomer.

9.4 Small Angle X-Ray Scattering (SAXS) of LBL triblocks

Interested in the effect of n_{bb} and ϕ_L on the periodicity of the plastomers, a series of SAXS experiments were performed. In particular, we measured the distance between bottlebrush strands d_1, radius of the linear domain d_2, and the distance between linear domains d_3 (**Figure 9.6**).

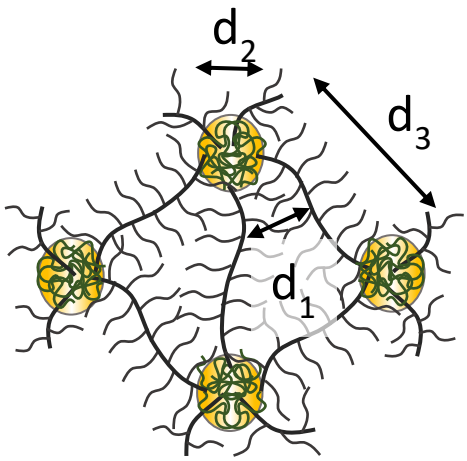

Figure 9.6: Illustration of distances in plastomer networks measurable by SAXS. d_1: Radius of the linear domain. d_2: Distance between bottlebrushes. d_3: Distance between linear domains.

First, we compared a series of PBzMA-*b*-P(PDMS$_{11}$MA)-*b*-PBzMA of varied n_{bb} but same n_{sc} and approximately the same ϕ_L. **Figure 9.7** and **Table 9.2** showed the comparison of the plastomers. The inter-distance between the bottlebrushes was not affected by the length of the bottlebrush backbone. The distance between linear domains increased linearly with the increase in n_{bb}. Note that the B300-3 sample did not show a peak corresponding to d_3. This could be due to the relatively high dispersity of the radius of the linear domain. The radii of the three samples were approximately in the same order of magnitude, which was around 30 nm. This was expected as the volume fraction of the three samples were roughly the same, around 0.11.

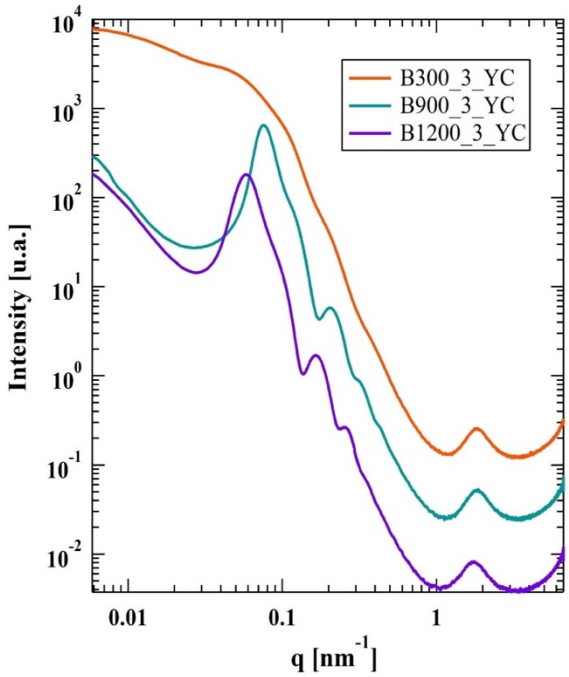

Figure 9.7: SAXS spectra for PBzMA-*b*-P(PDMS$_{11}$MA)-*b*-PBzMA with varied n_{bb}, $\phi_L \sim 0.11$.

Table 9.2: SAXS results for PBzMA-*b*-P(PDMS$_{11}$MA)-*b*-PBzMA with varied n_{bb}, $\phi_L \sim 0.11$.

Name	n_{bb}	n_L	ϕ_L	d_1 (nm)	d_2 (nm)	d_3 (nm)	Radius Polydispersity (%)
B300-3	320	150	0.12	3.41	24.7	-	28.8
B900-3	850	340	0.10	3.39	25.8	82	12.5
B1200-3	1150	470	0.11	3.57	32.7	107	10.9

The same experiment was performed on a series of PBzMA-*b*-P(PDMS$_{11}$MA)-*b*-PBzMA with higher ϕ_L (**Figure 9.8, Table 9.3**). Similar to the previous series, the inter distance between brushes remained consistent, so did the radius of the linear domains. Although the radius of the B300-4 sample was smaller compared to the other two samples, it could be due to the fact the dispersity of the radius was high (32.4) and hence affected the average radius. In contrast to the previous series, the distance between linear domains did not have a strong correlation with n_{bb}. Therefore, it was inconclusive whether the value of n_{bb} had a direct impact on the periodicity.

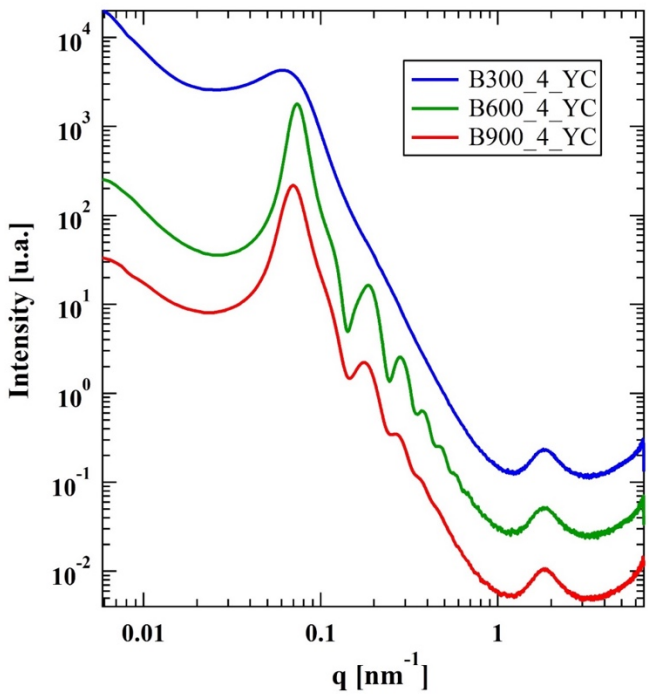

Figure 9.8: SAXS spectra for PBzMA-*b*-P(PDMS$_{11}$MA)-*b*-PBzMA with varied n_{bb}, $\phi_L \sim 0.15$.

Table 9.3: SAXS results for PBzMA-*b*-P(PDMS$_{11}$MA)-*b*-PBzMA with varied n_{bb}, ϕ_L~0.15.

Name	n_{bb}	n_L	ϕ_L	d_1 (nm)	d_2 (nm)	d_3 (nm)	Radius Polydispersity (%)
B300-4	320	260	0.19	3.40	23.7	104	32.4
B600-4	540	350	0.15	3.41	31.3	85	7.0
B900-4	850	460	0.13	3.41	31.0	90	11.2

Next, we investigated in the effect of n_L on the domain size and distances. SAXS measurements were performed on a series of PBzMA-*b*-P(PDMS$_{11}$MA)-*b*-PBzMA triblocks with the same n_{bb} and n_{sc} but different n_L (**Figure 9.9, Table 9.4**). The distance between bottlebrush backbones remained the same with varied n_L. The distance between linear domains and the radius of the linear domain increased consistently with the increase of n_L. This corroborated with our theory in **Section 6.1** that the higher curvature of the linear domain caused the bottlebrush backbone to be more pre-strained. Furthermore, we confirmed that increasing n_L increased periodicity.

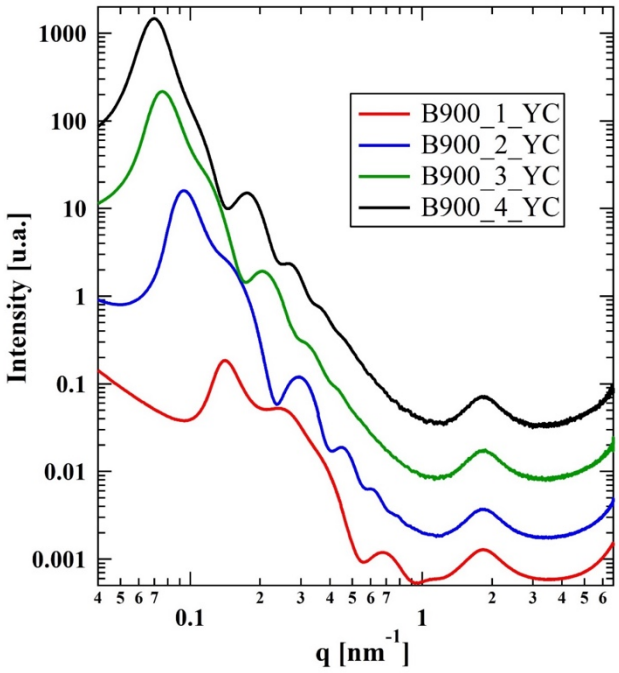

Figure 9.9: SAXS spectra for PBzMA-*b*-P(PDMS$_{11}$MA)-*b*-PBzMA with varied n_L.

Table 9.4: SAXS results for PBzMA-*b*-P(PDMS$_{11}$MA)-*b*-PBzMA with varied n_L.

Name	n_{bb}	n_L	ϕ_L	d_1 (nm)	d_2 (nm)	d_3 (nm)	Radius Polydispersity (%)
B900-1	850	50	0.02	3.40	8.0	44	11
B900-2	850	230	0.07	3.40	18.9	66	9.2
B900-3	850	340	0.10	3.39	25.8	82	12.5
B900-4	850	460	0.13	3.41	31.0	90	11.2

Finally, we investigated in the effect of swelling on periodicity. $PBzMA_{460}$-$P(PDMS_{11}MA)_{850}$-$PBzMA_{460}$ was swollen with 10, 20, 60, and 90 wt% $PDMS_{11}MA$ macromonomer respectively and measured by SAXS. The corresponding domain distances were shown in **Table 9.5**. Both the distance between bottlebrushes and between linear domains increased with respect to wt% of $PDMS_{11}MA$ macromonomer added. Meanwhile, the radius of the linear domain remained constant. This proved that the addition of $PDMS_{11}MA$ macromonomer selectively swelled the bottlebrush backbone and increased the periodicity. Consequently, the reflected wavelengths of the swollen plastomer red-shifted.

Table 9.5: Effect of swelling on the inter-distances of plastomers.

$PDMS_{11}MA$ Wt %	**d_1 (nm)**	**d_2 (nm)**	**d_3 (nm)**
0	3.41	31.0	90
10	3.58	31.3	93
20	3.70	31.2	95
60	4.37	31.0	104
90	4.80	31.1	111

Figure 9.10 showed the correlation between change in microscopic volume of plastomers and swelling ratio. The change in microscopic volume of the plastomer was estimated by a ratio of $d_2{d_1}^2/d_{2,0}{d_{1,0}}^2$. The change in volume increased with respect to swelling ratio, however; the former had a higher increase rate compared to swelling ratio.

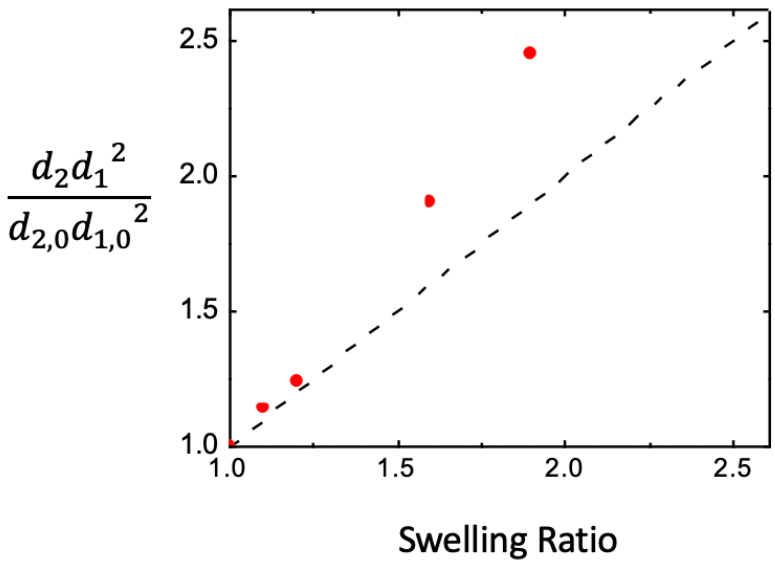

Figure 9.10: Effect of swelling ratio on the change in volume of the plastomers according to inter-distances measured by SAXS.

9.5 Closing remarks

In this chapter, we thoroughly investigated in methods to control the color of plastomers. SAXS measurements demonstrated that there was high order periodicity in the plastomers. The periodicity could be increased by increasing n_L and n_{bb} although the former was more effective than the latter. Furthermore, swelling could also act as an external stimuli to change the reflected wavelength of the plastomer. However, so far all plastomers synthesized showed blue color. In order to red-shift the color, alternative strategies needed to be considered. For example, we could potentially increase the Flory-Huggin parameter between the linear and bottlebrush blocks to increase the extent of pre-strain of the bottlebrush backbone. Furthermore, bulkier linear blocks could be used to increase the periodicity.

CHAPTER 10

Future Works

10.1 Introduction

In this study, we demonstrated that plastomers, physical networks formed by micro-phase separation of linear-bottlebrush-linear triblock copolymers, were capable of incorporating multiple biological tissues' defensive properties, such as softness, firmness, and structural coloration. More importantly, this multifunctionality was achieved by micro-phase separation of one single molecule, which remained stable under ambient condition, without leeching or needing additives. By controlling the architectural and chemical parameters [n_{bb}, n_L, n_{sc}, n_g, χ, T_g], plastomers with a wide range of mechanical and optical properties could be produced.

To overcome the synthetic challenge and produce materials with consistent and robust properties, as well as making the production process as cost-effective as possible, we have optimized our strategies from both synthetic and planning levels. From synthetic perspective, we investigated the effect of side products on the mechanical properties of plastomers and conducted a systematic investigation on the kinetics of the grafting-polymerization of $PDMS_{11}MA$ macromonomer to optimize the synthetic conditions. For the planning stage, we built statistical and machine learning models to predict the mechanical properties of plastomers based on architectural and chemical information, so that we can directly target the tissues of interest.

In addition to the achievements discussed above, the plastomer system offered great potential in the discovery of functional materials. For instance, so far, we have demonstrated the structural coloration of plastomers, but we are currently limited to the blue wavelength region, and the change in coloration upon stimuli is mostly verified from microscopic level, using UV-Vis spectroscopy or SAXS. In addition to the softness, firmness, and structural coloration, we can incorporate additional properties that are crucial to biomedical applications using the current plastomer architectural framework. From the synthetic perspective, we have currently focused on grafting-through polymerization of $PDMS_{11}MA$ macronomer and proved its success and ease of use. However, limitations exist with this method, especially when we are aiming for triblocks with high n_{sc}. Additional polymerization methods to synthesize the bottlebrush macroinitiator, such as grafting-from, can be investigated, so that we can use different chemicals to produce plastomers and unlock more properties.

10.2 Red-shifting plastomer color

In **Chapter 9**, we showed various methods to control the coloration of plastomers, such as varying the architectural parameters and applying external stimuli. However, so far, the colors displayed all fall in the blue wavelength range, and the external stimuli were limited to swelling. To truly mimic chameleon-like skins, we need to synthesize materials that displayed color in the red-side of the visible spectrum without external stimuli. **Figure 10.1** showed an example of applying mechanical stimulus to plastomer. At relaxed state, the plastomer exhibits a red color and upon tensile stress, the periodicity decreases, causing the color to blue shift. To achieve this, we propose to establish a quantitative relationship

between inter-domain distances of the plastomer and architectural parameters, as well as investigating in the mechanism of microphase separation of triblocks. **Chapter 9** proved that higher n_{bb} led to higher inter-domain distance. However, the increase in inter-domain distance was not linearly dependent on the increase in n_{bb}. By studying the microphase separation mechanism, we will be able to discover factors that affect the inter-domain distance in addition to n_{bb}.

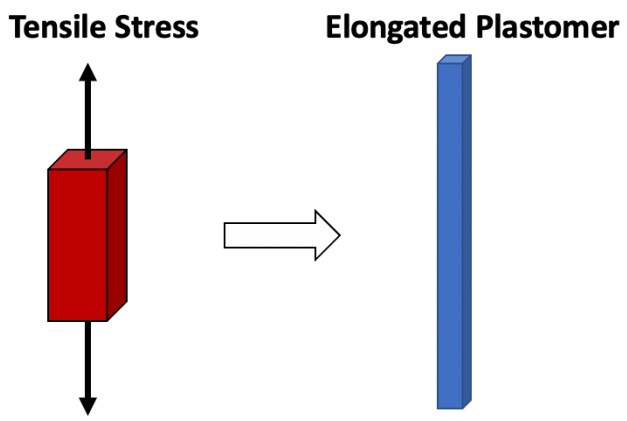

Figure 10.1: Plastomer's color blue-shifts upon applying tensile stress.

10.3 Soft-to-hard injectables

Since plastomers mimic tissues' mechanical properties and are stable under ambient conditions, they are ideal candidates for biomedical applications such as implants. The plastomer's architectural framework provides a solid foundation for controlling its tissue-like mechanical properties. Therefore, we can vary the chemical composition to add additional functionalities to the plastomers, as we did with the structural coloration. In this case, we can

adapt hydrophilic polymers with low critical solution temperature (LCST) into our triblock so that at elevated temperature, the triblock phase separates from the homogenous aqueous solution to form gels. For example, we can use poly(N-isopropylacrylamide) (PNiPAM) as the linear block and bottlebrush poly(ethylene glycol) (PEG) as the bottlebrush block. This triblock is soluble in water at room temperature and can phase separate at body temperature to form physical networks since PNiPAM has an LCST around 30 ºC[121-123]. Since the gelation occurs within the body, this material can be used as injectables for implants so that both implanting and removing of the implants do not depend on invasive procedures.

10.4 Alternative synthetic methods

With the right synthetic conditions, grafting-through polymerization has been proven to be an effective method in synthesizing bottlebrush macroinitiator. However, there are still underlying limitations with this method. As discussed in **Section 5.2**, the bulkier the monomer, the higher the equilibrium monomer concentration, and consequently, the lower the resulting DP. This limitation hinders the synthesis of triblocks with high n_{sc} and high n_{bb}, and in turn, blocks a wide range of mechanical properties of the plastomers. Alternatively, we can utilize the grafting-from polymerization method to synthesize the bottlebrush macroinitiator. This method involves two steps: 1) A linear backbone with initiation sites is synthesized, and 2) Side chains are grown from the initiation sites until desired n_{sc} is reached[124]. This method avoids the equilibrium monomer concentration challenge of macromonomers, and therefore allows the synthesis of triblocks of long side chains.

10.5 Closing Remarks

Biological creatures undergo the long process of evolution to develop a system of intricate compartments with different functionalities that work perfectly together to guarantee their chances of survival. As scientists, we aspire to recreate such functionalities in synthetic materials to fulfill the needs in medicine and therapeutics. Furthermore, as technology progresses, we aim to not only develop novel materials but also discover advanced methods that assist in the production of multifunctional materials. This project successfully produced bio-mimicking plastomers, optimized robust synthetic protocols to improve the reproducibility and consistency of the plastomers, and finally, introduced the effectiveness of using machine learning approach in strategic synthetic planning. It demonstrated a streamline process that utilized artificial intelligence to improve the efficiency of synthesizing materials with properties of interest. So far, we have illustrated applying artificial intelligence in the synthesis of organic polymers that mimicked biological tissues' softness and firmness. With ample data, this technique can be generalized to a variety of tissue-like properties.

APPENDIX 1: MECHANICAL PARAMETERS OF TISSUES FROM LITERATURE

Category	Type	β	E_0 (kPa)	λ_{fit}	λ_{max}	Ref
Adipose	IDC	0.89	79.8	1.21	1.28	125
Adipose	Fibro	0.77	93.9	1.28	1.29	125
Adipose	DCI	0.88	52.8	1.24	1.30	125
Adipose	Omental	0.90	11.1	1.24	1.34	126
Adipose	Subcataneous	0.91	3.2	1.21	1.30	126
Adipose	Subcataneous	0.91	0.62	1.26	1.26	127
Adipose	Fibro	0.97	106.8	1.13	1.14	128
Adipose	Lobular	0.97	140.1	1.15	1.15	128
Adipose	Gland	0.97	35.7	1.15	1.15	128
Adipose	Fat	0.97	26.7	1.15	1.15	128
Adipose	Gland	0.90	45.9	1.22	1.22	129
Adipose	Breast	0.98	53.3	1.05	1.05	130
Adipose	Fibro	0.99	28.0	1.04	1.05	130
Adipose	Subcataneous	0.88	0.70	1.30	1.30	131
Adipose	Subcataneous	0.89	0.72	1.23	1.26	131
Adipose	Kidney	0.98	116	1.05	1.06	132
Adipose	Breast	0.97	22.2	1.10	1.11	133
Cartilage	Intervertebral disc	0.93	82.7	-	-	134
Cartilage	Intervertebral disc	0.96	86.6	-	-	134
Dense regular	Fascia	0.87	562	1.32	1.32	135

Dense regular	MCL	0.99	9800.	1.07	1.15	136
Dense regular	Tendon	0.999	6400.	1.02	1.06	137
Dense regular	PCL	0.998	7300.	1.02	1.07	138
Dense regular	PL	0.87	155	1.28	1.35	139
Dense regular	PL	0.93	10.2	1.33	2.58	140
Dense regular	PL	0.97	22.2	1.30	2.09	140
Dense regular	PL	0.95	15.1	1.30	2.40	140
Dense irregular	Pericardium	0.97	176	1.13	1.20	141
Dense irregular	Pericardium	0.96	63.8	1.16	1.19	141
Dense irregular	Cornea	0.991	1600	1/05	1.06	142
Dense irregular	Cornea	0.992	940	1.05	1.08	142
Dense irregular	Cornea	0.988	810	1.05	1.08	142
Dense irregular	Cornea	0.989	790	1.05	1.08	142
Dense irregular	Cornea	0.991	520	1.05	1.08	142
Dense irregular	Cornea	0.994	1700	1.04	1.06	142
Dense irregular	Cornea	0.993	1000	1.04	1.08	142
Dense irregular	Cornea	0.989	550	1.06	1.08	142
Dense irregular	Skin dermis	0.99	760	1.05	1.36	143
Dense irregular	Skin dermis	0.87	534	1.18	1.36	143
Dense irregular	Skin dermis	0.92	67.4	1.18	1.19	143
Dense irregular	Skin dermis	0.96	444	1.10	1.25	143
Dense irregular	Skin dermis	0.92	639	1.13	1.17	143
Dense irregular	Skin dermis	0.85	84.9	1.24	1.60	143

Dense irregular	Skin dermis	0.71	61.5	1.38	1.60	143
Dense irregular	Skin dermis	0.72	14.3	1.46	2.10	143
Dense irregular	Skin dermis	0.90	13.9	1.16	2.10	143
Dense irregular	Cornea	0.99	580.	1.05	1.08	144
Dense irregular	Cornea	0.90	724	-	-	145
Dense irregular	Skin dermis	0.93	164	-	-	146
Dense irregular	Skin dermis	0.84	206	-	-	147
Dense irregular	Skin dermis	0.90	174	-	-	148
Dense irregular	Skin dermis	0.74	59.1	-	-	149
Dense irregular	Zonular filament	0.92	7.20	-	-	150
Dense irregular	Spinal cord	0.84	71.8	-	-	151
Elastic	Aorta	0.87	64.0	1.32	1.32	152
Elastic	Aorta	0.79	66.4	1.35	1.35	152
Elastic	Artery	0.79	66.0	1.42	1.42	153
Elastic	Artery	0.75	55.2	1.50	1.50	153
Elastic	Artery	0.78	36.7	1.48	1.48	153
Elastic	Artery	0.84	44.9	1.35	1.40	153
Elastic	Aorta	0.98	115	1.10	1.35	154
Elastic	Aorta	0.94	351	1.16	1.32	155
Elastic	Aorta	0.92	172	1.23	1.32	155
Elastic	Aorta	0.89	39.2	1.30	1.47	155
Elastic	Aorta	0.91	131	1.22	1.38	155
Elastic	Aorta	0.91	83.8	1.25	1.40	155

Elastic	Aorta	0.83	120.	1.18	1.57	155
Elastic	Aorta	0.97	256	1.14	1.30	156
Elastic	Aorta	0.83	120.	1.18	1.57	157
Elastic	Aorta	0.98	310/	1.10	1.25	158
Elastic	Aorta	0.96	214	1.14	1.46	158
Elastic	Aorta	0.90	53.1	1.28	1.60	158
Elastic	Aorta	0.96	51.3	1.15	1.69	158
Elastic	Artery	0.99	480.	1.05	1.05	159
Elastic	Artery	0.97	227	1.12	1.12	159
Elastic	Artery	0.96	191	1.13	1.13	159
Elastic	Aorta	0.67	128	-	-	160
Elastic	Blood vessel	0.75	37.4	-	-	161
Elastic	Artery	0.91	28.8	-	-	162
Epithelial	Fetal membrane	0.79	20.1	-	-	163
Epithelial	Alveolar wall	0.87	3.30	-	-	164
Cardiac muscle	Aortic valve	0.99	220.	1.09	1.12	165
Cardiac muscle	Heart valve	0.92	55.5	1.28	1.28	166
Skeletal muscle	Skeletal muscle	0.95	330.	1.14	1.27	167
Skeletal muscle	Skeletal muscle	0.96	210.	1.17	1.27	167
Skeletal muscle	Vocal fold	0.82	11.0	1.38	1.40	168
Skeletal muscle	Vocal fold	0.84	19.7	1.35	1.39	168
Skeletal muscle	Vocal fold	0.74	45.4	1.37	1.40	168
Skeletal muscle	Skeletal muscle	0.75	82.6	1.45	1.46	169

Skeletal muscle	Skeletal muscle	0.77	17.9	1.48	1.48	169
Skeletal muscle	Skeletal muscle	0.98	125	1.10	1.47	169
Cardiac muscle	Heart valve	0.99	92.0	1.09	1.10	170
Cardiac muscle	Heart valve	0.991	200.	1.10	1.10	170
Cardiac muscle	Heart valve	0.98	175	1.13	1.13	170
Cardiac muscle	Heart valve	0.98	140.	1.13	1.20	170
Cardiac muscle	Heart valve	0.96	21.3	1.19	1.24	170
Cardiac muscle	Heart valve	0.87	16.5	1.32	1.36	170
Cardiac muscle	Heart valve	0.98	37.0	1.12	1.21	170
Cardiac muscle	Heart valve	0.95	65.0	1.20	1.23	170
Skeletal muscle	Skeletal muscle	0.86	289	1.21	1.38	171
Skeletal muscle	Skeletal muscle	0.50	19/4	1.62	2.03	171
Cardiac muscle	Heart muscle	0.96	8.30	-	-	172
Skeletal muscle	Vocal fold	0.93	20.0	-	-	173
Skeletal muscle	Single muscle fiber	0.75	2.30	-	-	174
Skeletal muscle	Skeletal muscle	0.90	29.5	-	-	175
Nervous	Brain	0.47	1.30	1.58	1.6	176
Nervous	Brain	0.38	0.98	1.22	1.63	177
Nervous	Brain	0.74	9.4	1.26	1.28	178
Nervous	Brain	0.70	13.8	1.28	1.28	178
Nervous	Brain	0.75	17.5	1.28	1.28	178
Nervous	Brain	0.51	18.4	1.29	1.29	179

Nervous	Brain	0.62	26.6	1.26	1.30	179
Nervous	Brain	0.55	34.3	1.30	1.30	179
Nervous	Brain	0.90	3.4	1.21	1.21	180
Nervous	Brain	0.86	0.88	1.29	1.36	180
Nervous	Brain	0.75	0.70	-	-	181
Reticular	Liver	0.45	0.282	2.13	2.29	182
Reticular	Liver	0.95	557	1.10	1.21	183
Reticular	Liver	0.95	14.4	1.11	1.11	183
Reticular	Spleen	0.52	325	1.16	1.57	183
Reticular	Spleen	0.19	47.7	1.70	1.78	183
Reticular	Lung	0.69	2.20	-	-	

APPENDIX 2: PLASTOMER DATABASE FOR MODEL TRAINING

Name	n_{bb}	n_L	n_{sc}	χ	AvgT$_g$ (°C)	β	E_0 (kPa)
PMMA - PDMS 14	302	57	14	4.84	-10	0.48	12.8
PMMA - PDMS 14	302	117	14	4.84	-10	0.56	20.4
PMMA - PDMS 14	302	181	14	4.84	-10	0.69	41.5
PMMA - PDMS 14	602	295	14	4.84	-10	0.3	4.9
PMMA - PDMS 14	602	351	14	4.84	-10	0.35	6.9
PMMA - PDMS 14	602	677	14	4.84	-10	0.42	10.1
PMMA - PDMS 14	602	803	14	4.84	-10	0.51	15.3
PMMA - PDMS 14	938	190	14	4.84	-10	0.29	5.4
PMMA - PDMS 14	938	325	14	4.84	-10	0.33	6.5
PMMA - PDMS 14	938	656	14	4.84	-10	0.45	11.8
PMMA - PDMS 14	938	1235	14	4.84	-10	0.67	39.3
PMMA - PDMS 14	1065	360	14	4.84	-10	0.26	5.1
PMMA - PDMS 14	1065	480	14	4.84	-10	0.3	6.4
PMMA - PDMS 14	1065	810	14	4.84	-10	0.36	7.8
PMMA - PDMS 70	112	105	70	4.84	-10	0.71	106.2
PMMA - PDMS 70	112	131	70	4.84	-10	0.76	130
PMMA - PDMS 70	112	185	70	4.84	-10	0.84	155.7
PMMA - PDMS 70	296	156	70	4.84	-10	0.77	13.3
PMMA - PDMS 70	296	285	70	4.84	-10	0.8	18.3
PMMA - PDMS 70	296	507	70	4.84	-10	0.85	24.8
PMMA - PDMS 70	296	754	70	4.84	-10	0.91	55.7
PMMA - PDMS 70	447	288	70	4.84	-10	0.71	11.2
PMMA - PDMS 70	447	604	70	4.84	-10	0.78	20.4
PMMA - PDMS 70	447	772	70	4.84	-10	0.81	22.3
PMMA - PDMS 70	447	894	70	4.84	-10	0.82	26.3
PMMA - PDMS 14	1483	867	14	4.84	-10	0.33	3.7
PMMA - PDMS 14	1765	365	14	4.84	-10	0.4	3.4

PMMA - PDMS 14	1765	545	14	4.84	-10	0.48	5
PMMA - PDMS 14	1765	780	14	4.84	-10	0.58	7.9
P(OEOMA) - PDMS 14	900	240	14	9.61	-95.5	0.6	32
PMMA - PDMS/MMA 7.5	336	78	7.5	4.84	-10	0.08	19.5
PMMA - PDMS/MMA 7.5	336	102	7.5	4.84	-10	0.11	28.4
PMMA - PDMS/MMA 7.5	336	119	7.5	4.84	-10	0.13	33.9
PMMA - PDMS/MMA 10.8	196	34	10.8	4.84	-10	0.18	14.3
PMMA - PDMS/MMA 10.8	196	58	10.8	4.84	-10	0.24	26.9
PMMA - PDMS/MMA 10.8	196	64	10.8	4.84	-10	0.28	29
PMMA - PDMS/MMA 12.9	197	29	12.9	4.84	-10	0.19	11.8
PMMA - PDMS/MMA 12.9	197	52	12.9	4.84	-10	0.31	22.5
PMMA - PDMS/MMA 12.9	197	76	12.9	4.84	-10	0.36	30.5
PMMA - PDMS 14.4	363	57	14.4	4.84	-10	0.35	17.5
PMMA - PDMS 14.4	363	116	14.4	4.84	-10	0.44	33.2
PMMA - PDMS 14.4	363	168	14.4	4.84	-10	0.49	36.1
PMMA - PDMS 23.6	285	88	23.6	4.84	-10	0.45	29.2
PMMA - PDMS 23.6	285	123	23.6	4.84	-10	0.52	31.8
PMMA - PDMS 23.6	285	201	23.6	4.84	-10	0.56	38.9
PMMA - PDMS 33.8	249	62	33.8	4.84	-10	0.46	13.2
PMMA - PDMS 33.8	249	106	33.8	4.84	-10	0.5	24.2
PMMA - PDMS 33.8	249	133	33.8	4.84	-10	0.56	26.5
PMMA - PDMS 47.1	308	187	47.1	4.84	-10	0.68	23.6
PMMA - PDMS 47.1	308	261	47.1	4.84	-10	0.72	33.5

PMMA - PDMS 47.1	308	430	47.1	4.84	-10	0.76	55.4
PMMA - PDMS 14.4	559	315	14.4	4.84	-10	0.365	20.8
PMMA - PDMS 71.2	302	410	71.2	4.84	-10	0.821	36.3
PtBMA - PDMS 14.4	283	178	14.4	1.44	-3.5	0.482	33.8
PtBMA - PDMS 14.4	283	178	14.4	1.44	-3.5	0.525	35.1
PiPMA - PDMS 14.4	283	170	14.4	2.56	-18	0.492	39.1
PiPMA - PDMS 14.4	283	170	14.4	2.56	-17.5	0.509	40.2
PBzMA - PDMS 14.4	283	158	14.4	6.76	-22.5	0.497	46.9
PBzMA - PDMS 14.4	283	158	14.4	6.76	-22.5	0.541	51.0
MMA - PIB 20	341	643	20	2.56	16	0.652	73.2
MMA - PIB 20	341	872	20	2.56	16	0.732	111
MMA - PIB 20	341	989	20	2.56	16	0.808	157
P(HEMA-r-MMA) - PDMS 14	296	120	14	22.09	-11.5	0.65	49.6
P(HEMA-r-MMA) - PDMS 14	296	92	14	22.09	-11.5	0.61	97.8
P(HEMA-r-MMA) - PDMS 14	900	1006	14	22.09	-11.5	0.41	56.7
PBzMA - PDMS 14	1010	170	14	6.76	-22.5	0.35	3
PBzMA - PDMS 14	1010	230	14	6.76	-22.5	0.37	3.9
PBzMA - PDMS 14	1010	340	14	6.76	-22.5	0.4	5.1
PBzMA - PDMS 14	940	1100	14	6.76	-22.5	0.66	9.7
PBzMA - PDMS 14	850	50	14	6.76	-22.5	0.22	7.5
PBzMA - PDMS 14	850	240	14	6.76	-22.5	0.34	16.8
PBzMA - PDMS 14	850	350	14	6.76	-22.5	0.42	16.6
PBzMA - PDMS 14	850	460	14	6.76	-22.5	0.5	22.5
PBzMA - PDMS 14	320	150	14	6.76	-22.5	0.54	19.6
PBzMA - PDMS 14	320	260	14	6.76	-22.5	0.68	34.6
PBzMA - PDMS 14	1150	470	14	6.76	-22.5	0.33	6.9

PMMA - PDMS 14	938	358	14	4.84	-10	0.3	16.2
PMMA/PAMMA - PDMS 14	320	150	14	4.84	-10	0.43	11.6
PMMA - PDMS 14	288	230	14	4.84	-10	0.63	50.5
PBzMA - PDMS 14	860	260	14	6.76	-22.5	0.41	18
PBzMA - PDMS 14	860	540	14	6.76	-22.5	0.54	25.5
PBzMA - PDMS 14	860	330	14	6.76	-22.5	0.38	11.3
PBzMA - PDMS 14	860	330	14	6.76	-22.5	0.32	4.4
PBzMA - PDMS 14	860	460	14	6.76	-22.5	0.46	15.5
PBzMA - PDMS 14	860	240	14	6.76	-22.5	0.28	3.2

APPENDIX 3: PLASTOMER CANDIDATES

nbb	nL	nsc	ng	Chi	AvgTg (ºC)	beta	logE
100	1100	14	1	3	-50	0.80	5.33
100	1100	14	1	3	-20	0.81	5.42
100	1100	14	1	3	-10	0.81	5.42
100	1100	14	1	5	-50	0.81	5.30
100	1100	14	1	5	-20	0.81	5.41
100	1100	14	1	5	-10	0.81	5.40
100	1100	14	1	7	-50	0.81	5.28
100	1100	14	1	7	-20	0.81	5.37
100	1100	14	1	7	-10	0.81	5.38
100	1300	14	1	3	-50	0.82	5.34
100	1300	14	1	3	-20	0.83	5.43
100	1300	14	1	3	-10	0.83	5.47
100	1300	14	1	5	-50	0.82	5.31
100	1300	14	1	5	-20	0.83	5.43
100	1300	14	1	5	-10	0.83	5.45
100	1300	14	1	7	-50	0.83	5.28
100	1300	14	1	7	-20	0.83	5.40
100	1300	14	1	7	-10	0.83	5.43
100	1500	14	1	3	-50	0.83	5.34
100	1500	14	1	3	-20	0.84	5.44
100	1500	14	1	3	-10	0.85	5.48
100	1500	14	1	5	-50	0.84	5.31
100	1500	14	1	5	-20	0.84	5.44
100	1500	14	1	5	-10	0.84	5.47
100	1500	14	1	7	-50	0.84	5.29
100	1500	14	1	7	-20	0.84	5.42
100	1500	14	1	7	-10	0.84	5.46

100	1700	14	1	3	-50	0.85	5.34
100	1700	14	1	3	-20	0.86	5.45
100	1700	14	1	3	-10	0.86	5.49
100	1700	14	1	5	-50	0.85	5.32
100	1700	14	1	5	-20	0.86	5.45
100	1700	14	1	5	-10	0.86	5.48
100	1700	14	1	7	-50	0.86	5.29
100	1700	14	1	7	-20	0.86	5.43
100	1700	14	1	7	-10	0.86	5.47
100	1900	14	1	3	-50	0.86	5.34
100	1900	14	1	3	-20	0.87	5.45
100	1900	14	1	3	-10	0.87	5.49
100	1900	14	1	5	-50	0.86	5.32
100	1900	14	1	5	-20	0.87	5.45
100	1900	14	1	5	-10	0.87	5.48
100	1900	14	1	7	-50	0.87	5.29
100	1900	14	1	7	-20	0.87	5.43
100	1900	14	1	7	-10	0.87	5.47
100	2100	14	1	3	-50	0.87	5.34
100	2100	14	1	3	-20	0.88	5.45
100	2100	14	1	3	-10	0.89	5.49
100	2100	14	1	5	-50	0.88	5.32
100	2100	14	1	5	-20	0.88	5.45
100	2100	14	1	5	-10	0.88	5.49
100	2100	14	1	7	-50	0.88	5.29
100	2100	14	1	7	-20	0.88	5.43
100	2100	14	1	7	-10	0.88	5.48
100	2300	14	1	3	-50	0.89	5.34
100	2300	14	1	3	-20	0.89	5.45

100	2300	14	1	3	-10	0.90	5.50
100	2300	14	1	5	-50	0.89	5.32
100	2300	14	1	5	-20	0.89	5.45
100	2300	14	1	5	-10	0.89	5.49
100	2300	14	1	7	-50	0.89	5.29
100	2300	14	1	7	-20	0.89	5.43
100	2300	14	1	7	-10	0.89	5.48
100	2500	14	1	3	-50	0.90	5.34
100	2500	14	1	3	-20	0.90	5.45
100	2500	14	1	3	-10	0.91	5.50
100	2500	14	1	5	-50	0.90	5.32
100	2500	14	1	5	-20	0.90	5.45
100	2500	14	1	5	-10	0.90	5.49
100	2500	14	1	7	-50	0.90	5.29
100	2500	14	1	7	-20	0.90	5.44
100	2500	14	1	7	-10	0.90	5.48
100	2700	14	1	3	-50	0.91	5.34
100	2700	14	1	3	-20	0.91	5.45
100	2700	14	1	3	-10	0.91	5.50
100	2700	14	1	5	-50	0.91	5.32
100	2700	14	1	5	-20	0.91	5.45
100	2700	14	1	5	-10	0.91	5.49
100	2700	14	1	7	-50	0.91	5.29
100	2700	14	1	7	-20	0.91	5.44
100	2700	14	1	7	-10	0.91	5.48
100	2900	14	1	3	-50	0.91	5.34
100	2900	14	1	3	-20	0.92	5.45
100	2900	14	1	3	-10	0.92	5.49
100	2900	14	1	5	-50	0.91	5.32

100	2900	14	1	5	-20	0.92	5.45
100	2900	14	1	5	-10	0.92	5.49
100	2900	14	1	7	-50	0.91	5.27
100	2900	14	1	7	-20	0.92	5.44
100	2900	14	1	7	-10	0.92	5.49
100	3100	14	1	3	-50	0.92	5.33
100	3100	14	1	3	-20	0.93	5.45
100	3100	14	1	3	-10	0.93	5.49
100	3100	14	1	5	-50	0.92	5.30
100	3100	14	1	5	-20	0.93	5.45
100	3100	14	1	5	-10	0.93	5.49
100	3100	14	1	7	-50	0.92	5.26
100	3100	14	1	7	-20	0.92	5.44
100	3100	14	1	7	-10	0.93	5.49
100	3300	14	1	3	-50	0.93	5.32
100	3300	14	1	3	-20	0.93	5.45
100	3300	14	1	3	-10	0.93	5.49
100	3300	14	1	5	-50	0.93	5.29
100	3300	14	1	5	-20	0.93	5.45
100	3300	14	1	5	-10	0.93	5.48
100	3300	14	1	7	-50	0.93	5.24
100	3300	14	1	7	-20	0.93	5.44
100	3300	14	1	7	-10	0.93	5.49
100	3500	14	1	3	-50	0.93	5.30
100	3500	14	1	3	-20	0.94	5.44
100	3500	14	1	3	-10	0.94	5.48
100	3500	14	1	5	-50	0.93	5.28
100	3500	14	1	5	-20	0.94	5.44
100	3500	14	1	5	-10	0.94	5.48

100	3500	14	1	7	-50	0.93	5.22
100	3500	14	1	7	-20	0.94	5.44
100	3500	14	1	7	-10	0.94	5.48
100	3700	14	1	3	-50	0.94	5.29
100	3700	14	1	3	-20	0.94	5.44
100	3700	14	1	3	-10	0.94	5.48
100	3700	14	1	5	-50	0.94	5.26
100	3700	14	1	5	-20	0.94	5.44
100	3700	14	1	5	-10	0.94	5.48
100	3700	14	1	7	-50	0.94	5.21
100	3700	14	1	7	-20	0.94	5.44
100	3700	14	1	7	-10	0.94	5.48
100	3900	14	1	3	-50	0.94	5.28
100	3900	14	1	3	-20	0.95	5.44
100	3900	14	1	3	-10	0.95	5.48
100	3900	14	1	5	-50	0.94	5.25
100	3900	14	1	5	-20	0.95	5.44
100	3900	14	1	5	-10	0.95	5.48
100	3900	14	1	7	-50	0.94	5.20
100	3900	14	1	7	-20	0.95	5.44
100	3900	14	1	7	-10	0.95	5.48

REFERENCES

1. Bar-Cohen, Y. *Biomimetics: Nature-Based Innovation,* Taylor & Francis, 2012.

2. Allen, R. (ed) *Bulletproof Feathers: How Science Uses Nature's Secret to Design Cutting-edge Technology,* University of Chicago, 2010.

3. Primrose, S. B. *Biomimetics: Nature-Inspired Design and Innovation*, 1st ed.; John Wiley & Sons Ltd, 2020.

4. Mohammad, N.; Nature-Inspired Discoveries and Inventions, 2016. Dawn Web site. https://www.dawn.com/news/1297127 (accessed Feb 23, 2021).

5. Mäthger, L. M., Denten, E. J., Marshall, N. J., Hanlon, R. T., Mechanisms and behavioural functions of structural coloration in cephalopods. *J. R. Soc. Interface* **6**, S149-S163 (2009).

6. Teyssier, J., Saenko, S. V., Marel, D. V. D., Milinkovitch, M. C., Photonic crystals cause active color change in chameleons. *Nat. Comm.* **6**, 6368 (2015).

7. Mäthger, L. M., Denten, E. J., Marshall, N. J., Hanlon, R. T., Mechanisms and behavioural functions of structural coloration in cephalopods. *J. R. Soc. Interface* **6**, S149-S163 (2009).

8. Cuthill, I. C. et al., The biology of color. *Science* **357**, eaan0221 (2017).

9. G. A. Holzapfel, in *Handbook of Material Behavior Models,* J. Lemaitre, Ed. (Academic Press, 2001), pp. 1057-1071.

10. Richard-Blum, S., The collagen family. *Cold Spring Harb Perspect Biol.* **3**, a004978 (2011).

11. Lodish, H., Berk, A., Zipursky, S. L., et al. *Collagen: The Fibrous Proteins of the Matrix*, Molecular Cell biology. 4th ed.; W. H. Freeman, 2000. Section 22.3.

12. Muiznieks, L. D., Keeley, F. W., Molecular assembly and mechanical properties of the extracellular matrix: A fibrous protein perspective. *Biochimica et Biophysic Acta* **1832**, 866-875 (2013).

13. C. Storm, J. J. Pastore, F. C. MacKintosh, T. C. Lubensky, P. A. Janmey, Nonlinear elasticity in biological gels. *Nature,* **435***,* 191-194 (2005).

14. Greenleaf, J. F., Fatemi, M., Insana, M., Selected methods for imaging elastic properties of biological tissues. *Annu. Rev. Biomed. Eng.* **5**, 57-78 (2003).

15. Demiray, H., A note on the elasticity of soft biological tissues. *J. Biomechanics* **5**, 309-311 (1972).

16. Potyrailo, R. A., Ghiradella, H., Vertiatchikh, A., Dovidenko, K., Cournoyer, J. R., Olson, E. *Morpho* butterfly wing scales demonstrate highly selective vapour resonse. *Nat. Photonics* **1**, 123-128 (2007).

17. Zi, J. et al., Coloration strategies in peacock feathers. *PNAS.* **100**, 12576-12578 (2003).

18. So, J., Tayi, A.S., Günder, F., Whitesides, G. M., Stepped moduli in layered composites. *Adv. Funct. Mater.* **24**, 7197-7204 (2014).

19. Martinez, R. V., Glavan, A. C., Keplinger, C., Oyetibo, A. I., Whitesides, G. M., Soft actuators and robots that are resistant to mechanical damage. *Adv. Mater.* **24**, 3003-3010 (2014).

20. Vantankhah-Varnosfaderani, M. et al., Bottlebrush elastomers: a new platform for freestanding electroactuation. *Adv. Mater.* **29**, 1604209 (2017).

21. Trung, T. Q., Ramasundaram, S., Hwang, B., Lee, N., An all-elastic transparent and stretchable temperature sensor for body-attachable wearable electronics. *Adv. Mater.* **28**, 502-509 (2016).

22. Minns, R. J., Soden, P. D., Jackson, D. S., The role of the fibrous components and ground substance in the mechanical properties of biological tissues: a preliminary investigation. *J. Biomechanics***6**, 153-165 (1973).

23. Gosline, J. et al., Elastic proteins: biological roles and mechanical properties. *Phil. Trans. R. Soc. Lond. B***357**, 121-132 (2002).

24. Ranzani, T., Gerboni, G., Cianchetti, M., Menciassi, A., A bioinspired soft manipulator for minimally invasive surgery. *Bioinspir. Biomim.***10**, 035008 (2015).

25. Lee, J., Macosko, C. W., Urry, D. W., Mechanical properties of cross-linked synthetic elastomeric polypentapeptides. *Macromolecules***34**, 5968-5974 (2001).

26. Vatankhah-Varnosfaderani, M. et al., Mimicking biological stress-strain behaviour with synthetic elastomers. *Nature* **549**, 497-501 (2017).

27. Dobrynin, A. V., Carrillo, J. M. Y., Universality in nonlinear elasticity of biological and polymeric networks and gels. *Macromolecules* **44**,140-146 (2011).

28. Villa-Forte, A., Tissues and Organs. *Merck and the Merck Manuals.* Consumer ed. Merck & Co., Inc., NJ.

29. Rice University. *Anatomy and Physiology*. OpenStax, 2013. Chapter 4.1.

30. Rice University. *Anatomy and Physiology*. OpenStax, 2013. Chapter 4.2.

31. Rice University. *Anatomy and Physiology*. OpenStax, 2013. Chapter 4.4.

32. Rice University. *Anatomy and Physiology*. OpenStax, 2013. Chapter 4.5.

33. Rice University. *Anatomy and Physiology*. OpenStax, 2013. Chapter 4.3.

34. Muiznieks, L. D., Keeley, F. W., Molecular assembly and mechanical properties of the extracellular matrix: A fibrous protein perspective. *Biochimica et Biophysic Acta* **1832**, 866-875 (2013).

35. Culav, E. M., Clark, C. H., Merrilees, M. J., Connective tissues: Matrix composition and its relevance to physical therapy. *Physical Therapy* **79(3)**, 308-319 (1999).

36. Parry, D. A. D., The molecular and fibrillar structure of collagen and its relationship to the mechanical properties of connective tissue. *Biophysical Chemistry* **29**, 195-209 (1988).

37. Khan, T. et al., Metabolic dysregulation and adipose tissue fibrosis: Role of collagen VI. *Mol. Cell Biol.* **29**, 1575-1591 (2009).

38. Georgiev, G. P. et al., Light and electron microscopic study of the medial collateral ligament epiligament tissue in human knees. *World J. Orthop.* **18(5)**, 372-378 (2017).

39. Woo, S. L-Y., Takakura, Y., Liang, R., Jia, F., Moon, D. K., Treatment with bioscaffold enhances the fibril morphology and the collagen composition of healing medial collateral ligament in rabbits. *Tissue Engineering* **12(1)**, 159-166 (2006).

40. Pingel, J. et al., 3-D ultrastructure and collagen composition of healthy and overloaded human tendon: evidence of tenocyte and matrix buckling. *J. Anat.* **224**, 548-555 (2014).

41. Danysh, B. P., Duncan, M. K., The lense capsule. *Exp. Eye Res.* **88(2)**, 151-164 (2009).

42. Braga-Vilela, A. S., Pimentel, E. R., Marangoni, S., Toyama, M. H., Vidal, B. D. C., Extracellular matrix of porcine pericardium: Biochemistry and collagen architecture. *J. Membrane Biol.* **221**, 15-25 (2008).

43. Alavi, S. H., Ruiz, V., Krasieva, T., Botvinick, E. L., Arash, K., Characterizing the collagen fiber orientation in pericardial leaflets under mechanical loading conditions. *Ann. Biomed. Eng.* **41(3)**, 547-561 (2013).

44. Maurer, T. et al., Structural characterization of four different natural occurring porcine collagen membranes suitable for medical applications. *Plos One* (2018).

45. Orpheu, S. C. et al., Collagen and elastic content of abdominal skin after surgical weight loss. *Obes. Surg.* **20**, 480-486 (2010).

46. Berillis, P., The role of collagen in the aorta's structure. *The Open Circulation and Vascular Journal* **6**, 1-8 (2013).

47. Holzapfel, G. A., Collagen in arterial walls: Biomechanical aspects. *Collagen: Structure and Mechanics* (2008).

48. Gillies, A. R., Lieber, R. L., Structure and function of the skeletal muscle extracellular matrix. *Muscle Nerve* **44(3)**, 318-331 (2011).

49. Sloan, P., Collagen fibre architecture in the periodontal ligament. *Journal of the Royal Society of Medicine* **79**, 188-191 (1979).

50. Staszyk, C., Wulff, W., Jacob, H., Gasse, H., Collagen fiber architecture of the periodontal ligament in equine cheek teeth. *J. Vet. Dent.* **23(3)**, 143-147 (2006).

51. Liao, J., Yang, L., Grashow, J. Sacks, M. S., The relation between collagen fibril kinematics and mechanical properties in the mitral valve anterior leaflet. *Journal of Biomedical Engineering* **129**, 78-87 (2007).

52. Hammer P.E., Pacak C.A., Howe R.D., del Nido P.J. (2013) Collagen Bundle Orientation Explains Aortic Valve Leaflet Coaptation. In: Ourselin S., Rueckert D., Smith N. (eds) Functional Imaging and Modeling of the Heart. FIMH 2013. Lecture Notes in Computer Science, vol 7945. Springer, Berlin, Heidelberg.

53. Muir, H., Bullough, P., Maroudas, A., The distribution of collagen in human articular cartilage with some of its physiological implications. *The Journal of Bone and Joint Surgery* **52B(3)**, 554-563 (1970).

54. Buhler, R. B. et al., Collagen type I, collagen type III, and versican in vocal fold lamina propria. *Arch. Otolaryngol Head Neck Surg.* **137(6)**, 604-608 (2011).

55. Liakka, A., Apaja-Sarkkinen, M., Karttunen, T., Autio-Harmainen, H., Distribution of laminin and types IV and III collagen in fetal, infant and adult human spleens. *Cell Tissue Res.* **263**, 245-252 (1991).

56. G. M. Miyake, R. A. Weitekamp, V. A. Piunova, R. H. Grubbs, Synthesis of isocyanate-based brush block copolymers and their rapid self-assembly to infrared-reflecting photonic crystals. *J. Am. Chem. Soc.* **134**, 14249-14254 (2012).

57. S. Colodrero, M. Ocana, H. Miguiz, Nanoparticle-based one-dimensional photonic crystals. *Langmuir* **24**, 4430 (2008).

58. M. A. Haque, G. Kamita, T. Kurokawa, K. Tsujii, J. P. Gong, Unidirectional alignment of lamellar bilayer in hydrogel: one-dimensional swelling, anisotropic modulus, and stress/strain tunable structural color. *Adv. Mater.* **22**, 5110-5114 (2010).

59. Vatankhah-Varnosfaderani, M. et al., Chameleon-like elastomers with molecularly encoded strain-adaptive stiffening and coloration. *Science* **359**, 1509-1513 (2018).

60. J. M. Yu, Ph. Dubois, Ph. Teyssie, and R. Jerome, Syndiotactic Poly(methyl methacrylate) (sPMMA)-Polybutadiene (PBD)-sPMMA Triblock Copolymers: Synthesis, Morphology, and Mechanical Properties. *Macromolecules* **29**, 6090-6099 (1996).

61. Honeker, C.C.; Thomas, E.L Impact of Morphological Orientation in Determining Mechanical Properties in Triblock Copolymer Systems. *Chem. Mater*. **8**, 1702-1714 (1996).

62. K. A. Erk, K. J. Henderson, K. R. Shull, Strain Stiffening in Synthetic and Biopolymer Networks. *Biomacromolecules* **11***,* 1358–1363 (2010).

63. A. Watts, N. Kuurokawa, M. A. Hillmyer, Strong, resilient and sustainable aliphatic polyester thermoplastic elastomers. *Biomacromolecules* **18**, 1845-1854 (2017).

64. Bolton, J.; Rzayev, J. Synthesis and melt self-assembly of PS–PMMA–PLA triblock bottlebrush copolymers. *Macromolecules* **2014,** 47 (9), 2864-2874.

65. R. Verduzco, X. Li, S. L. Pesek, G. E. Stein, Structure, function, self-assembly, and applications of bottlebrush copolymers. *Chem. Soc. Rev.* **44**, 2405-2420 (2015).

66. C.M. Bates, A.B. Chang, N, Momčilović, S.C. Jones, R.H. Grubbs, ABA Triblock Brush Polymers: Synthesis, Self-Assembly, Conductivity, and Rheological Properties, *Macromolecules* **48**, 4967-4973 (2015).

67. M. Müllner, A.H.E. Müller, Cylindrical polymer brushes - anisotropic building blocks, unimolecular templates and particle nanocarriers, *Polymer* **98**, 389-401 (2016).

68. Zhang, J., Wang, Z., Wang, X., The synthesis of bottlebrush cellulose-*graft*-diblock copolymer elastomers *via* atom transfer radical polymerization utilizing a halide exchange technique. *Chem. Commun.* **55**, 13904-113907 (2019).

69. Sheiko, S.S., Dobrynin, A.V., Architectural Code for Rubber Elasticity: From Supersoft to Superfirm Materials. *Macromolecules***52**, 7531-7546 (2019).

70. Fantner, G. E. et al., Sacrificial bonds and hidden length: Unraveling molecular mesostructures in tough materials. *Biophysical Journal* **90**, 1411-1418 (2006).

71. Keith, A. N. et al., Bottlebrush bridge between soft gels and firm tissues. *ACS Cent. Sci.* **6**, 413-419 (2020).

72. Wang, J. S., Matyjaszewski, K., Controlled "living" radical polymerization. Atom transfer radical polymerization in the presence of transition-metal complexes. *J. Am. Chem. Soc.* **117**, 5614-5615 (1995).

73. Matyjaszewski, K. Advanced materials by atom transfer radical polymerization. *Adv. Mater.* **30 (23)**, 1706441 (2018).

74. Hou, C. et al., Synthesis of poly(2-hydroxyethyl methacrylate) end-capped with asymmetric functional groups *via* atom transfer radical polymerization. *New J. Chem.* **38**, 2538-2547 (2014).

75. Leonard, J., Thermodynamics of equilibrium polymerization in solution. Effect of polymer concentration on the equilibrium monomer concentration. *Macromolecules* **2(6)**, 661-666 (1969).

76. Rubinstein, M.; Colby, R. H., *Polymer Physics*. Oxford University Press: New York, NY, 2003.

77. Flanders, M. J., Gramlich, W. M. Reversible-addition fragmentation chain transfer (RAFT) mediated depolymerization of brush polymers. *Polym. Chem.* **9**, 2328-2335 (2018).

78. Dainton, F. S., Ivin, K. J. Some thermodynamic and kinetic aspects of addition polymerization. *Q. Rev. Chem. Soc.* **12**, 61-92 (1958).

79. Dainton, F. S., Ivin, K. J. Reversibility of the propagation reaction in polymerization process and its manifestation in the phenomenon of a 'ceiling temperature'. *Nature* **4122**, 705-707 (1948).

80. Small, P. A. The equilibrium between methyl methacrylate and its polymer. *Trans. Faraday Soc.* **49**, 441-447 (1953).

81. Martinez, M.R.; Krys, P.; Sheiko S.S.; Matyjaszewski K. Poor solvents improve yield of grafting-through radical polymerization of OEO19MA. *ACS Macro Letters* **9**, 674-679 (2020).

82. Bywater, S. Evaluation of heats and entropies of polymerization from measurements of equilibrium monomer concentration in solution. *Die Makromolekulare Chemie* **52 (1)**, 120-124 (1962).

83. Ivin, K. J.; Leonard, J. The effect of polymer concentration on the equilibrium monomer concentration for the anionic polymerization of a-methyl styrene in tetrahydrofuran. *European Polymer Journal* **6**, 331-341 (1970).

84. Fiscer, H. The persistent radical effect in "living" radical polymerization. *Macromolecules* **30 (19)**, 5666-5672 (1998).

85. Zhong, M.; Matyjaszewski, K., How fast can a CRP be conducted with preserved chain end functionality?, *Macromolecules (Washington, DC, U. S.)* **44,** 2668-2677 (2011).

86. Braunecker, W. A., Tsarevsky, N. V., Gennaro, A., Matyjaszewski, K., Thermodynamic components of the atom transfer radical polymerization equilibrium: quantifying solvent effects. *Macromolecules* **42**, 6348-6360 (2009).

87. Lee, J. N., Park, C., Whitesides, G. M., Solvent compatibility of poly(dimethylsiloxane)-based microfluidic devices. *Anal. Chem.* **75**, 6544-6554 (2003).

88. Tang, W.; Kwak, Y.; Braunecker, W.; Tsarevsky, N. V.; Coote, M. L.; Matyjaszewski, K., Understanding atom transfer radical polymerization: effect of ligand and initiator structures on the equilibrium constants. *J. Am. Chem. Soc.* **130**, 10702-10713 (2008).

89. Tang, W.; Matyjaszewski, K., Effects of initiator structure on activation rate constants in ATRP. *Macromolecules (Washington, DC, United States)* **40**, 1858-1863 (2007).

90. Lin, C. Y.; Coote, M. L.; Petit, A.; Richard, P.; Poli, R.; Matyjaszewski, K., Ab Initio study of the penultimate effect for the ATRP activation step using propylene, methyl acrylate, and methyl methacrylate monomers. *Macromolecules* **40**, 5985-5994 (2007).

91. Matyjaszewski, K., Atom transfer radical polymerization (ATRP): current status and future perspectives. *Macromolecules* **45**, 4015-4039 (2012).

92. Konkolewicz, D. et al., Aqueous RDRP in the presence of Cu^0: the exceptional activity of Cu^I confirms the SARA ATRP mechanism. *Macromolecules* **47**, 560-570 (2014).

93. Konkolewicz, D. et al., SARA ATRP or SET-LRP. End of controversy? *Polym. Chem.* **5**, 4396-4417 (2014).

94. Ribelli, T. G., Krys, P., Cong, Y., Matyjaszewski, K., Model studies of alkyl halide activation and comproportionation relevant to RDRP in the presence of Cu0. *Macromolecules* **48**, 8428-8436 (2015).

95. Matyjaszewski, K., Paik, H., Zhou, P., Diamanti, S. J., Determination of activation and deactivation rate constants of model compounds in atom transfer radical polymerization. *Macromolecules* **34(15)**, 5125-5131 (2001).

96. Martinez, M. R.; Cong, Y.; Sheiko, S. S.; Matyjaszewski, K. "Thermodynamic Roadmap for the Grafting-through Polymerization" *ACS Macro Lett*. **9**, 1303-1309, (2020).

97. Zhou, Z., Li X., Zare, R. N., Optimizing chemical reactions with deep reinforcement learning. *ACS Cent. Sci.* **3**, 1337-1344 (2017).

98. Sohn K. et al., An extremely simple macroscale electronic skin realized by deep machine learning. *Scientific Reports* **7**, 11061 (2017).

99. Wei, J. N., Duvenaud, D., Aspuru-Guzik, A., Neural networks for the prediction of organic chemistry reactions. *ACS Cent. Sci.* **2**, 725-732 (2016).

100. Afzal, M. A., F., Sonpal, A., Haghighatlari, M., Schultz, A. J., Hachmann, J., Hachmann, J., A deep neural network model for packing density predictions and its application in the study of 1.5 million organic molecules. *Chem. Sci.* **10**, 8374-8383 (2019).

101. Steiner, S. et al., Organic synthesis in a modular robotic system driven by a chemical programming language. *Science* **363**, eaav2211 (2019).

102. Li, H., Tuning the molecular weight distribution from atom transfer radical polymerization using deep reinforcement learning. *Mol. Syst. Des. Eng.* **3**, 496-508 (2018).

103. Wu, S., Machine-learning-assisted discovery of polymers with high thermal conductivity using a molecular design algorithm. *npj Computational Materials* **5**, 66 (2019).

104. Zheng, X., Zheng, P., Zhang, R., Machine learning material properties from the periodic table using convolutional neural networks. *Chem. Sci.* **9**, 8426- 8432 (2018).

105. Xie, T., Grossman, J. C., Crystal graph convolutional neural networks for an accurate and interpretable prediction of material properties. *Physical Review Letters* **120**, 145301 (2018).

106. Ramprasad, R., Batra, R., Pilania, G., Mannodi-Kanakkithodi, A., Kim, C., Machine learning in materials informatics: Recent applications and prospects. *npj Computational Materials* **3**, 54 (2017).

107. Ward, L., Agrawal, A., Choudhary, A., Wolverton, C., A general-purpose machine learning framework for predicting properties of inorganic materials. *npj Computational Materials* **2**, 16028 (2016).

108. Liu, Y., Zhao, T., Ju, W., Shi, S., Materials discovery and design using machine learning. *J Materiomics* **3**, 159-177 (2017).

109. Long, W. J., Griffith, J. L., Selker, H. P., D'Agostino, R. B., A comparison of logistic regression to decision-tree induction in a medical domain. *Computers and Biomedical Research* **26**, 74-97 (1993).

110. Swetapadma, A., Yadav, A., A novel decision tree regression-based fault distance estimation scheme for transmission lines. *IEEE Transactions on power delivery* **32(1)**, 234-245 (2017).

111. Pekel, E., Estimation of soil moisture using decision tree regression. *Theor. Appl. Climatol.* **139**, 1111-1119 (2020).

112. Wang, Y., et al., Random bits forest: a strong classifier/regressor for big data. *Sci. Rep.* **6**, 30086 (2016).

113. Cootes, T. F., Ionita, M. C., Lindner, C., Sauer, P., Robust and accurate shape model fitting using random forest regression voting. In: Fitzgibbon, A., Lazebnik, S., Perona, P., Sato, Y., Schmid, C. (eds). *Computer Vision – ECCV 2012.* **7578** (2012).

114. Dube, T., Mutanga, O., Abdel-Rahman, E. M., Ismail, R., Slotow, R., Predicting *Eucalyptus* spp. stand volume in Zululand, South Africa: an analysis using a stochastic gradient boosting regression ensemble with multi-source data sets. *Intl. J. Remote Sensing* **36(14)**, 3751-3772 (2015).

115. Wang, Y., Feng, D., Li, D., Chen, X., Zhao, Y., Niu, X., A mobile recommendation system based on logistic regression and gradient boosting decision trees. *2016 International Joint Conference on Neural Networks* Vancouver, BC, Canada, 1896-1902 (2016).

116. Chang, Y., Chang, K., Wu, G., Application of eXtreme gradient boosting trees in the construction of credit risk assessment models for financial institutions. *Appl. Soft Computing* **73**, 914-920 (2018).

117. Xu, Y., Du, J., Dai, L., Lee, C., A regression approach to speech enhancement based on deep neural networks. *IEEE/ACM Transactions on Audio, Speech, and Language Processing* **23**, 7-19 (2015).

118. He, T., et al., Deep neural networks and kernel regression achieve comparable accuracies for functional connectivity prediction of behavior and demographics. *NeuroImage* **206**, 116276 (2020).

119. Kinoshita, S., Yoshioka, S., Miyazaki, J., Physics of structural colors. *Rep. Prog. Phys.* **71**, 076401 (2008).

120. Dong, B. Q., et al., Structural coloration and photonic pseudogap in natural random close-packing photonic structures. *Optics Express* **18(14)**, 14430-14438 (2010).

121. Jain, K., Vedarajan, R., Watanabe, M., Ishikiriyama, M., Matsumi, N., Tunable LCST behavior of poly(*N*-isopropylacrylamide/ionic liquid) copolymers. *Polym. Chem.* **6**, 6819-6825 (2015).

122. Zhang, W., Shi, L., Wu, K., An, Y., Thermoresponsive micellization of poly(ethylene glycol)-*b*-poly(*N*-isopropylacrylamide) in water. *Macromolecules* **38(13)**, 5743-5747 (2005).

123. Luo, Y., Yu, W., Xu, F., Zhang, L., Novel thermo-responsive self-assembly micelles from a double brush-shaped PNIPAM-*g*-(PA-*b*-PEG-*b*-PA)-*g*-PNIPAM block copolymer with PNIPAM polymers as side chains. *Polym. Chem.* **50**, 2053-2067 (2012).

124. Nese, A., Li, Y., Sheiko, S. S., Matyjaszewski, K., Synthesis of molecular bottlebrushes by atom transfer radical polymerization with ppm amounts of Cu catalyst. *ACS Macro. Lett.* **1**, 991-994 (2012).

125. J. F. Greenleaf, M. Fatemi, M. Insana, Selected methods for imaging elastic properties of biological tissues. *Annu. Rev. Biomed. Eng.* **5**, 57-78 (2003).

126. Alkhouli, N. et al., The mechanical properties of human adipose tissues and their relationships to the structure and composition of the extracellular matrix. *Am. J. Physiol. Endocrinol. Metab.* **305**, E1427-E1435 (2013).

127. Comley, K., Fleck, N. A., A micromechanical model for the Young's modulus of adipose tissue. *Int. J. Solids and Structures* **47**, 2982-2990 (2010).

128. Wang, Z. G., Liu, Y., Wang, G., Sun, L. Z., Elastography method for reconstruction of nonlinear breast tissue properties. *Int. J. Biomed. Imaging* **4**, 406854 (2009).

129. T. Varghese, J. Ophir, T. A. Krouskop, Nonlinear stress-strain relationships in tissue and their effect on the contrast-to-noise ratio in elastrograms. *Ultrasound in Med. & Biol.* **26 (5)**, 839-851 (2000).

130. A. Samani, J. Bishop, C. Luginbuhl, D. B. Plewes, Measuring the elastic modulus of *ex vivo* small tissue samples. *Phys. Med. Biol.* **48**, 2183-2198 (2003).

131. K. Comley, N. Fleck, The compressive response of porcine adipose tissue from low to high strain rate. *Inter. J. Impact Engineering* **46**, 1-10 (2010).

132. Erkamp, R. Q., Wiggins, P., Skovoroda, A. R., Emelianov, S. Y, O'Donnell, M., Measuring the elastic modulus of small tissue samples. *Ultrasonic Imaging* **29**, 17-28 (1998).

133. Samani, A., Plewes, D., A method to measure the hyperelastic parameters of *ex vivo* breast tissue samples. *Phys. Med. Biol.* **49**, 4395-4405 (2004).

134. Yang, T. et al., The rule of strain in different stratification of the intervertebral disc under physiologic loading. *Biomed. Research* **28(2)**, 987-994 (2017).

135. W. F. Deccraemer, M. A. Maes, V. J. Vanhuyse, An elastic stress-strain relation for soft biological tissues based on a structural model. *J. Biomechanics* **13**, 463-468 (1980).

136. E. Pena, B. Calvo, M. A. Martinez, M. Doblare, On finite-strain damage of viscoelastic-fired materials. Application to soft biological tissues. *Int. J. Numer. Meth. Engng.* **74**, 1198-1218 (2008).

137. Maceri, F., Marino, M., Vairo, G., A unified multiscale mechanical model for soft collagenous tissues with regular fiber arrangement. *Journal of Biomechanics* **43**, 355-363 (2010).

138. Pioletti, D. P., Rakotomanana, L. R., Benvenuti, J.-F., Leyvraz, P.-F., Viscoelastic constitutive law in large deformations: applications to human knee ligaments and tendons. *Journal of Biomechanics* **31**, 753-757 (1998).

139. Dorow, C., Krstin, N., Sander, F.-G., Determination of the mechanical properties of the periodontal ligament in a uniaxial testing experiment. *J. Orafac Orthop.* **2**, 100-107 (2003).

140. Komatsu, K., Shibata, T., Shimada, A., Viidik, A., Chiba, M., Age-related and regional differences in the stress-strain and stress-relaxation behaviors of the rat incisor periodontal ligament. *Journal of Biomechanics* **37**, 1097-1106 (2004).

141. M. Itskov, A. E. Ehret, D. Mavrilas, A polyconvex anisotropic strain-energy function for soft collagenous tissues. *Biomech. Model Mechanbiol* **5**, 17-26 (2006).

142. Spoerl, E., Huhle, M., Seiler, T., Induction of cross-links in corneal tissue. *Exp. Eye Res.* **66**, 97-103 (1998).

143. Lim, J., Hong, J., Chen, W. W., Weerasooriya, T., Mechanical response of pig skin under dynamic tensile loading. *International Journal of Impact Engineering* **38**, 130-135 (2011).

144. Hoeltzel, D. A., Altman, P., Buzard, K., Choe, K., Strip extensiometry for comparison of the mechanical response of bovine, rabbit, and human corneas. *J. Biomech. Eng.* **114 (2)**, 202-215 (1992).

145. Kra, S.; Andreassen, T. T. Mechanical properties of human lens capsule. *Prog. Retin. Eye Res.* **22**, 749-767 (2003).

146. Silver, F. H.; Freeman, J. W.; Devore, D. Viscoelastic properties of human skin and processed dermis. *Skin Res. Tech.* **7**, 18-23 (2001).

147. Hebrank, M. R. Mechanical properties and locomotor functions of eel skin. *Biol. Bull.* **158**, 58-68 (1980).

148. Bancelin, S. et al., Ex vivo multiscale quantitation of skin biomechanics in wild-type and genetically-modified mice using multiphonon microscopy. *Sci. Rep.* **5**, 17635 (2015).

149. Lim, J.; Hong, J.; Chen, W.W.; Weerasooriya, T. Mechanical response of pig skin under dynamic tensile loading. *Int. J. Impact. Eng.* **38**, 130-135 (2011).

150. Wright, D. M.; Duance, V. C.; Wess, T. J.; Kielty, C. M.; Purslow, P. P. The supramolecular organisation of fibrillin-rich microfibrils determines the mechanical properties of bovine zonular filaments. *J. Exp. Bio.* **202**, 3011-3020 (1999).

151. Shreiber, D. I.; Hao, H.; Elias, R. A. Probing the influence of myelin and glia on the tensile properties of the spinal cord. *Biomech. Model. Mechanobiol.* **8**, 311-321 (2009).

152. D. Balzani, P. Neff, J. Schroder, G. A. Holzapfel, A polyconvex framework for soft biological tissues. Adjustment to experimental data. *Inter. J. Solids and Structures* **43**, 6052-6070 (2006).

153. D. Craiem, F. J. Rojo, J. M. Atienza, R. L. Armentano, G. V. Guinea, Fractional-order viscoelasticity applied to describe uniaxial stress relaxation of human arteries. *Phys. Med. Biol.* **53**, 4543-4554 (2008).

154. M. L. Raghavan, M. W. Webster, D. A. Vorp, *Ex vivo* biomechanics behavior of abdominal aortic aneurysm: assessment using a new mathematical model. *Annals of Biomedical Engineering* **24**, 573-582 (1996).

155. M. J. Thubrikar, M. Labrosse, F. Robiscek, J. Al-Soudi, B. Fowler, Mechanical properties of abdominal aortic aneurysm wall. *J. Medical Engineering & Technology* **25 (4)**, 133-142 (2001).

156. D. A. Vorp, B. J. Schiro, M. P. Ehrlich, T. S. Juvonen, M. A. Ergin, B. P. Griffith, Effect of aneurysm on the tensile strength and biomedical behavior of the ascending thoracic aorta. *Ann. Thorac. Surg.* **75**, 1210-1214 (2003).

157. Destrade, M., Annaidh, A. N., Coman, C. D., Bending instabilities of soft biological tissues. *International Journal of Solids and Structures* **46**, 4322-4330 (2009).

158. Xiong, J., Wang, S. M., Zhou, W., Wu, J. G., Measurement and analysis of ultimate mechanical properties, stress-strain curve fit, and elastic modulus formula of human abdominal aortic aneurysm and nonaneurysmal abdominal aorta. *Journal of Vascular Surgery* **48 (1)**, 189-195 (2008).

159. Tajaddini, A., Kilpatrick, D. L., Vince, D. G., A novel experimental method to estimate stress-strain behavior of intact coronary arteries using intravascular ultrasound (IVUS). *J. Biomech. Eng.* **125 (1)**, 120-123 (2003).

160. Place, E. S.; George, J. H.; Williams, C. K.; Stevens, M. Synthetic polymer scaffolds for tissue engineering. *Chem. Soc. Rev.* **38**, 1139-1151 (2009).

161. Holzapfel, G. A.; Sommer, G.; Regitnig, P. Anisotropic mechanical properties of tissue components in human atherosclerotic plaques. *J. Biomech. Eng.* **126**, 657-665 (2004).

162. Holzapfel, G. A.; Sommer, G.; Gasser, C. T.; Regitnig, P. Determination of layer-specific mechanical properties of human coronary arteries with nonatherosclerotic intimal thickening and related constitutive modeling. *Am. J. Physiol. Heart Circ. Physiol.* **289**, H2048-H2058 (2005).

163. Jabareen, M.; Mallik, A. S.; Bilic, G.; Zisch, A. H.; Mazza, E. Relation between mechanical properties and microstructure of human fetal membranes: an attempt towards a quantitative analysis. *Eur. J. Obstet. Gynecol. Reprod. Biol.* **144**, 5134-5141 (2009).

164. Chen, Z.-L.; Chen, Y.-Z.; Hu, Z.-Y. A micromechanical model for estimating alveolar wall strain in mechanically ventilated edematous lungs. *J. Appl. Physiol.* **117**, 586-592 (2014).

165. E. P. M. Rousseau, A. A. H. J. Sauren, M. C. V. Hout, A. A. V. Steenhoven, Elastic and viscoelastic material behavior of fresh and glutaraldehyde-treated porcine aortic valve tissue. *J. Biomechanics* **16 (5)**, 339-348 (1983).

166. N. D. Broom, The stress/strain and fatigue behavior of glutaraldehyde preserved heart-valve tissue. *J. Biomechanics* **10**, 707-724 (1977).

167. J. H. McElhaney, Dynamic response of bone and muscle tissue. *J. Appl. Physiology* **21 (4)**, 1231-1236 (1966).

168. Alipour-Haghighi, F., Titze, I. R., Elastic models of vocal fold tissues. *The Journal of the Acoustical Society of America* **90**, 1326-1331 (1991).

169. Song, B., Chen, W., Ge, Y., Weerasooriya, T., Dynamic and quasi-static compressive response of porcine. *Journal of Biomechanics* **40**, 2999-3005 (2007).

170. Kunzelman, K. S., Cochran, R. P., Stress/strain characteristics of porcine mitral valve tissue: Parallel versus perpendicular collagen orientation. *Journal of Cardiac Surgery* **7 (1)**, 71-78 (1992).

171. Morrow, D. A., Donahue, T. L. H., Odegard, G. M., Kaufman, K. R., Tranversely isotropic tensile material properties of skeletal muscle tissue. *Journal of the Mechanical Behavior of Biomedical Materials* **3**, 124-129 (2010).

172. Chen, Q.-Z. Harding, S. E.; Ali, N. N.; Lyon, A. R.; Boccaccini, A. R. Biomaterials in cardiac tissue engineering: ten years of research survey. *Mater. Sci. Eng. R Rep.* **59**, 1-37 (2008).

173. Hunter, E. J.; Titze, I. R. Refinements in modeling the passive properties of laryngeal soft tissue. *J. Appl. Physiol.* **103**, 206-219 (2017).

174. Malisoux, L.; Francaux, M.; Nielens, H.; Theisen, D. Stretch-shortening cycle exercise: an effective training paradigm to enhance power output of human single muscle fibers. *J. Appl. Physiol.* **100**, 771-779 (2006).

175. Roberts, T. J. Contribution of elastic tissues to the mechanics and energetics of muscle function during movement. *J. Exp. Biol.* **219**, 266-275 (2016).

176. K. Miller, K. Chinzei, Mechanical properties of brain tissue in tension. *J. Biomechanics* **35**, 483-490 (2002).

177. K. Miller, K. Chinzei, G. Orssengo, P. Bednarz, Mechanical properties of brain tissue in-vivo: experiment and computer simulation. *J. Biomechanics* **33**, 1369-1376 (2000).

178. B. Rashid, M. Destrade, M. D. Gilchrist, Mechanical characterization of brain tissue in tension at dynamic strain rates. *J. Mechanical Behaviors of Biomedical Materials* **33**, 43-54 (2014).

179. B. Rashid, M. Destrade, M. D. Gichrist, Mechanical characterization of brain tissue in compression at dynamic strain rates. *J. Mechanical Behavior of Biomedical Materials* **10**, 23-38 (2012).

180. Franceschini, G., Bigoni, D., Regitnig, P., Holzapfel, G. A., Brain tissue deforms similarly to filled elastomers and follows consolidation theory. *J. Mech. Phys. Solids* **54**, 2592-2620 (2006).

181. Pervin, F.; Chen, W. W. Effect of inter-species, gender, and breeding on the mechanical behavior of brain tissue. *NeuroImage* **54**, S98-102 (2011).

182. Chui, C., Kobayashi, E., Chen, X., Hisada, T., Sakuma, I., Combined compression and elongation experiments and non-linear modeling of liver tissue for surgical simulation. *Medical & Biological Engineering & Computing* **42**, 787-798 (2004).

183. Carter, F. J., Frank, T. G., Davies, P. J., McLean, D., Cuschieri, A., Measurements and modeling of the compliance of human and porcine organs. *Medical Image Analysis* **5**, 231-236 (2001).

184. Maksym G. N.; Bates, J. H. A distributed nonlinear model of lung tissue elasticity. *J. Appl. Physiol.* **82**, 32-41 (1997).